Cell Sorting in Pillar Arrays based on Electrokinetics and Morphology

Ho, Bao Dang

2018

Document Version:
Publisher's PDF, also known as Version of record

Cell Sorting in Pillar Arrays based on Electrokinetics and Morphology

BAO DANG HO
FACULTY OF ENGINEERING | LUND UNIVERSITY

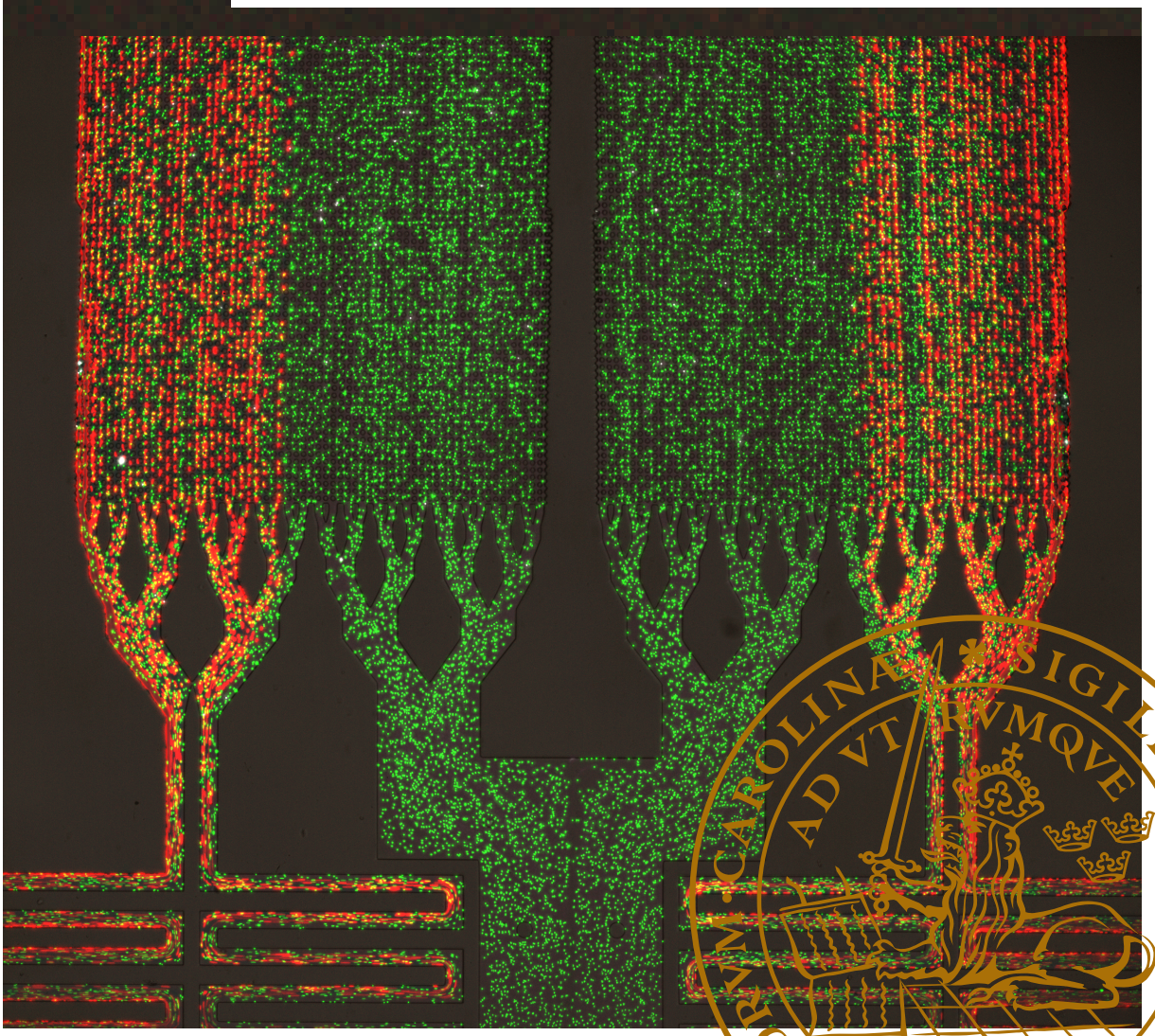

Cell Sorting in Pillar Arrays based on Electrokinetics and Morphology

Bao Dang Ho

LUND
UNIVERSITY

DOCTORAL DISSERTATION

by due permission of the Faculty of Engineering, Lund University, Sweden.
To be defended at Rydbergssalen, Sölvegatan 14,
on Friday 23rd of November 2018 at 9:15.

Faculty opponent:
Prof. Michael Hughes
University of Surrey, Guildford, Surrey, UK

Organization	Document name
LUND UNIVERSITY Department of Physics Professorsgatan 1 223 63 Lund Sweden	**DOCTORAL DISSERTATION** Date of disputation 2018-11-23 Sponsoring organization
Author(s) Bao Dang Ho	

Title and subtitle

Cell Sorting in Pillar Arrays based on Electrokinetics and Morphology

Abstract

Deterministic Lateral Displacement (DLD) is a method capable of sorting cells based on size where mechanical interactions between a sufficiently large particle and obstacles in a microfludic *pillar array* force the particle to follow a different trajectory than their smaller counterparts, resulting in continuous lateral separation. To extend the capability of DLD, electrical interaction between particles and pillars can be employed to complement the mechanical interaction, making electrical/dielectric properties additional parameters for sorting. Another idea is to exploit the morphologies of cells and as a concequence, their dynamical properties, to sort them in DLD. The development of DLD cell sorting methods based on those two ideas has brought forth five papers appended to this thesis: paper I, III, and V (combination of electrokinetics and DLD), and paper II and IV (exploiting morphology in sorting by DLD).

In the first topic, differences in electric properties or dielectric properties of particles and cells are employed to extend the capability of DLD. In Paper I, an AC electric field was applied across DLD devices having insulating pillars to sort similar-sized polystyrene particles having different surface charge, viable from non-viable yeast cells, and viable from non-viable *E. coli* bacteria. In Paper III, the same method was utilised on open channel DLD devices, showing unaltered effectiveness but offering the ability to flexibly change the distance between the electrodes. Also in the topic of combining electrokinetics and DLD, Paper V introduced a new type of DLD device where the electrodes were defined locally on every pillar, making it easier to generate a high electric field strength.

Besides electrical properties, morphology is another useful accompaniment to DLD. In Paper II, pathogenic *Streptococcus pneumoniae* bacteria were fractionated in DLD devices according to the difference in their morphology, viz. their chain length. It was also demonstrated, in paper IV, that an AC field can be used to rotate non-spherical red blood cells and in turn, change their trajectory in a DLD device. This implies an opportunity to sort red blood cells from cells having different morphology, either spherical cells or parasites like trypanosomes.

Key words

Label-free separation, Deterministic Lateral Displacement, Electrokinetics

Classification system and/or index terms (if any)

Supplementary bibliographical information	Language
	English
ISSN and key title	ISBN
	978-91-7753-888-2 (print) 978-91-7753-889-9 (pdf)
Recipient's notes	Number of pages: 199 / Price
	Security classification

Cell Sorting in Pillar Arrays based on Electrokinetics and Morphology

Bao Dang Ho

LUND
UNIVERSITY

Cover illustration front: Purification of 1.1 μm polystyrene microspheres from a mixture of 1.1 μm and 2.1 μm polystyrene microspheres. The device has 32 units like this in parallel and is intended for purifying *S. pneumoniae* single cocci from chains at high throughput.

Cover illustration back: DLD obsession. After four years working on DLD, you will see it everywhere.

Funding information: The thesis work was financially supported by grants from the European Union, under the Seventh Framework Programme FP7/2007-2013/ within the project LAPASO (project number 607 350) and under Horizon2020/HEALTH within the project BeyondSeq (project number 634 890).

Faculty of Engineering, Department of Physics

ISBN: 978-91-7753-888-2 (print)
ISBN: 978-91-7753-889-9 (pdf)

Printed in Sweden by Media-Tryck, Lund University, Lund 2018

Media-Tryck is an environmentally certified and ISO 14001 certified provider of printed material. Read more about our environmental work at www.mediatryck.lu.se

To my parents and my sister

Contents

Abstract

Deterministic Lateral Displacement (DLD) is a method capable of sorting cells based on size where mechanical interactions between a sufficiently large particle and obstacles in a microfludic *pillar array* force the particle to follow a different trajectory than their smaller counterparts, resulting in continuous lateral separation. To extend the capability of DLD, electrical interaction between particles and pillars can be employed to complement the mechanical interaction, making electrical/dielectric properties additional parameters for sorting. Another idea is to exploit the morphologies of cells and as a concequence, their dynamical properties, to sort them in DLD. The development of DLD cell sorting methods based on those two ideas has brought forth five papers appended to this thesis: paper I, III, and V (combination of electrokinetics and DLD), and paper II and IV (exploiting morphology in sorting by DLD).

In the first topic, differences in electric properties or dielectric properties of particles and cells are employed to extend the capability of DLD. In Paper I, an AC electric field was applied across DLD devices having insulating pillars to sort similar-sized polystyrene particles having different surface charge, viable from non-viable yeast cells, and viable from non-viable *E. coli* bacteria. In Paper III, the same method was utilised on open channel DLD devices, showing unaltered effectiveness but offering the ability to flexibly change the distance between the electrodes. Also in the topic of combining electrokinetics and DLD, Paper V introduced a new type of DLD device where the electrodes were defined locally on every pillar, making it easier to generate a high electric field strength.

Besides electrical properties, morphology is another useful accompaniment to DLD. In Paper II, pathogenic *Streptococcus pneumoniae* bacteria were fractionated in DLD devices according to the difference in their morphology, viz. their chain length. It was also demonstrated, in paper IV, that an AC field can be used to rotate non-spherical red blood cells and in turn, change their trajectory in a DLD device. This implies an opportunity to sort red blood cells from cells having different morphology, either spherical cells or parasites like trypanosomes.

Popular Summary in English

Most of the visible objects and tools around us are made from solid materials, which have definite shape and high strength to withstand external forces from the surrounding environment. Fluids, on the other hand, are highly deformable and change shape easily under an applied force, making it difficult to control or manipulate them. Nevertheless, there are areas of science and technology where fluids can be constrained, controlled, and made use of to bring out useful applications for human life. Microfludics is one such field.

Microfluidics refers to the study of liquids and gases at the micrometric scale – the scale of things that are smaller than the resolution limit of a human's eyes, the world of tiny bio-particles like bacteria, parasites or red blood cells. There are several good reasons for studying and engineering tools at such a minute scale. Firstly and straightforwardly, in order to deal with cells and pathogens, we need to shrink our tools and devices down to their size. Secondly, making tiny devices also means more economical use of rare samples from patients or expensive reagents required for analysis, making diagnosis more affordable and less painful. Last but not least, we might integrate many tiny tools and devices into a small handheld chip which can perform a complete diagnostic task, a lab-on-a-chip, and distribute them to the patients' home where they perform their own diagnostic procedures. This is similar to the development where centralised building-sized computers became individual handheld smartphones, with equal importance to the well-being in our society.

In the theme of microfludics for bio-medical applications, this work focuses on separating different kinds of cells by their physical properties, with the goal of making biomedical tools that are simpler, cheaper and more accessible to everyday life. The three properties of interest in this work are size, electrical/dielectric properties, and morphology of the cells that need sorting. Thanks to the disposability of the material, the simplicity of the mechanism (no complicated chemical treatments needed), the prospects are bright for making the devices available to each person's home for them to perform the diagnosis by themselves or to distant regions of the world to help local people conduct useful medical tests which are currently inaccessible to them. The study presented here is a modest step in the journey to that future.

Acknowledgements

It has been more than four years since my first visit to Lund for the interview of my current PhD position and my first participation in LAPASO, the Label-free Particle Sorting consortium funded by the European Commission, even before I was officially admitted to the project. During the challenging but interesting journey thus far, I am immensely thankful to my supervisor, Prof. Jonas Tegenfeldt, who enrolled me into his team and introduced to me the field of cell separation. While giving me much freedom to try any ideas I could think of, he provided me with every necessary guidance and support, networked me with experts in the fields he was not quite an expert on, and gave me almost instant feedback on my work, manuscripts, and thesis.

I would also like to thank my co-supervisor, Dr. Jason Beech, who has taught me tremendous practical knowledge and skills in, for example, microfludics and soft lithography, cleanroom expertise, and microscopy. When things did not seem right in the lab, Jason would be the first person I turned to and he never refused to give a hand.

The work in this thesis would never be complete without collaboration and support from LAPASO principle investigators and fellows: Prof. Hywel Morgan, Dr. Daniel Spencer, and Carlos Honrado from the University of Southampton; Prof. Birgitta Henriques Normark, Dr. Genevieve Garriss, and Vitor Oliveira from Karolinska Institute; Anke, Miguel, Clement, Elisabeth, Walter, Laura, and other LAPASO partners and fellows who have shared great times with me during every LAPASO meeting.

I have also received tremendous help from my group mates, who are also my good friends and lunch companions: Trung, Stefan, Kushagr and Oskar. Trung has been my close friend and collaborator from the first day in Lund and provides me with a lot of help during my PhD. Stefan is my DLD advisor, who is also my most frequent BMC lunch buddy. Oskar is my source of inspiration and optimism. Kushagr is the guy who gives you the impression that he knows everything, which may be true. In general, it is a group of buddies I can get advice about anything, from science to every matter in life.

Within the division of Solid State Physics, I would like to thank Gerda for her great help during my three years with LAPASO, Christelle for her kindness and the cosy dinners at her and Jonas' home, Elke and Martin for the energy and fun they bring, Damiano and

my office buddies throughout the years: Enrique, Michael, Pyry, Steve, Reza, Ivan, for the warm atmosphere they create at C366. All of them have made FTF my pleasant workplace.

I am grateful to be part of the biogroup: Christelle, Heiner, Jonas, Laura, Elke, Fei Fei, Rebehkah, Mercy, Martin, Frida, Inga, Zhen, Regina, Kalle, Therese, Roman, Jingyuan, Pradheebha, who have given constructive comments about my work and have taught me a lot in biomedical field during our weekly meetings. I also feel thankful to the faculty, administrative, and technical staff at FTF, who have directly helped me during my PhD or have contributed to building a supportive working environment I enjoy every day: Dan, Jonas Johansson, Anneli, Anders Gustafsson, Maria, Johanna, Janne, Bengt, Håkan, Marica, Mia, Sara, Mariusz, Abdul-Rehman, and Charlotte. And the list goes on. Thank you all for the good four years I have had at FTF.

Outside work, I would like to thank Hoa for his daily encouragement on my PhD research, Hong for being my good corridor friend, Ngoc, Dana, Tu, Hien, Van, Jasmine for all the great dinners and the delicious meals I enjoy (I now realise that most of my Vietnamese friends are excellent cooks), and Quan, Vinh, Minh, Thao for all the talks and advice for my PhD. Thank you all for building such a great Vietnamese community here in Lund.

Big thanks also go to all my corridor friends at Sparta 39B, who have contributed to a friendly and lively atmosphere I enjoy since 2016. Christina Naum, Julia von Treskow, Jiyan, and Isabel frequently asked me about my PhD work and encouraged me when my experiments did not go as planned. Jiyan even cooked dinners for me during my busy writing time. I sure will miss you all when I move out at the end of this year. Also, I want to thank Magnus, for giving me a comfortable accommodation when I first started my PhD in Lund, four years ago.

Lastly and most importantly, I want to express my gratitude to my parents and my younger sister, who have given me unconditional love, support and encouragement, from very far away in Vietnam.

List of Publications

This thesis is based on the following papers and manuscripts:

I **Cell Sorting using Electrokinetic Deterministic Lateral Dispalcement**
B. D. Ho, J. P. Beech, C. Honrado, D. Spencer, H. Morgan, and J. O. Tegenfeldt
Manuscript

I designed and made the masters and the devices. I performed all the experiments, analysed the data, and did the simulations. I wrote the manuscript.

II **Separation of Pathogenic Bacteria by Chain Length**
J. P. Beech, B. D. Ho, G. Garriss, V. Oliveira, B. Henriques-Normark, and J. O. Tegenfeldt
Analytica chimica acta, 2018, **1000**, 223-231

I designed the devices. I made the masters and devices, together with J. Beech. I characterised the devices with polystyrene beads (Figure 2E,F). I manually measured the size of the bacteria (the data for Figure 4). I processed the videos for Figure 7. I took part in most of the experiments and discussions.

III **Open channel Deterministic Lateral Displacement for Particle and Cell Sorting**
T. S. H. Tran, B. D. Ho, J. P. Beech, and J. O. Tegenfeldt
Lab Chip, 2017, **17**, 3592

I took part in the electrokinetic experiments (Fig 6), the initial experiments (Figure 3C), and the flow resistance experiments (Section "Flow resistance" in the ESI).

IV **Electrokinetic Rotation of Red Blood Cells in Deterministic Lateral Displacement devices**
B. D. Ho, H. Yavari, S. H. Holm, T. S. H. Tran, J. P. Beech, and J. O. Tegenfeldt
Manuscript

I conceived the idea. I made the devices, performed the experiment, analysed the data together with H. Yavari. I wrote most of the manuscript (section 2, half of section 3, section 4, and section 5).

V **Active Posts in Deterministic Lateral Displacement Devices**
J. P. Beech, K. Keim, B. D. Ho, C. Guiducci, and J. O. Tegenfeldt
Manuscript

I contributed to the design of the microfluidic part of the device. I took part in the experiments with particle sizes over $2\mu m$ (Figure 4, Figure 8 of the main text and Figure 5 of the ESI). I helped with setting up the numerical simulations.

The following manuscript is related but beyond the scope of this thesis:

VI **Integrated Separation and Readout - Towards Field-diagnosis of Trypanosomiasis**
C. Honrado, S. H. Holm, J. P. Beech, B. D. Ho, D. Spencer, M. P. Barrett, J. O. Tegenfeldt, and H. Morgan
Manuscript
I contributed in the experimental work and the design of the integrated device.

All papers are reproduced with permission of their respective publishers.

List of Abbreviations

AC	Alternating Current
BOP	Bipolar Operational Power
CAD	Computer-Aided Design
CFU	Colony-Forming Unit
CTC	Circulating Tumour Cell
DC	Direct Current
DEP	Dielectrophoresis
DLD	Deterministic Lateral Displacement
DNA	Deoxyribonucleic Acid
EOF	Electroosmotic Flow
EP	Electrophoresis
ESI	Electronic Supplementary Information
FACS	Fluorescence-Activated Cell Sorting
FEM	Finite Element Method
FFF	Field Flow Fractionation
FSI	Fluid-Structure Interaction
GUI	Graphical User Interface
IBM	Immersed Boundary Method
LAPASO	Label-free Particle Sorting
LBM	Lattice Boltzmann Method
LED	Light-Emitting Diode

MACS	Magnetic-Activated Cell Sorting
MCF-7	Michigan Cancer Foundation-7
MEMS	MicroElectroMechanical System (a.k.a. Microsystem Technology)
MFCS	Microfluidic Control System
PDMS	PolyDiMethylSiloxane
PEG	PolyEthylene Glycol
PFOTS	Trichloro (1H,1H,2H,2H-PerFluoroOcTyl) Silane
PLL	Poly(L-Lysine)
POC	Point-Of-Care
RMS	Root Mean Square
RNA	RiboNucleic Acid
sCMOS	scientific Complementary Metal Oxide Semiconductor
SDPD	Smoothed Dissipative Particle Dynamics
RBC	Red Blood Cell
WBC	White Blood Cell

List of Symbols

Roman alphabet

D	Material derivative
D_C	Critical diameter of DLD
$\mathbf{D_{dir}}$	Direction toward the nearest wall (unit vector)
d_p	Diameter of particle
D_w	Distance to wall
$\mathbf{E}$	Electric field
e	Euler's number ($e \simeq 2.71828$)
$\mathbf{E_{rms}}$	Electric field (root mean square)
E_t	Tangential component of electric field
$\mathbf{F}$	Force
f	Frequency of electric field
$\mathbf{f}$	Total body force per unit mass
$\mathbf{F_t}$	Total force acting on particle
$\mathbf{F_d}$	Stokes drag force acting on particle
$\mathbf{F_{DEP}}$	Dielectrophoretic force acting on particle
$\mathbf{F_w}$	Steric wall force acting on particle
f_{CM}	The Clausius-Mossotti factor
G	Gap between two pillars of DLD
$\mathbf{I}$	Identity matrix
i	The imaginary unit ($i = \sqrt{-1}$)

Roman alphabet (continued)

$\mathbf{J}$	Current density
j	(Subscript) Type of ions
K	Surface conductance
k_B	Boltzmann constant
L	Characteristic dimension of microfludic channel
m	Mass
m	(Subscript) Medium
N	Period of a DLD array
n	Number density of ions
n_0	Number density of ions in the bulk solution
$\mathbf{P}$	Dipole moment
p	(Subscript) Particle
p	Pressure
q	Elementary charge ($q \simeq 1.602 \times 10^{-19}$)
r	Particle radius
Re	Reynolds number
$Re\,()$	The real part of ...
r_p	Particle radius
s	(Subscript) Surface
$step\,()$	Step function

Roman alphabet (continued)

T	Absolute temperature
T	(Superscript) Transpose of a matrix
t	Time
$\mathbf{u}$	Velocity of fluid
U_E	Electric potential energy
u_{eof}	Electroosmotic flow velocity
u_{ep}	Electrophoretic velocity of particle
V	Electric potential
$\mathbf{v}$	Velocity of particle
w	(Subscript) Wall
z	Charge number

Greek alphabet

∇	Del operator
ε	Permittivity
ζ	Zeta potential
η	Dynamic viscosity
κ	Inverse of Debye length
λ_D	Debye length
μ_{eof}	Electroosmotic flow mobility
μ_{ep}	Electrophoretic mobility of particle
ρ	Mass density of fluid
ρ_q	Volume charge density
ρ_p	Mass density of particle
σ	Conductivity
τ_p	Particle velocity response time in Stokes flow
ϕ	Electric potential
ω	Angular velocity

Chapter 1

Introduction

There is plenty of room at the bottom.
— Richard Feynman

1.1 Microfluidics

HUMANS have the tendency of miniaturizing their tools, making things smaller yet better and even cheaper. One excellent example is the computer. The replacement of bulky mechanical shafts and disks, or electromagnetic relays and vacuum tubes with semiconductor components has helped miniaturizing a computer from a room-sized machine to a cell phone in people's pockets nowadays, with far better performance at much lower price. Microfluidics has developed in a way that is analogous to that of microelectronics: microelectronics studies and makes use of solid state electronic circuits at micro and nano scale, while microfluidics investigates and manipulates fluids in channels whose sizes are smaller than the width of a human hair. In fact, just like microelectronics, microfludics has emerged as a field, encompassing a large number of research publications, enormous technological development and bringing about many patents and start-up companies.

Microfludics started in the late 70s with IBM ink jet printer nozzles[1] and Stanford University's miniaturized gas chromatography[2]. The early works in microfludics till the early 90s were closely related to Microsystem Technology (MEMS). In fact, most of the

early microfludic products were made in silicon or glass, the familiar materials of the MEMS industry. A large portion of the research was focused on theory, modeling/simulation, or the technological aspects (*e.g.* making of valves and pumps in silicon). Applications were narrow and limited to flow sensors, ink jet printer nozzle arrays, micro-dosing systems and microchemical analysis systems[3]. The next stage of microfludics was marked with the introduction of soft lithography using polydimethylsiloxane (PDMS)[4] to fabricate devices, transferring microfludics from a branch of MEMS into a distinct field of its own. The main advantage of soft lithography is the ease to replicate new devices from an original mold. Also, the transparency of PDMS to visible and ultraviolet light and its compatibility to cells have made microfludics more friendly to biological and medical applications. The "softness" of PDMS has also enabled the fabrication of flexible miniature pneumatic valves, mixers, and pumps, broadening the capability of microfludic devices. Besides silicon, glass, and PDMS, other materials like thermoplastics (polystyrene, cyclic olefin copolymer, polymethyl methacrylate, and polycarbonate) or familiar materials (paper, wax, and cloth), have also been exploited for specific requirements.

Thanks to the maturity of the technology and the diversity of the materials used for fabrication, microfluidics has found various applications in biological and medical research[5,6]. Following are just some of the key applications:

- ▷ *Point-of-care diagnostics (POC)* is a promising area for microfludic applications since it fits with the key aspect of microfludics: making low-cost and even disposable lab-on-a-chip devices that can complete a specific task. There have been several microfludic POC products on the market[7] with limited success. The development of paper-based microfludics[8], together with the innovations in optical microfluidic technologies[9], for example cell phone microscopy[10], will conceivably make microfluidic POC devices readily available in everyday life.
- ▷ *Droplet microfludic devices*[11,12] can generate, at high speed, a large amount of microscopic single-droplet containers that can be considered as tiny test tubes for a wide range of applications such as: chemical reactions, therapeutic agent delivery, cell culture, or molecular synthesis.
- ▷ *Cell and bioparticle sorting devices* fractionate a heterogeneous population of cells and bioparticles into homogeneous ones, for preparative and analytical purposes. This will be discussed in more details in the next section.

- ▷ *Sensor applications* cover a wide range of physical and chemical sensors, electrochemical sensors, and biosensors. Examples include thread-based strain or pH sensors[13], paper-based electrochemical sensor[14], or yeast cell growth sensor using polymer microcantilever[15].

- ▷ *Cell biology*[16] is a fast-growing area of microfludics. Applications are diverse and include: cell culture[17], neuroscience, stem cell or cancer cell research, drug discovery and screening, microbiology, and clinical diagnostics, just to name a few. A typical example is the immobilisation of *C. elegans* using microfluduics, which offers the unprecedented ability to conveniently trap, manipulate, and image the worms[18–21].

- ▷ *Organ-on-a-chip*[22] mimics and constructs the complex structures of tissues or organs on microfludic chips, for example: liver on chip[23], kidney on chip[24], or lung on chip[25].

The above-mentioned diverse applications of microfluidics substantiate its importance and visibility in today's society. However, a phenomenal "killer application", like the personal computers or the smart phones as with microelectronics, has not yet arrived[5,6]. A large proportion of research in microfluidics is still in the engineering fields[6]. Sackmann *et al.*[6] made some well founded suggestions for making microfluidics a mainstream in biomedical research: offering fundamentally new capabilities instead of only improving upon existing methods, keeping the devices as simple as possible, fostering collaborations between physicists/engineers and biologists/medical experts, and finding the right problems. The following section will attempt to convince the readers that biological particle sorting is one of the right problems.

1.2 Particle Sorting

Sorting is the process of regaining the order of a system, a quantity which universally decreases over time. This can mean either arranging individual objects in a predefined sequence or grouping similar objects together into specific groups. In biological and medical fields, the latter definition is normally assumed. The objects of biomedical sorting are normally micro- or nanoscale bioparticles and cells, for example tissue-derived cells, blood cells, bacteria, parasites, and micro/nano vesicles. In terms of purpose, biomedical particle sorting can be a preparative step where the sorted populations are reserved for further study or analysis, or an analytical process where the distributions of the sorted populations provide useful information for clinical diagnosis. To set the background for the rest of the thesis, this section will briefly introduce some of the most popular sorting techniques employed in biomedical applications nowadays.

The simplest yet most prevalent cell sorting techniques are *filtering* and *centrifugation*. The first method makes use of filters which have pore sizes in the micrometer range to only allow cells of a predefined upper size limit to pass through. Examples of such filters are disposable filter papers used in preparation of samples for cell culture or flow cytometry analysis or nylon filters used in sorting adipocytes by size[26,27]. The second method, centrifugation, takes advantage of the difference in sedimentation speed of particles, which is a function of size and mass density, to sort them accordingly. Centrifuge machines are indispensable in most clinical or research labs for separation of blood components or for concentrating and collecting of particles in a liquid medium. Despite being simple, fast, and easy to use, filtering and centrifugation only target size or density of the cells and as a result, sorting by other physical properties or functional properties is impossible. Centrifuge machines are also rather bulky and require electric power to operate.

To target functional properties of cells, other methods, *magnetic-activated cell sorting (MACS)* and *fluorescence-activated cell sorting (FACS)*, make use of labeled probes to identify the cells of interest. In these methods, antibodies are coated on magnetic nanoparticles (MACS) or attached to fluorophores (FACS). The antibodies then bind to specific antigens on the surface of the cells of interest, thereby tagging them with magnetic nanoparticles or fluorophores. In MACS, the tagged cells may be retained in a magnetic column by magnetic force while other cells are eluted away. In FACS, by emitting and detecting the fluorescence

signals, tagged cells can be detected individually. They are then selectively charged and sorted out from other cells by electrostatic force. While MACS and FACS are effective and can target a wide range of cells, they also have limitations. For example, MACS requires the use of magnetic nanobeads and magnetic columns, which are expensive. Furthermore, since it only targets functional properties of cells, specifically surface-expressed proteins, sorting by size or other physical properties is difficult. In case of FACS, besides the high cost of reagents and equipment, the FACS machines are bulky, difficult to operate, and as a result, cannot be deployed in remote areas. Many of those limitations of MACS and FACS can be avoided by using microfluidic cell sorting techniques.

In general, microfluidic particle sorting technology makes use of micro- and nano-fabrication to produce features as small as cells or biological particles to easily manipulate them. In principle, cell sorting in microfludic devices can also exploit labels as in the case of MACS or FACS, for example using magnetic beads to alter the size and compressibility of cells for acoustophoretic sorting[28]. However, a large proportion of research in microfluidic particle sorting pursues the concept of *label-free sorting*. Instead of tagging the cells with magnetic or fluorescence label, this group of techniques exploit intrinsic physical properties to separate or enrich cells, and can be divided into two groups: active and passive methods. Active methods require an externally applied force field, for instance dielectrophoresis or acoustophoresis. Passive methods, on the other hand, rely on the internal intrinsic forces – the steric force between the particles and the devices' walls and the hydrodynamic force that the fluid exerts on the particles – together with careful geometrical designs to perform the sorting task. Below are some of the most popular microfluidic active and passive cell sorting methods. More extensive reviews can be found elsewhere[29,30].

Active methods:

- *Electrophoresis* exploits the difference in particles' electrophoretic mobility in an electric field to sort them accordingly. *Gel electrophoresis*[31] has long been used to sort DNA in agarose or polyacrylamide gels according to their size since mobility of longer molecules is reduced significantly due to their increased interaction with the pores of the gel. *Capillary electrophoresis,* on the other hand, sorts particles based on their effective charge (or more precisely, their zeta potential) as they travel along a long, thin glass capillary under an applied DC electric field. Capillary electrophoresis has also been successfully miniaturised on a glass chip[32].

- ▷ *Dielectrophoresis (DEP)*[33,34] makes use of the dielectrophoretic force acting on the particles in a non-uniform electric field. The force is dependent on the particles' size and effective polarisability (or more precisely, the Clausius-Mossotti factor, see Section 2.5). Therefore, the particles can be sorted by their sizes and/or their effective polarisability. An example is shown in Figure 1.1.

- ▷ *Acoustophoresis*[35] employs an acoustic standing wave force to induce lateral displacement of particles, perpendicular to the direction of flow. The force is dependent on the particles' size, density, and compressibility. Therefore, the particles can be sorted according to size, density, and compressibility (Figure 1.1).

- ▷ *Field Flow Fractionation (FFF)*[36] utilises a force field perpendicular to the flow to migrate particles into streams of different velocity in a parabolic flow profile, resulting in separation in retention time at the end of the channel.

Passive methods:

- ▷ *Pinched Flow Fractionation*[37] makes use of the fact that a particle cannot be closer to a wall than its radius to separate particles based on size (Figure 1.1).

- ▷ *Deterministic Lateral Displacement (DLD)*[38] is in principle a size-based method with the advantage of being continuous and high-resolution. A detailed description of DLD can be found in Section 2.2.

- ▷ *Inertial microfluidics*[39] operates in the middle range of Reynolds number where the flow is still laminar but the inertia of fluid and particles is considerable (see Section 2.1 for a description of laminar flow and Reynolds number). The inertial Dean flow in a curved channel and/or the inertial lift forces on particles are utilised to separate particles based on their size (Figure 1.1).

Let us now examine the possibility of *label-free particle sorting* being a mainstream practice in biomedical research, according the criteria proposed by Sackmann *et al.*[6]. First, considering fundamental novelty, it can be seen that while some techniques, for example microscale filters, improve upon the ideas which have been used to make their macro counterparts, other approaches, for instance Inertial Sorting or Deterministic Lateral Displacement, were completely new discoveries. When it comes to keeping the devices as simple as

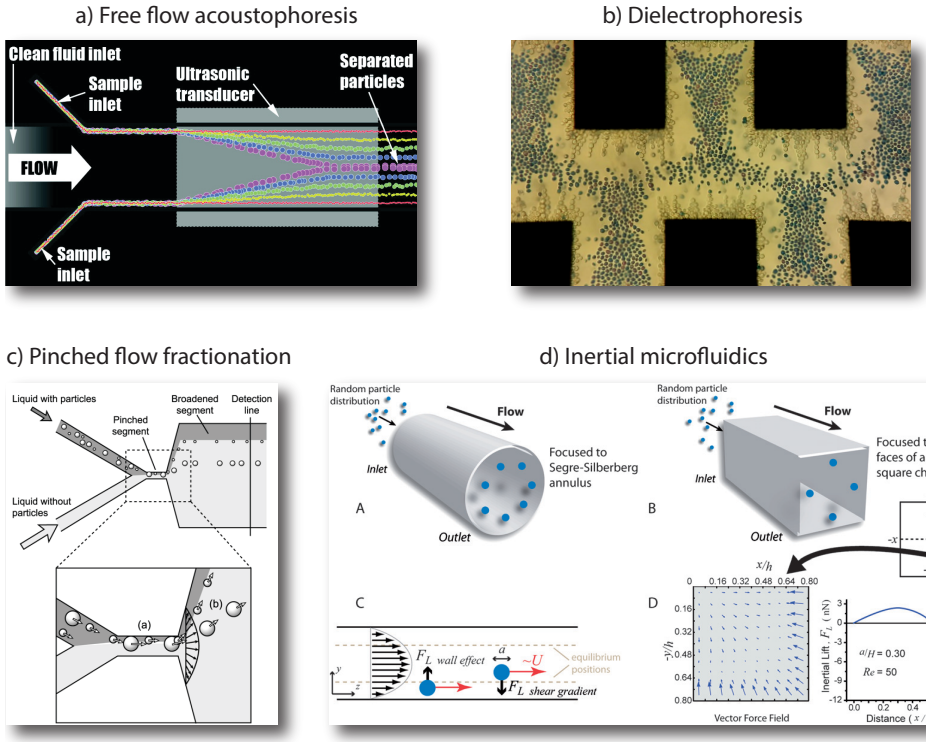

Figure 1.1: Examples of active (a,b) and passive (c,d) microfluidic label-free particle sorting methods. a) In free flow acoustophesis, particles are sorted laterally based on their size, density, and compressibility. Reprinted (adapted) with permission from Petersson *et al.* [35]. Copyright 2007 American Chemical Society. b) Under dielectrophoresis, non-viable yeast cells (stained dark blue) and viable yeast cells (transparent) migrate to different areas in a castellated electrode device, according to the sign of the dielectrophoretic force acting on them. c) With pinch flow fractionation, particles of different size can be sorted because the centre of small particles can be closer to the wall than that of big particles. Reprinted (adapted) with permission from Yamada *et al.* [37]. Copyright 2004 American Chemical Society. d) When the Reynolds number is larger than unity, particles experience inertia lift forces that are dependent on their size and their position in the cross-section of a channel. This can be exploited to focus particles of different sizes at different positions an separate them. Republished (adapted) with permission from Di Carlo [39]. Copyright 2009, the Royal Society of Chemistry.

possible to lower the entrance threshold for biomedical technicians or end-users, most of the passive techniques are good candidates since they usually need only a pressure generator, which can be as simple as a syringe. Active mechanisms often need some sort of apparatus to generate the required force field. However, those apparatuses can be redesigned and simplified to adapt to the local infrastructure. The third and forth criterion – fostering collaborations between physicists/engineers and biologists/medical experts and finding the right problems to solve – are open questions, since they are not dependent on the techniques but rather are determined by the needs and the incentives of the professionals involved. Nevertheless, as the most important purposes of label-free particle sorting are to avoid using ex-

pensive reagents and to produce cheap and more widely available biomedical devices, this is a promising yet challenging area, which can stimulate collaborations between scientists and companies in multidisciplinary fields. An example of such collaborations was LAPASO, the Label-free Particle Sorting research project funded by the People Programme (Marie Curie Actions) of the European Union's Seventh Framework Programme. The LAPASO project has brought together a multidisciplinary consortium of eight full partners and seven associate partners in Europe and Africa to solve current problems in the fields of bacteriology, parasitology, and rare cells sorting, using label-free methods. Further information can be found at its website: `http://lapaso.org`.

The work in this thesis is narrowed down to Deterministic Lateral Displacement. The main focus is on extending the capabilities of this technique by exploiting, besides size differences, the electrical/dielectric properties and the morphology of the cells. The thesis is structured as follows. After this introduction, Chapter 2 presents the theory and modeling of Deterministic Lateral Displacement and Electrokinetics. Chapter 3 describes the methods and the practical details of the work. Chapter 4 summarizes the results of the thesis work, the related published articles and manuscripts intended for publications, and concludes the thesis. The appendix and the related papers are located at the end of the thesis.

Chapter 2

Theory and Modelling

It's easy to be complicated
but very difficult to be simple.
— Debasish Mridha

This chapter presents the theory of microfludics and electrokinetics, the two central topics of this research work. It also gives an overview of the related modelling and simulation work.

2.1 Fluid Dynamics in Microfluidic Systems

Following is a brief summary of the physics of fluid dynamics in microfludic systems. Further comprehensive reading may be found in several textbooks in fluid dynamics [40–42] or theoretical microfluidics [43,44].

The physics of continuum fluid dynamics is described by the Navier-Stokes equations. Despite their essence to many scientific and engineering fields, whether the general solutions to them exists is an unsolved mathematical problem [45]. Fortunately in many cases, the equations can be simplified. The Navier-Stokes equations for an incompressible flow, which is the case for microfluidic applications, consist of one vector equation describing momentum conservation and one scalar equation describing mass conservation [40]:

$$\rho\frac{D\mathbf{u}}{Dt} = \rho\mathbf{f} - \nabla p + \eta\nabla^2\mathbf{u} \tag{2.1}$$

$$\nabla \cdot \mathbf{u} = 0 \tag{2.2}$$

Here, ρ is the density of the fluid, $\mathbf{u}$ is the velocity field, $\frac{D}{Dt} = \frac{\partial}{\partial t} + \mathbf{u} \cdot \nabla$ is the material derivative, t is the time, $\mathbf{f}$ is the total body forces per unit mass, p is the pressure, and η is the dynamic viscosity of the fluid. Essentially, Equation 2.1 is the Newton's second law applied to a unit volume of fluid: the term on the left hand side is the rate-of-change of momentum while the terms on the right hand side are the body force (for example gravity or dielectrophoretic force) and the surface forces (pressure force and viscous sheer force). Since the density ρ is often uniform and known, the four unknowns (p and the three components of $\mathbf{u}$) can in principle be solved using Equation 2.1 and Equation 2.2. Nevertheless in practice, solving the general Navier-Stokes equations is hard because of the nonlinerity coming from the convective derivative of the velocity, $(\mathbf{u} \cdot \nabla)\mathbf{u}$.

Fortunately, Equation 2.1 can be reduced in microfluidic systems where the ratio between inertial effects and viscous effects, $Re = \frac{\rho u L}{\eta}$ (the Reynolds number), is normally under unity. Here, L is the characteristic dimension of the microfluidic channel. In a typical microfluidic device, assuming $\rho = 1000\ \frac{kg}{m^3}$, $\eta = 0.001\ \frac{kg}{m.s}$, $u = 100\ \frac{\mu m}{s}$, and $L = 10\ \mu m$, the Reynolds number is 10^{-3}, well below unity. In this case, the inertial term on the left hand side of Equation 2.1, $\rho\frac{D\mathbf{u}}{Dt}$, is negligible and the equation can be simplified into the *Stokes equation*, which is linear:

$$0 = \rho\mathbf{f} - \nabla p + \eta\nabla^2\mathbf{u}$$

The flow described by the Stokes equation is called *Stokes flow* or *creeping flow*. In such a scheme, the flow consists of non-mixing, turbulent-free parallel layers of fluid. In fact, the Stokes flow is a subset of a broader *low-Re* flow regime called *laminar flow*, where the Reynolds number is low enough for the fluid to be smooth, orderly, and free of any turbulent vortices ($Re \leq 800$[46]) . Laminar flow is the underlying mechanism for Deterministic Lateral Displacement (DLD), which will be discussed in the next section,

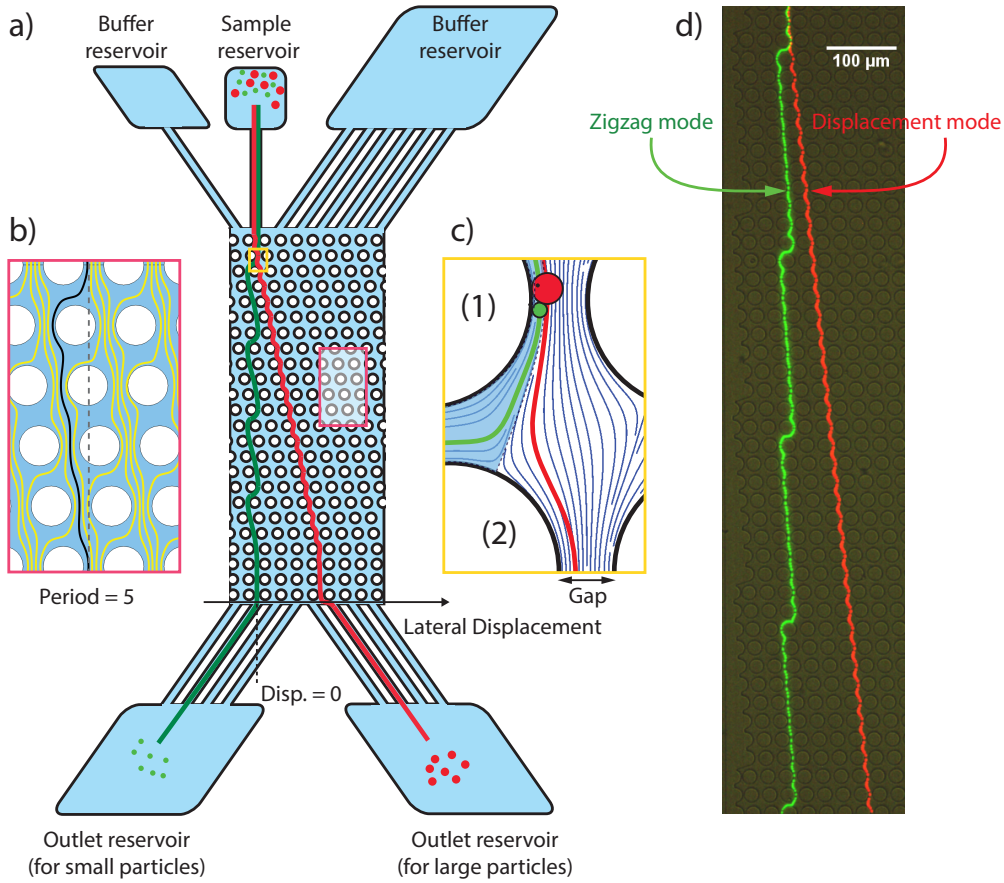

Figure 2.1: Principle of Deterministic Lateral Displacement. a) A schematic of a typical DLD device. The device consists of three parts: the inlet reservoirs on the top, the pillar array in the middle, and the outlet reservoirs at the bottom. It is capable of sorting a mixture of big (red) and small (green) particles into homogeneous populations. b) Periodic streamlines in the channel due to the pillar array. c) The underlying mechanism of size-dependent separation in DLD. The centre of mass of the green particle resides within the blue stream, whereas the centre of mass of the red one locates outside of the blue stream. Therefore, the two particles follow two different trajectories. (The streamlines in b) and c) are based on actual simulations.) d) Colour-coded micrograph of polystyrene beads, $2.1\ \mu m$ (green) and $4.3\ \mu m$ (red), in a pillar array having an estimated critical diameter, $D_C = 2.8\ \mu m$.

to be "deterministic". As DLD is a continuous hydrodynamic particle sorting technique, it relies on the flow behaviour being predictable in time and space. Consequently, DLD relies on being operated in the laminar flow regime.

2.2 Deterministic Lateral Displacement - Basic Principle

A typical device based on deterministic lateral displacement (DLD) (Figure 2.1a, not to scale) consists of three parts: the inlet reservoirs on the top, the sorting array in the middle, and the outlet reservoirs at the bottom. The middle inlet reservoir – the sample reservoir – contains a heterogeneous sample suspended in a running medium. The two inlet reservoirs on the sides – the buffer reservoirs – help maintain straight flow throughout the sorting array. The sorting takes place in a section consisting of an array of micrometre-sized pillars in a shallow channel of rectangular cross-section. The pillars are positioned so that the principle direction of the pillar array lattice forms an angle with respect to the channel wall. The outlet reservoirs accommodate the homogeneous populations being separated. The size of a DLD device is dependent on the intended application but its dimensions are typically on the order of $length \sim 1\ cm$, $width \sim 1\ mm$, and $depth \sim 10\ \mu m$. Detailed information about the devices in this thesis work is given in the Appendix (Chapter 5).

The arrangement of the pillars and the laminar nature of the flow are fundamental to the operation of DLD. The presence of the pillar array, tilted with a specific angle with respect to the overall flow direction, bifurcates and diverts the otherwise straight flow into many "zigzagging" streams around the pillars, as illustrated by the simulated streamlines in Figure 2.1b. If the pillar array is periodic, thanks to the turbulence-free and predictable nature of laminar flow, a flow stream would appear at the same lateral position after every period, as exemplified by the black streamline in Figure 2.1b.

This laminar and periodic flow pattern is the underlying mechanism for particle separation. As can be seen in Figure 2.1c, since pillar 2 is shifted to the right of pillar 1, it bifurcates the flow into two streams: one to its left (light blue) and one to its right (white). When spherical particles are transported near to the surface of pillar 1, the distance from the wall to the centre of a small particle is less than to the centre of a large particle. Depending on whether the centres of the particles reside within the blue stream (the green particle) or outside the blue stream (the red particle), they will travel through the DLD array in either a zigzag trajectory or a displacement/bumping trajectory, repectively. Particles traveling in zigzag mode return to the same lateral position after each period while particles traveling in displacement mode are transported along the tilting angle of the pillar array. This results in separation. As an example, Figure 2.1d shows the trajectories of 2.1 μm (green) and 4.3 μm

(red) polystyrene beads in a DLD array having the gap width between pillars of 6 μm and the period of 10.

The *critical diameter* above which particles traveling in displacement mode can be calculated assuming laminar flow with parabolic velocity profile between two posts of a row[47]. Beech and Tegenfeldt came up with a close-form analytical approximation for the critical diameter[48]:

$$D_C = 1.2GN^{-0.5} \tag{2.3}$$

where D_C is the critical diameter, G is the gap between two posts in a row (Figure 2.1c), and N is the period of the array. Another estimation for the critical diameter was proposed by John Davis[49], based on an empirical study:

$$D_C = 1.4GN^{-0.48} \tag{2.4}$$

For the pillar array shown in Figure 2.1d, Equation 2.3 and Equation 2.4 give $D_C = 2.3\mu m$ and $D_C = 2.8\mu m$, respectively, differing by around 20%. For the case exemplified in Figure 2.1d, the actual critical diameter was experimentally found to be larger than 3.1 μm, meaning that Equation 2.4 in this case gives a more realistic estimation of the resulting separation. This equation is also more commonly used when fabricating DLD devices. However, it should be stressed that both equations only give approximations of the resulting separation. Further studies are required to reveal a more accurate relationship between the critical size and the device geometries and the properties of the liquid and the particles.

2.3 Deterministic Lateral Displacement - Status of Theory, Technology, and Applications

2.3.1 Theory and Simulation

Theoretical work on DLD can be categorised broadly into two main branches. One branch focuses more on the structure of the flow and the other focuses more on the particle-obstacle interaction. In the first approach, the authors base their calculations on laminar flow to determine the flow profile and the distribution of flow streams in a pillar array. The flow profile and flow stream distribution are then employed to infer the trajectories of particles according to their size, without any explicit assumption about the interaction between the particles and the obstacles besides the impenetrability condition. This approach was employed in the first DLD paper[38] to explain the working principle of DLD and later in other works to estimate the critical diameter in a circular pillar array[47] or in a triangular pillar array[50]. The second theoretical approach, on the other hand, attempts to describe the irreversible particle-obstacle contact by a characteristic parameter while making no reference to the structure of the flow. This approach, so called "directional locking", was also successful in correlating theoretical calculations with experimental results, obtained in macro scale DLD arrays[51–61]. In addition, a model based on advection-diffusion theory claiming to bridge the two main aforementioned approaches has been published.[62].

Numerical simulation research on particle separation using DLD can be sorted into two main groups: Finite Element Method or a combination of Lattice Boltzmann Method (LBM), Finite Element Method (FEM), and Immersed Boundary Method (IBM). In the first approach, the Navier-Stokes equations are solved for the fluid flow, the mechanical deformation of the solid particles is also solved, and the fluid and the solid phase are connected using Fluid-Structure Interaction (FSI) algorithms[63,64]. In cases where the particles are hard spheres and are small compared to the gap between pillars, the two-way coupling scheme (FSI) can be simplified into a one-way coupling scheme where the particles were modeled as point-like objects whose minimum distance to pillar walls equals the actual particles' radius[62,65–69]. The second simulation approach employs the Lattice Boltzmann Method to resolve fluid velocity instead of solving the Navier-Stockes equations. The membranes/surfaces of the particles are modeled as a spring network and solved using FEM whereas the fluid-structure interaction is solved using the Immersed Bound-

ary Method[70–73]. In addition to the FEM or LBM/FEM/IBM approach, researchers also employed Finite Difference Method + IBM[74], Fictitious Domain Method[75], or Smoothed Dissipative Particle Dynamics (SDPD)[76] for numerical studies of DLD. Most notably, Henry *et al.*[76] showed qualitative agreement between the dynamics of Red Blood Cells in their models with the dynamics of the cells in DLD.

Future works on numerical simulations of DLD should preferably attempt to correlate with experimental data to help with the designing and optimising process. It is also of interest to accurately capture the behaviour of arbitrary particles (*e.g.* bacteria or other bioparticles with complex properties) in DLD devices to explore new sorting schemes.

2.3.2 Technology

Chip materials

The two most popular materials for fabrication of DLD devices are silicon[38,77,78] and polydimethylsiloxane (PDMS)[79–81]. Silicon etching techniques allow fabrication of well-defined pillars and very narrow gaps but the process can be complicated and difficult to replicate. Soft lithography using PDMS, on the other hand, allows for rapid and cheap device prototype fabrication, but high-aspect ratio pillars can often be difficult to achieve due to limitations in the processing steps. To reduce the cost of making chips and to improve scalability, attempts have also been made to produce DLD chips in plastic[82,83].

Design

Much of the attention on the design of DLD has been paid to optimising pillar shape, both experimentally and numerically. In general, it has been proven that if the cross-section of the pillars is a triangle[50,84–90], a square[72,87], an I shape/L shape[72,91–93], a diamond shape[87], an egg shape[94], or a specific topological optimised shape[95], the same critical diameter is achieved at a larger gap width than in the case of circular pillars. As a consequence, the DLD array is less prone to clogging and at the same time, the volumetric throughput will increase. There are also other added benefits of using special shapes. For example, the airfoil shape[96] was believed to reduce deformation of soft particles. The I-shape/L-shape pillars were found to induce rotational movement of non-spherical cells[91,92], which in turn helps distinguish particles based on their morphology. Another way which has been successful at sorting

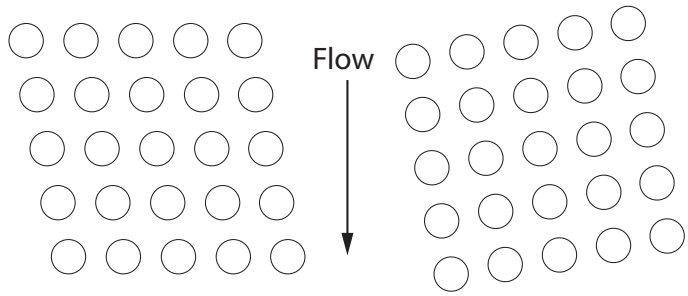

Figure 2.2: Two ways of implementing array's tilting angle: rhombic array (left), where the rows are perpendicular to the flow, and rotated square array (right), where the rows are perpendicular to the columns.

particles based on their morphological differences is to impose an orientational constraint by decreasing the channel depth down to below the largest dimension of a particle with aspect ratio larger than unity (*i.e.* long or thin particles). This has been employed to sort trypanosomes from blood[97,98] or Circulating Tumour Cell (CTC) clusters from blood[93].

At a larger scale, researchers have been working on improving the performance of the whole pillar array. There are two ways of implementing the tilting angle of the array: rhombic configuration and rotated square configuration (Figure 2.2). The majority of DLD publications use the rhombic configuration. The advantage is that it is easier to correct for boundary effects near the edges of the device, as well as, to interface two sections having arrays of different angles. However, it has been pointed out recently that the rotated square configuration is more immune to anisotropic permeability[99].

Attempts have been made to reduce unwanted effects in DLD caused by the tilting angle of the array, including the wall effect[100] and the anisotropic permeability effect[99,101–103]. The wall effect is due to the finite width of the array while the anisotropic permeability effect is because of the array tendency to induce a lateral pressure gradient perpendicular to the overall flow direction. To increase throughput, Loutherback *et al.* proposed mirroring an array next to the other[50] and this idea has been appreciated by other researchers[104,105].

Driving Mechanisms

While most of DLD experiments employ a pressure difference across the device to induce the flow and in turn to transport the particles, it has been demonstrated that other driving mechanisms also have their benefits. For example, gravity-driven[55,61], centrifugal force-

driven[60], or capillary force-driven DLD[106] may conceivably be useful in distant places where pressure pumps or syringe pumps are impractical. Electroosmotic-driven DLD[38,58], due to the plug flow profile, can yield smaller critical diameters than in the pressure-driven DLD[47].

Tuning critical diameter or sorting by parameters other than size

Not limited to improving DLD by optimising design or employing new physical mechanisms, researchers have also attempted to extend its capabilities by adding tunability. Interesting examples include tuning the critical diameter of a DLD array by deforming the device[80] or by applying electrokinetic forces[107]. These implementations on one hand complicate the operation of DLD devices, but on the other hand, extends the dynamical range of the device. The critical diameter can also be altered if a non-Newtonian fluid is used instead of aqueous media[63].

It has further been shown that DLD is capable of discriminating between particles based on properties additional to size. For example, the deformability of Red Blood Cells has been shown experimentally[108] and numerically[70,73,76,87] to affect their trajectories in a DLD device. Similarly, morphology of RBCs and trypanosome[97], *S. pneumoniae*[109], or 3D-printed macro objects[59] has been shown to be an effective marker for separation using DLD.

2.3.3 Applications

Since its inception, DLD has been employed to effectively separate a wide range of particles for biological and medical research. At the lower spectrum of size, around and below 1 μm, DLD has been used to concentrate exosomes[78], separate microvesicle from blood[110,111], sort DNA of different length[38], or fractionate bacteria based on chain length[109]. On the order of 10 μm, the technique has been employed for separation of nucleated RBC from blood[112], trypanosomes from blood[97,98], epithelial cells from fibroblasts[113], fungal spores from debris background[114], cardiomyocytes from heart tissue digest[115], MCF-7 cancer cells by size[89], viable Jurkat cells from nonviable apoptotic cells and their remnants[104], or droplets based on size[116,117].

A large part of DLD applications have been focused on the preparative or analytical separations of blood samples. Preparative separations comprise separations where the common goal is to enrich a certain subpopulation of the samples for further processing or downstream analysis. Examples include the separation of WBC from RBC or from blood as a whole[79,81,118] and furthermore, to take different blood components apart[77,119,120]. The other direction is analytical particle sorting where the sorting itself is the end goal of the analysis. This includes either analysing the distribution of a certain property among the cells in the sample, or detecting the presense of a certain cell in the sample, such as in the case of rare cell isolation and detection. A wide range of rare cells including parasites[97,98], PC3 cancer cells[88], or Circulating Tumour Cells (CTC)[85,90,93,94,121] have been enriched and detected using DLD.

In summary, during fourteen years, DLD has been central to a wide range of theoretical, engineering, and biomedical studies. Thanks to the relative maturity of the field, it can be hypothesised that future work will lean towards development of products based on DLD. Examples could be inexpensive point-of-care diagnostic chips[98], integrated chips where DLD is one component[94], or high throughput DLD chips which can process whole blood[81,88,94]. From a technological point of view, DLD devices which can sort nanoparticles or DLD devices which can specifically enrich rare cells from background would be highly appreciated. It should be noted that although the throughput of DLD devices can be improved by running at high pressures and/or by using parallelisation, the main strength of DLD is high resolution and this should be exploited in more applications.

2.4 Electrokinetics

In this section, the term *Electrokinetics* is used as an umbrella term to refer to three phenomena which can be used for transport (*-kinetics*) under application of an electric field (*Electro-*):

- ▷ Electroosmotic flow: the transport of aqueous solutions using an electric field
- ▷ Electrophoresis: the transport of a charged particle using an electric field
- ▷ Dielectrophoresis: the transport of a dielectric particle using a non-uniform electric field

Electrophoresis is fundamentally caused by electroosmotic flow around a particle. Both electroosmotic flow and electrophoresis are related to the charges at the interfaces between an electrolyte solution and a solid wall, which can be the wall of a device or the surface of a particle. Dielectrophoresis is related to the polarisation the particles and the medium and does not require the particles to be charge. To keep this section at reasonable length, dielectrophoresis will be discussed in the section. More detailed treatment of AC electrokinetics can be found in the book by Morgan and Green[122].

2.4.1 The Electrical Double Layer

The electrical double layer is the basic concept underlying electroosmotic flow and electrophoresis. When a charged object is embedded into an electrolyte solution, the ions of opposite polarity from the solution, counter-ions, are attracted to the surface of the object and electrically screen it[1]. Over a century, scientists have proposed, developed and refined theories to explain and quantify the double layer. The most commonly used model nowadays was proposed by Bockris *et al.*[123 124]. According to this model, as illustrated in Figure 2.3a), the region of electrolyte solution closest to the object surface consists of solvent dipoles, usually water molecules, and ions of both polarities (co-ions and counter-ions). The plane passing through the loci of bounded dipoles and ions is called *the inner*

[1]Even a neutral object, for example a glass or PDMS surface, can become charged in aqueous solution. In case of glass or PDMS, the terminated –OH group will dissociate into $-O^-$ and H^+ in an aqueous solution. This creates the necessary asymmetry between the stationary charge (the negative ionised hydroxyl groups) and the mobile ions in the double layer.

Helmholtz plane. Farther away from the surface is a region of hydrated counter-ions. The plane passing through the loci of hydrated ions is named *the outer Helmholtz plane.* The layer residing between the object surface and the outer Helmholtz plane, consisting of molecules and ions bounded to the object surface, is called *the Stern layer*. Outside the Stern layer, hydrated ions can move relative to the object surface. The counter-ions in this outer layer "diffuse" into the bulk electrolyte solution, or in other words, the charge density reduces exponentially to zero, reaching neutrality. Therefore, this layer is called the *the diffuse layer*. The term *double layer* refers to the Stern layer and the diffuse layer.

The electric potential in the electrical double layer – the Poisson - Boltzman equation.

The electric potential in the diffuse layer can be described by the Possion equation:

$$\nabla^2\phi = -\frac{\rho_q}{\varepsilon} \tag{2.5}$$

Where ρ_q is the volume charge density and ε is the permittivity of the medium. The volumetric charge density can be calculated applying the statistical *Boltzman law,* which states that the likelihood that a particle possesses an energy U_E is proportional to $e^{-\frac{U_E}{k_B T}}$, where e is the Euler's number, k_B is the Boltzmann constant, and T is the absolute temperature. Therefore the number density of the ions can be written as:

$$n = n_0 e^{-\frac{U_E}{k_B T}} \tag{2.6}$$

Where U_E is the electric potential energy of the ions, and n_0 is the number density of ions in the bulk solution. The electric potential energy can be expressed in the electric potential by: $U_E = zq\phi$, where z is the charge number, and q is the elementary charge. Equation 2.6 becomes:

$$n = n_0 e^{-\frac{zq\phi}{k_B T}} \tag{2.7}$$

And since $\rho_q = nzq$, Equation 2.5 becomes:

$$\nabla^2\phi = -\frac{zq}{\varepsilon} n_0 e^{-\frac{zq\phi}{k_B T}} \tag{2.8}$$

When there are many ionic species in the electrolyte solution, one has:

$$\nabla^2\phi = -\frac{q}{\varepsilon}\sum z_j n_{0j} e^{-\frac{z_j q\phi}{k_B T}} \tag{2.9}$$

which is known as *the Poisson-Boltzman equation*. Here the subscript j denotes the ions of type j. Since the potential ϕ appears at both sides of the equation, an analytical solution is difficult. However, approximations can be made in some special cases.

The Debye-Hückel theory. If we assume that the potential ϕ is small, we can approximate the exponential term by first order Taylor approximation: $e^x \approx 1 + x$ for small x. Thus, Equation 2.9 becomes:

$$\nabla^2\phi = -\frac{q}{\varepsilon}\sum z_j n_{0j}(1 - \frac{z_j q\phi}{k_B T}) \tag{2.10}$$

Due to the charge balance, $\sum z_j n_{0j} = 0$, we come up with a linear ordinary differential equation:

$$\nabla^2\phi = \frac{\phi}{k_B T}\frac{q^2}{\varepsilon}\sum z_j^2 n_{0j} \tag{2.11}$$

Denoting $\kappa^2 = \frac{q^2}{\varepsilon k_B T}\sum z_j^2 n_{0j}$, Equation 2.11 can be simplified to:

$$\nabla^2\phi = \kappa^2\phi \tag{2.12}$$

The Debye-Hückel theory is equivalent to the thick double layer limit, applied for ions. Thus, it should be solved using spherical coordinates. To illustrate, we simplify the problem to 1D, then Equation 2.12 has solution of the form: $\phi(r) = \phi_1 e^{\kappa r} + \phi_2 e^{-\kappa r}$. Solving this ODE with appropriate boundary conditions ($\phi(r = \infty) = 0$ and $\phi(r = 0) = \phi_0$) yields[2]:

$$\phi_r = \phi_0 e^{-\kappa r} = \phi_0 e^{-r/\lambda_D} \tag{2.13}$$

[2]Here a model simpler than the one in Figure 2.3a is assumed. The outer Helmholtz plane is supposed to coincide with the surface, and so: $\phi_d = \phi_0$.

One can see that at a distance of λ_D, called *the Debye length*, the potential falls off to $\frac{1}{e}$ of its maximum value. Also, λ_D is inversely proportional to $\sqrt{\frac{1}{2}\sum z_j^2 n_{0j}}$, the square root of the *ionic strength* of the electrolyte solution. Increasing the concentration of the electrolyte will increase the ionic strength of the solution and as a result, decrease λ_D.

For a symmetric monovalent electrolyte solution like *KCl*, the Debye length can be calculated as:

$$\lambda_D = \kappa^{-1} = \sqrt{\frac{\varepsilon k_B T}{2q^2 n_0}} \tag{2.14}$$

where ε is the permittivity of the solution, k_B is the Boltzmann constant, T is the absolute temperature, q is the elementary charge, and n_0 is the number density of the ions in the bulk. For a 1M KCl solution at room temperature: $\varepsilon = 80 \times 8.85 \times 10^{-12}\ F/m$, $k_B = 1.38 \times 10^{-23}\ J/K$, $T = 293\ K$, $q = 1.60 \times 10^{-19}\ C$, $n_0 = 6.02 \times 10^{26}\ m^{-3}$, the Debye length is $0.305\ nm$. For a $1\ mM$ KCl solution at room temperature ($\sigma \simeq 15\ mS/m$), $\lambda_D = 9.6\ nm$.

The Gouy-Chapman theory. If we assume that the thickness of the double layer is much smaller than the curvature of the charged object (the think double layer limit), the object can be considered planar, then Equation 2.12 can be reduced to 1D problem and solved analytically. The solving method can be referenced from the book "Colloidal Dispersions" of Russel *et. al.*[125] (page 101). The potential is found to be:

$$\phi = \frac{2k_B T}{q} ln\left(\frac{1+\gamma e^{-\kappa y}}{1-\gamma e^{-\kappa y}}\right) \approx \frac{4k_B T}{q}\gamma e^{-\kappa y} \tag{2.15}$$

where $\gamma = tanh\left(\frac{q\phi_0}{4k_B T}\right)$. We can see that when $\phi_0 \to 0$, Equation 2.15 becomes Equation 2.13, the Debye-Hückel approximation with 1D assumption.

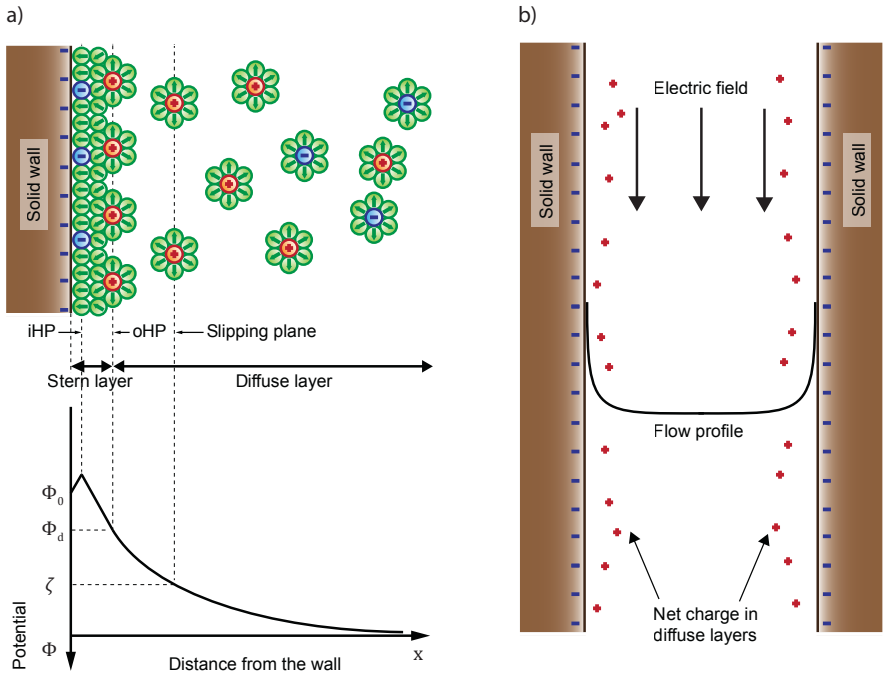

Figure 2.3: The electrical double layer and its relation to electroosmotic flow. a) Structure of the electrical double layer; b) Mechanism of the electroosmotic flow

2.4.2 Electroosmotic Flow

It has been known for more than two hundred years that an applied voltage can be used to transport an electrolyte solution in a channel with charged walls[126]. This phenomenon can be explained by the theory of the *electrical double layer*. Due to the structure of the electrical double layer, for the case in Figure 2.3a, the potential drops exponentially (in absolute value) from the outer Helmholtz plane into the bulk electrolyte solution. The charge density also decreases exponentially from the outer Helmholtz plane into the bulk electrolyte solution. Therefore, there is a net charge in the diffuse layer. If an electric field is applied tangential to the wall, as illustrated in Figure 2.3b, at some certain plane in the diffuse layer, called the *slipping plane*, the counter charges will move, dragging the fluid with them to form a plug-like flow profile. In essence, the slipping plane separates mobile fluid from stationary fluid that remains attached to the surface. The potential at the slipping plane is called the *zeta potential* ($\zeta - potential$). The electroosmotic flow velocity is related to the zeta potential of the wall via the Helmholtz– Smoluchowski equation:

$$u_{eof} = -\frac{\varepsilon \zeta_w}{\eta} E_t \tag{2.16}$$

Here u_{eof} is the electroosmotic flow velocity, ε is the permittivity of the fluid, ζ_w is the zeta potential of the wall, η is the viscosity of the fluid, and E_t is the electric field component tangential to the wall.

It is convenient to define the *electroosmotic mobility,* which is the ratio between the electroosmotic velocity and the tangential electric field:

$$\mu_{eof} = \frac{u_{eof}}{E_t} = -\frac{\varepsilon \zeta_w}{\eta}$$

2.4.3 Electrophoresis

The electrical double layer also forms when a charged particle is in contact with an electrolyte solution. In this situation, the relation between the size of the particle and the thickness of the double layer needs to be considered. If the particle is roughly one micrometer or bigger, which is typically much larger than the thickness of the double layer (several nanometers), similar arguments as with electroosmotic flow can be used and the electrophoretic velocity can be calculated as[127,128]:

$$u_{ep} = \frac{\varepsilon \zeta_p}{\eta} E \tag{2.17}$$

Here u_{ep} is the electroosmotic flow velocity, ε is the permittivity of the fluid, ζ_p is the zeta potential of the particle's surface, η is the viscosity of the fluid, and E is the applied electric field. This equation is very similar to the equation of electroosmotic flow (2.16), only with the difference in sign. It is because in both cases, the physical chemistry effects are the same, only that Equation 2.16 expresses fluid velocity with respect to a wall while Equation 2.17 calculates the particle (wall) velocity with respect to the fluid, hence the sign difference.

It is, again, convenient to define the *electrophoretic mobility,* which is the ratio between the electrophoretic velocity and the electric field:

$$\mu_{ep} = \frac{u_{ep}}{E} = \frac{\varepsilon \zeta_p}{\eta}$$

When the particle size is comparable to the Debye length, which is in the limit of a thick double layer, a different equation for electrophoresis should be used[128]:

$$u_{ep} = \frac{2\varepsilon \zeta_p}{3\eta} E \tag{2.18}$$

which has similar form to the case of the thin double layer, only that the coefficient has changed from 1 to $\frac{2}{3}$.

2.4.4 Measurement of Phase Lag between Electroosmotic Flow and Electric Field

The normal situation in electrokinetics, which is also the case in capillary electrophoresis, is that electroosmotic flow and electrophoresis take place simultaneously. Conceivably, they must have different response time because the inertia of the volume of a fluid is much larger than that of a single particle. If there is any phase lag between the movement of a bead when applying, for example, an AC sinusoidal field, it would be attributed to the slower response of electroosmotic flow.

To investigate this matter, electrokinetic experiments were performed in a DLD device with carboxylate-modified beads of 2 μm in diameter suspended in a 1.7 mM KCl solution, having the conductivity of $25 mS/m$. No electroosmotic suppressor (PVP or Pluronic F127) was used and the device was not exposed to elevated temperature after bonding (Section 3.1), all is to enhance the electroosmotic flow during the experiments. The high intensity LED lamp used to expose the fluorescent beads was synchronised with the AC voltage applied across the device. The electrical setup performing this task is shown in Figure 2.4.

The output sinusoidal signal from a function generator (15 MHz function/arbitrary waveform generator, model 33120A, Hewlett Packard, Palo Alto, CA, USA) was amplified

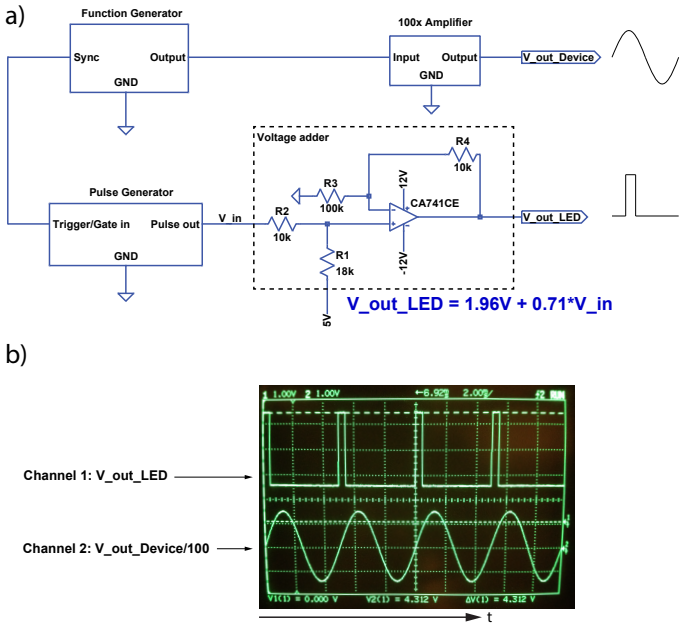

Figure 2.4: Synchronisation of the rectangular pulses of the LED light and the AC voltage applied to the device. a) Schematic of the electrical setup. b) Oscilloscope screen showing the syncronised voltages fed to the LED and to the device

100 times by a Bipolar operational power supply/amplifier (BOP 1000M, Kepco, Flushing, NY, USA) whose output was applied across the device. The sinusoidal signal from the function generator was synchronized with a rectangular signal from a pulse generator (TGP110 10MHz Pulse generator, Thurlby Thandar). The duty cycle of the rectangular signal was adjustable, capable of providing a very short pulse to the LED. An op-amp voltage adder circuit was used to raise the lower level of the rectangular signal to a value above zero, making the beads visible even between the peaks. As a result, an observer would see the beads at high intensity of light for a short period of time and at low intensity between peaks. The trigger of the pulse generator was adjusted to coincide with the beginning of the sine wave (Figure 2.4b). The phase lag between the electrokinetic oscillation of the beads (due to electroosmotic flow and particle electrophoresis) and the sinusoidal signal, if exists, can be pinpointed by the phase lag between the high intensity period and the starting point of each oscillation.

The results are shown in Figure 2.5. First of all, since the electroosmotic flow has positive mobility in PDMS channels[129], and since the terminal electrode was on the left and the ground electrode was on the right, the electroosmotic flow would be from the left

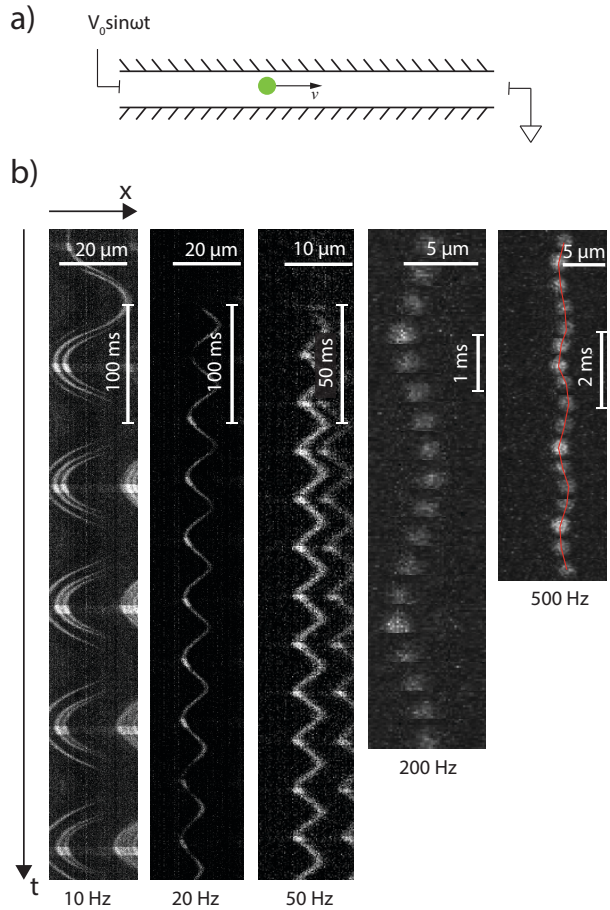

Figure 2.5: Experiments to measure the phase lag between electroosmotic flow and electric field. a) Schematic of the setup. b) Kymographs showing the positions of the beads as a function of time. The original videos were taken at 2100 frames per second. The spatial and temporal scales are different for each graph. In all cases, the terminal electrode was on the left and the ground electrode was on the right. For the case $f = 500\ Hz$, lines connected the centres of the bead at different time points have been drawn to guide the eyes.

to the right during the positive half cycle of the sinusoidal signal applied on the device. Here we also see the beads lit up before they move from the left to the right (most visible at 20 Hz), which confirms that the electroosmotic flow was dominant over the particle electrophoresis, which is in the opposite direction for the negatively charged beads used here. Second of all, the beads lit up precisely at the beginning of their motion from the left to the right at all frequencies up to 200 Hz, which implies that there was no visible lagging between the beads' oscillation (mainly due to electroosmotic flow) and the electric field. This may also be valid at 500 Hz, although the small amplitude of the oscillation at this

frequency made it difficult to confirm. In conclusion, electroosmotic flow is fast enough to keep pace with the electric field at all frequencies up to 200 Hz.

2.5 Dielectrophoresis

This section aims to give a brief overview of dielectrophoresis. More detailed treatments of the topic can be found in several textbooks in this field[122,130].

2.5.1 Simple Picture - a Dielectric Particle in a Dielectric Medium in a Static Electric Field

When a neutral dielectric particle is immersed into a dielectric fluid under a static electric field, both the particle and the fluid are polarised and charge of opposite sign accumulates at either sides of the interface. If the particle is so small that the electric field does not vary significantly across its dimensions, the induced polarisability can be approximated as a dipole moment and the force acting on it can be written using a linear approximation of the field:

$$\mathbf{F} = (\mathbf{P} \cdot \nabla)\mathbf{E} \tag{2.19}$$

Here $\mathbf{P}$ is the dipole moment and $\mathbf{E}$ is the electric field. Equation 2.19 shows that the force is non-zero only if the field is non-uniform.

To approximate the particle as a dipole, the *effective moment method* is employed[131]. The effective dipole moment of a spherical particle, for example, is the moment of a dipole which will produce an identical electrostatic potential, if placed at the centre of the particle. This method has been used to derive the effective dipole moment of a spherical dielectric particle in a dielectric medium[131]:

$$\mathbf{P} = 4\pi r^3 \varepsilon_m \frac{\varepsilon_p - \varepsilon_m}{\varepsilon_p + 2\varepsilon_m}\mathbf{E} \tag{2.20}$$

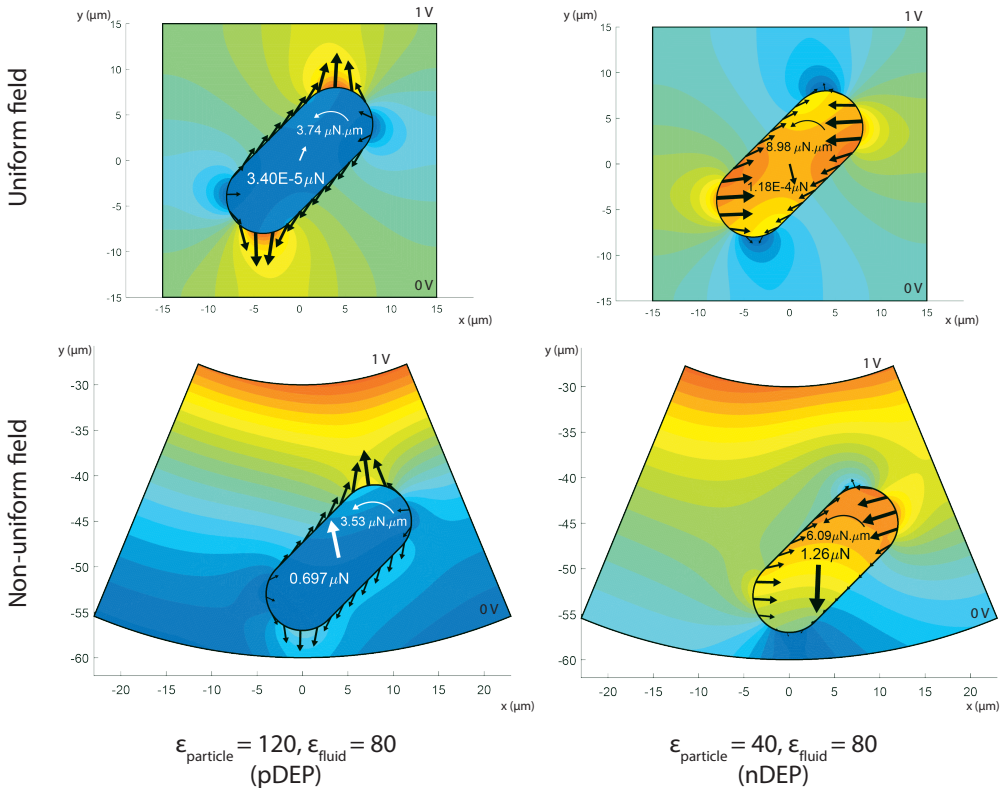

Figure 2.6: Numerical simulation of a rod-shape particle in a uniform or a non-uniform electric field. On the background is the magnitude of the field, on the boundary of the particle is the Maxwell surface stress tensor. Inside the particle, the DEP force and the torque acting on it are annotated. The arrows on the particle boundary has the same scale for all subfigure, while the arrows representing the DEP force and the torque are not for scale.

Here r is the particle radius, ε_m and ε_p are the permittivity of the fluid medium and the particle, respectively. It can be seen that the effective dipole moment is proportional to the volume of the particle and a term representing the "contrast" in permittivity between the particle and the medium, known as the *Clausius-Mossotti factor:* $f_{CM} = \frac{\varepsilon_p - \varepsilon_m}{\varepsilon_p + 2\varepsilon_m}$. Since $\nabla \times \mathbf{E} = 0$ and $\nabla(\mathbf{A} \cdot \mathbf{B}) = (\mathbf{A} \cdot \nabla)\mathbf{B} + (\mathbf{B} \cdot \nabla)\mathbf{A} + \mathbf{A} \times (\nabla \times \mathbf{B}) + \mathbf{B} \times (\nabla \times \mathbf{A})$, Equation 2.20 and Equation 2.19 can be combined to yield:

$$\mathbf{F_{DEP}} = 2\pi r^3 \varepsilon_m \frac{\varepsilon_p - \varepsilon_m}{\varepsilon_p + 2\varepsilon_m} \nabla |\mathbf{E}|^2 \tag{2.21}$$

When the particle has complicated shape or when the field varies significantly across the particle, the effective moment approximation can be erroneous. Instead, the dielectrophoretic force can be integrated from the Maxwell surface stress acting on the particle. Such calculations can be done in a numerical Finite Element Analysis software, for example COMSOL Multiphysics (Figure 2.6). Figure 2.6 illustrates the 2D simulation of a hypothetical rod-shape particle in a uniform and a non-uniform field. Several remarks can be made regarding the simulated results. First of all, it is clear that the DEP force in the uniform field is negligibly small, four to six orders of magnitude smaller than in the non-uniform field, although the Maxwell stress at the surface has comparable magnitude. Second of all, the DEP force points to the region of higher field when the permittivity of the particle is larger than that of the fluid (positive DEP) and to the region of lower field when the permittivity of the particle is smaller than that of the fluid (nDEP). Lastly, in all cases there are torques of the same order of magnitude which tend to rotate the particle counter-clockwise so that its length aligns parallel with the field.

2.5.2 Practical picture - the Particle and the Medium have Non-zero Conductivity, and an AC Field is Applied

In a typical microfludic device, the medium is an electrolyte solution and the ions within the solution contributes to its conductivity. The particle may also have a surface conductance (polystyrene beads) or internal conductivity (cells). Furthermore, the field is normally not a simple DC static field but an AC field, whose frequency in the range of kHz or MHz. Therefore, the dielectrophoretic force in Equation 2.21 is modified to include the conductivity of the particle and medium and the time average value of the field:

$$\mathbf{F_{DEP}} = 2\pi\varepsilon_m r^3 Re\left(\frac{\tilde{\varepsilon}_p - \tilde{\varepsilon}_m}{\tilde{\varepsilon}_p + 2\tilde{\varepsilon}_m}\right)\nabla|\mathbf{E_{rms}}|^2 \tag{2.22}$$

where $\tilde{\varepsilon}_m$, $\tilde{\varepsilon}_p$ are the complex permittivities of the particle and the suspending medium, defined as: $\tilde{\varepsilon} = \varepsilon - i\sigma/\omega$ (ε denotes the permittivity, σ denotes the conductivity, and ω is the angular frequency of the electric field).

For polystyrene beads, the bulk conductivity σ_b is negligibly small and their conductivity comes from the surface conductivity σ_s[122]:

$$\sigma_p \simeq \sigma_s = \frac{2K}{r} \tag{2.23}$$

where r is the radius and K is the surface conductance of the beads.

In the cases where cells are studied, their complicated structures can be modeled as a two-shell or three-shell sphere and the effective Clausius-Mossotti factor can be calculated from the contribution of each layer[130].

2.6 Simulation

When the geometry is complicated or when the mathematics is too complex to produce an analytical solution, especially when many physical mechanisms are involved, a numerical simulation based on differential equations and proper boundary conditions provides a rather direct, engineering way to look at the problems at hand. Simulation is also advantageous for approving or disproving novel ideas, since prototyping in microfludics is costly and time consuming. All the simulations in this work were built using COMSOL Multiphysics. The *physics*[3] used are summarized below and more details can be found in Table 2.1.

i. Stokes flow is used for calculating the velocity profile of the fluid in the devices. Since the Reynolds number of microfluidic devices is well below unity, the inertial component can be neglected. Also, since the fluid velocity is well below the speed of sound, the flow is assumed incompressible. The wall boundary condition can be non-slip (pressure driven flow) or slip boundary condition (electroosmotic flow).

ii. Wall distance is useful when calculating the distance from the centre of mass of a particle to a wall to apply a wall force. It is described using an *Eikonal equation.*

[3] *The physics* here are the names of the modules in COMSOL, which do not necessarily coincide with the concepts they suggest.

Table 2.1: Physics used in simulations. Meaning of symbols can be found at the List of Symbols on page xiii.

Physics	Differential equations/Boundary conditions	Meaning
Stokes flow	$0 = \nabla.\left[-p\mathbf{I} + \eta\left(\nabla\mathbf{u} + (\nabla\mathbf{u})^T\right)\right] + \rho\mathbf{f}$	Inertial term neglected (left hand side); surface forces and body forces adds up to zero (right hand side).
	$\rho\nabla.\mathbf{u} = 0$	Incompressible flow
	$\mathbf{u} = 0 \mid_{walls}$	No-slip boundary condition
	$\mathbf{u} = \mu_{eof}\mathbf{E}_\mathbf{t} \mid_{walls}$	Electroosmotic flow boundary condition
	$p = p_0 \mid_{inlet}, p = 0 \mid_{outlet}$	Pressure at the inlet and outlet of the device
Wall distance	$\lvert\nabla D_w\rvert = 1$	The norm of the gradient of wall distance is unity
	$D_w = 0 \mid_{wall}$	Wall distance is zero for the points on the wall
Electric current	$\nabla.\mathbf{J} = 0$	Continuity equation of current
	$\mathbf{J} = \sigma\mathbf{E}$	Ohm's law in steady state
	$\mathbf{J} = (\sigma + i\omega\varepsilon_0\varepsilon_r)\,\mathbf{E}$	Ohm's law in frequency domain
	$\mathbf{J} = \left(\sigma + \varepsilon\varepsilon_r\frac{\partial}{\partial t}\right)\mathbf{E}$	Ohm's law in transient state
	$\mathbf{E} = -\nabla V$	Definition of electric potential
	$V = V_0 \mid_{inlet}, V = 0 \mid_{outlet}$	Voltage at the inlet and outlet of the device
Particle tracing for fluid flow	$\frac{d}{dt}(m_p\mathbf{v}) = \mathbf{F_t}$	Newton's second law
	$\mathbf{F_d} = \frac{1}{\tau_p}m_p\,(\mathbf{u} - \mathbf{v})$	Drag force, Stokes form used for laminar flow
	$\tau_p = \frac{\rho_p d_p^2}{18\eta}$	Particle velocity response time for spherical particles in a laminar flow
	$\mathbf{F_w} = F_{w0} \times step\left(D_w - r_p\right) \times (-\mathbf{D_{dir}})$	Wall repulsive force
	$\mathbf{F_{DEP}} = 2\pi r_p^3\varepsilon_m Re\{f_{CM}\}\nabla\lvert\mathbf{E_{rms}}\rvert^2$	Dielectrophoresis force
	$f_{CM} = \frac{\tilde{\varepsilon}_p - \tilde{\varepsilon}_m}{\tilde{\varepsilon}_p + 2\tilde{\varepsilon}_m}$	The Clausius-Mosotti factor
	$\tilde{\varepsilon} = \varepsilon - j\frac{\sigma}{\omega}$	Complex permittivity

iii. Electric current provides solutions to the electric field in the device, which will be used later as an input to calculate electroosmotic flow and dielectrophoretic force. In this work, it is assumed that there is no current source or external current density.

vi. Particle tracing for fluid flow provides a computationally reasonable way to simulate dynamics of the particles in a DLD device under the combined action of pressure driven flow, electroosmotic flow, electrophoresis and dielectrophoresis.

Chapter 3

Device Fabrication and Experimental Setup

If you optimise everything,
you will always be unhappy.
— Donald Knuth

The research methodology is illustrated in Figure 3.1. The research ideas can come from either *a technological-driven approach* (literature and our previous work) or *an application-driven approach* (biological or medical needs). To probe the feasibility of the ideas, a modelling or simulation step can be performed (Section 2.6), but can be skipped if the implementation of the ideas is straightforward. The next step, device fabrication, includes several sub steps: designing and making photolithographic masks, making moulds, and finally casting and bonding devices. The details can be found in section 3.1. The experiments are then performed on the fabricated devices with model particles (*e.g.* polystyrene microspheres) or with cells and bioparticles. The results will be documented and recorded via a microscope equipped with optics and cameras (Section 3.2). In the next step, experimental data will be processed, analysed, and compared with simulation results. Normally, it takes several iterations through the previous steps before the results of the study can be ready for dissemination.

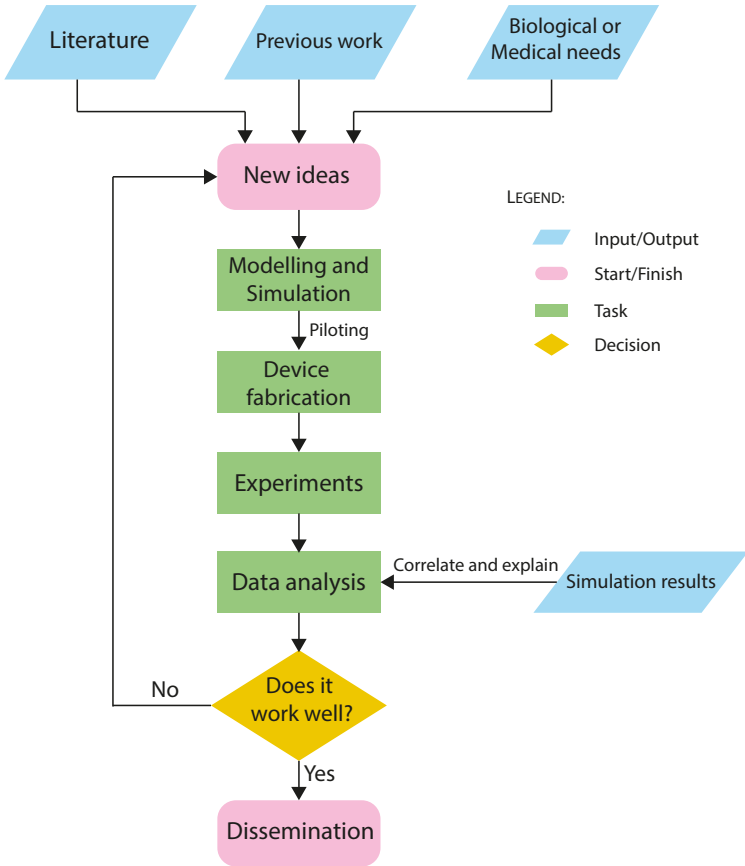

Figure 3.1: Typical methodology flow chart used for the work presented within this thesis.

3.1 Device Fabrication

All devices were cast from a silicon-based organic polymer called *polydimethylsiloxane*, normally abbreviated as PDMS. The material is transparent, non-toxic, impermeable to water but permeable to air and other gases, making it suitable for biomedical microfluidic devices. The making of a PDMS device is termed *soft lithography*[4]. It is relatively simpler and less equipment intensive than a conventional lithography process. However, to make the mould for soft lithogaphy, a conventional clean room lithography process using a photosensitive resist is required. The complete device fabrication procedure includes:

- Drawing of the devices' features on an electronic file. The CAD software named Tanner L-Edit (Mentor Worldwide LLC, Santa Barbara, California, USA) was used.

- ▷ Fabrication the chromium-coated glass mask. For the work presented within this thesis, the masks were outsourced to a mask manufacturing company (Delta Mask B.V., Enschede, The Netherlands). The mould for soft lithography was fabricated in Lund NanoLab by using a $10 - 50\ \mu m$ thick layer of the negative photoresist SU-8 on a silicon wafer. The SU-8 layer has the counterpart features of the features of the device, for example holes on the SU-8 mould correspond to pillars in the device. An antisticking step with *trichloro (1H,1H,2H,2H-perfluorooctyl) silane* (PFOTS) (Sigma Aldrich, Saint Louis, MO, USA) in vapour phase on the mould is needed to facilitate demoulding of PDMS. Several moulds can be fitted on a single 3-inch wafer, as illustrated in Figure 3.2.

- ▷ Generation of the PDMS imprint by soft lithography. This was carried out by mixing the monomer (Sylgard 184, Dow Corning Inc., USA) with its curing agent at a ratio of $10 : 1\ (w/w)$ and pouring it on the mould. The liquid PDMS on the mould is then cured at $80°C$ for an hour. The hardened PDMS layer is then peeled off from the mould, trimmed, perforated with access holes, treated with oxygen plasma, and bonded on a PDMS-coated glass slide. Thereafter, silicon tubing is added to act both as liquid reservoirs and as an interface to the pressure controller (Figure 3.2).

- ▷ An additional surface treatment of the DLD devices may be required for specific applications. In Paper II, to reduce sticking of *S. pneumoniae* to the PDMS walls, the devices were filled with PLL(20)-g[3.5]-PEG(2) solution after bonding for 20 minutes. In Paper I, the bonded devices were left in an oven at $120°C$ for 24 hours[132] to bring the PDMS surface back to its native hydrophobic state, making it stable for electrokinetic experiments.

The last three steps described above have been developed and optimised previously in our group and more details can be found in other publications[48,133]. The first step, the drawing and designing of DLD devices, is often the most time-consuming step due to the vast amount of features of a DLD array which need to be positioned precisely. However, this step can be sped up significantly by the implementation of software script into L-Edit, which automate the process. The script also reduces human errors when designing the separation arrays.

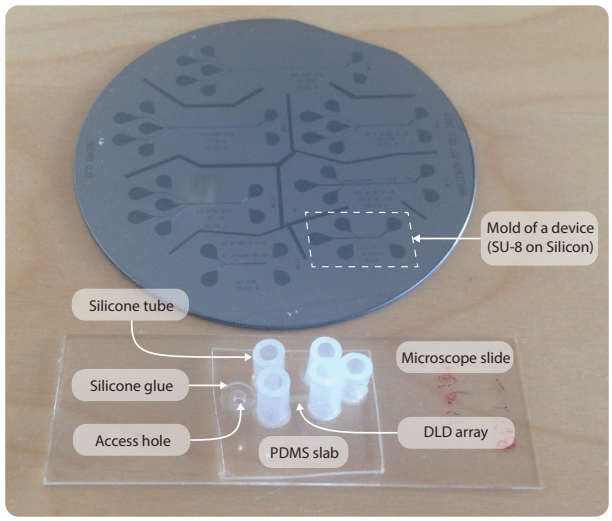

Figure 3.2: An SU-8 silicon wafer and a bonded PDMS device on a standard microscope slide.

3.1.1 Implementing Scripts for Automated Device Drawing

Although the finer details can be more complicated, a typical design of a DLD device is illustrated in Figure 3.3a. Unless internal electrodes are needed (Paper V), the device can be drawn on one single layer, corresponding to one single lithography mask. The green areas are hollow space where liquid can flow while the white areas are PDMS obstacles or walls. A typical device consists of inlet and outlet reservoirs, a pillar array where separation takes place, and channels connecting the array and the reservoirs. Within the array, the pillars are arranged inclined to the overall flow direction, facilitating deterministic lateral displacement (more details can be found in Section 2.1). Edge correction[100] is implemented to minimise wall effects and to ensure a symmetric flow pattern throughout the array. Two additional straight pillar arrays are positioned between the tilted array and the connecting channels to ensure that the particles move as they are expected when they enter and exit the tilted arrays.

L-Edit is a CAD software which allows users to draw basic shapes (rectangulars, circles, polygons, *etc.*) whose dimensions can be specified precisely, via a graphic user interface (GUI). It also provides various functions to transform these shapes. A complicated geometry, for example a DLD array, can be constructed from basic shapes via a hierarchical organisation. In this organisation, every design feature, from a basic shape to a whole

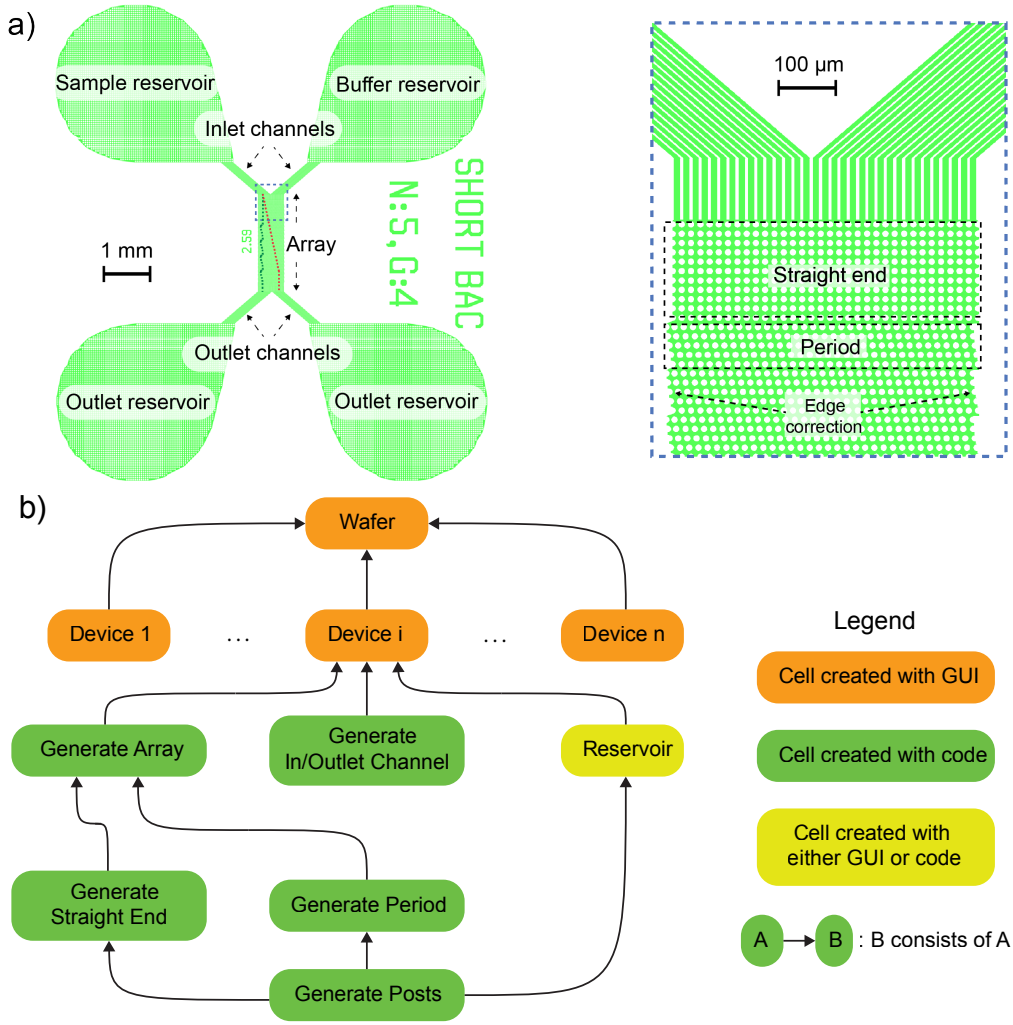

Figure 3.3: Design of DLD device. a) A typical design of a DLD device, b) The design is structured in a hierarchical order using cells in L-Edit.

device, is called *cell* and a cell at a higher hierarchical level can be built by populating it with instances of cells at a lower level, making it easy to modify or reuse a design. It also supports programmable drawing mode via *T-cell* (Template cell), in *C* language, allowing users to draw shapes of parameterised size or clone an array of shapes with parameterised quantity. Both the GUI and the programmable interface have their own advantages. The GUI provides flexible drawing and positioning of shapes in specific cases where programming is impossible, whereas the programmable interface enables designing and placing features in

a parametric and automatic manner. The two approaches can be combined to optimise the designing process.

A simplified process of designing the devices is described in the diagram of Figure 3.3b. The cells with green background are T-cells while the cells with orange background are created using the GUI. The reservoirs can be drawn either by code or by the GUI, depending on the specific situation. The design task starts with creating posts (pillars) (*Generate Posts*) and then arranging posts into arrays without or with a tilt with respect to the overall fluid direction (*Generate Straight End* and *Generate Period*). The straight ends and the periods are then combined into the array (*Generate Array*) and the connecting channels are also generated (*Generate In/Outlet Channel*). The reservoirs have some parts which can be programmed, but also some parts which can be done easier with GUI. A *Device* is then constructed by combining the array, the connecting channels, and the reservoirs. Finally, the devices are arranged so that they fit onto a *Wafer* of suitable size (*e.g.* a 3-inch wafer).

Although the procedure was described in a bottom up manner, when all the modules (T-cells) have been prepared, the designing process is carried out top down. For example, generating an array is performed by calling the corresponding T-cell with its own parameters without paying any attention to the T-cells at a lower levels (*Generate straight end*, *Generate period* or *Generate posts*), which makes the designing task easy and convenient. [1]

3.2 Experimental Setup

A typical experimental setup is shown in Figure 3.4. A pressure gradient was created by letting the outlet reservoir be open to the ambient air while connecting inlet reservoirs to an overpressure controller or a syringe pump. The setup presented here uses a $MFCS - 4C$ pressure controller (Fluigent, Paris, France), connected to the reservoirs of the device via silicone tubes and T-connectors. To bias the device with a voltage, holes were drilled through the elbow connectors and platinum electrodes were pushed through the holes, glued and embedded into the fluid in the reservoirs (Figure 3.4a).

[1] The source code for the T-cells used in this work to draw a DLD array can be found at bit.ly/DLDScript (case sensitive), and is free to use under CC 4.0 BY-NC.

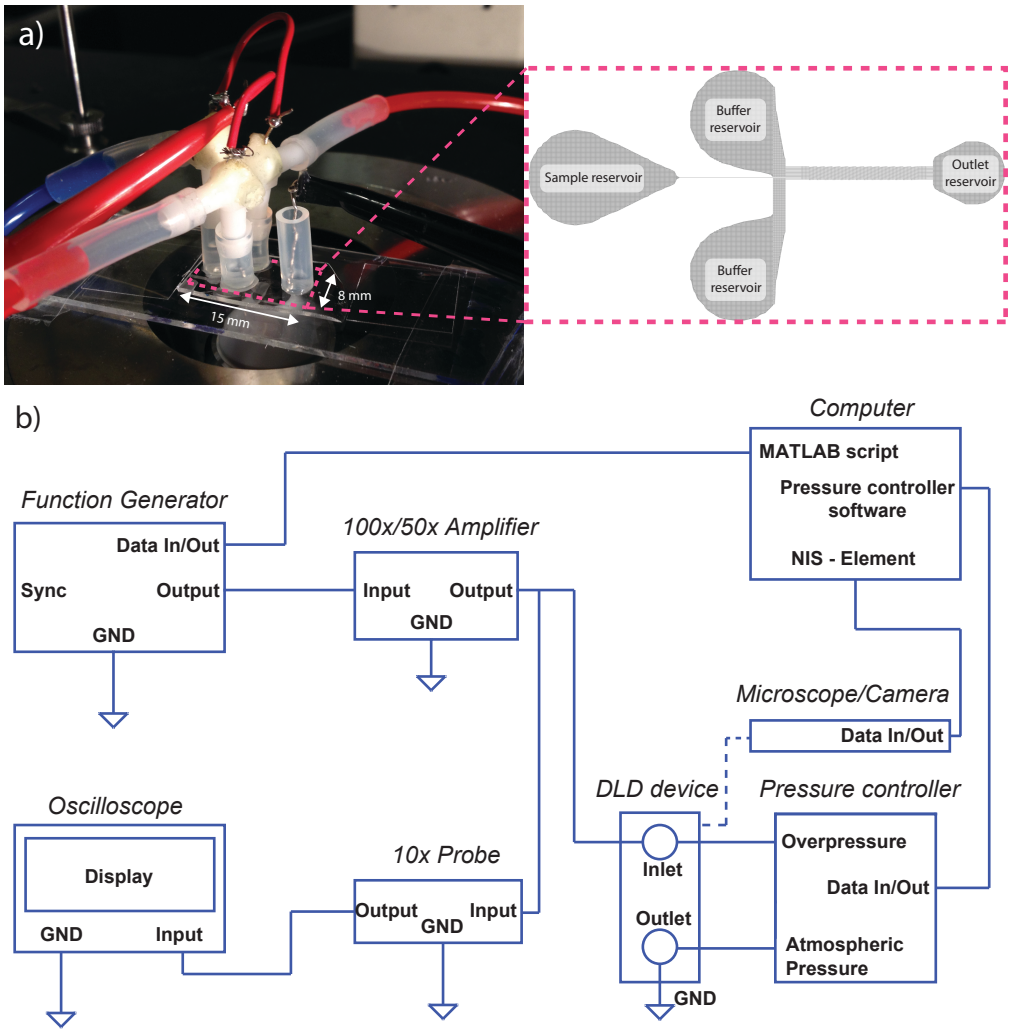

Figure 3.4: Experimental setups. a) Picture of a DLD device connected to tubing and electrical wiring (left), along with an overview of the layout of the device (right). b) Schematic of the full setup (Paper I, III, and IV). In Paper V, the amplifier was omitted. In Paper II, no electrical equipment was used.

To generate DC or AC fields, a function generator (15 *MHz* function/arbitrary waveform generator, model 33120A, Hewlett Packard, Palo Alto, CA, USA) was used and the signals were amplified 100 times by a Bipolar operational power supply/amplifier (BOP 1000M, Kepco, Flushing, NY, USA) to give a maximum voltage of 1000 V_{pp} at 1 *kHz*. Alternatively, a high-frequency, 50× amplifier (WMA-300, Falco Systems, Amsterdam, The Netherlands) can be used to give a maximum voltage of 300 V_{pp} at 1 *MHz*.

The voltage was measured using an oscilloscope (Hewlett Packard 54603B 60MHz), via a 10× probe (Kenwood PC-54, 600 V_{pp}). An inverted microscope (Nikon Eclipse TE2000-U, Nikon Corporation, Tokyo, Japan) and an Andor Neo sCMOS camera (DC-152Q-FI, Andor Technology, Belfast, Northern Ireland) were used to acquire the images and videos of the experiments. A colour camera (Exmor USB 3.0, USB29 UXG M) was used to capture colour video if necessary, for example in the experiments with non-fluorescen viable/non-viable yeast cells or with fluorescence viable/non-viable *E. coli*. The images captured from the camera were recorded into a computer hard drive using NIS Element software (NIS Element Advanced Research v4.51, Nikon).

Chapter 4

Summary of Results and Outlook

If I have seen further than others,
it is by standing upon the shoulders of giants.
— Isaac Newton

This chapter summarises the motivations and the main results of the papers and of the ongoing adipocyte sorting project, and discusses some conclusions and outlook.

4.1 Electrokinetic Deterministic Lateral Displacement (Paper I)

Size is probably the most common parameter in label-free particle sorting. Nevertheless, particles derived from an initial population, for example viable and non-viable cells of some kind, can be quite homogeneous in size. In those situations, parameters other than size need to be employed. Although DLD was originally a size-based method, it has been demonstrated that the effective size of polystyrene beads in a DLD device could be tuned with an AC voltage[107]. This suggests that electrical and dielectric properties of particles can be exploited as new parameters for separation in DLD devices.

In Paper I, we employed surface electric properties and dielectric properties of particles and cells to sort them in a DLD device. We have shown that by combining electrokinetics with DLD (Section 3.2) and tuning the AC frequency, similar-sized polystyrene particles

of differently modified surface properties could be sorted. Interestingly, using the same principle, viable and non-viable yeast cells and viable and non-viable *E. coli* bacteria could also be separated with high purity.

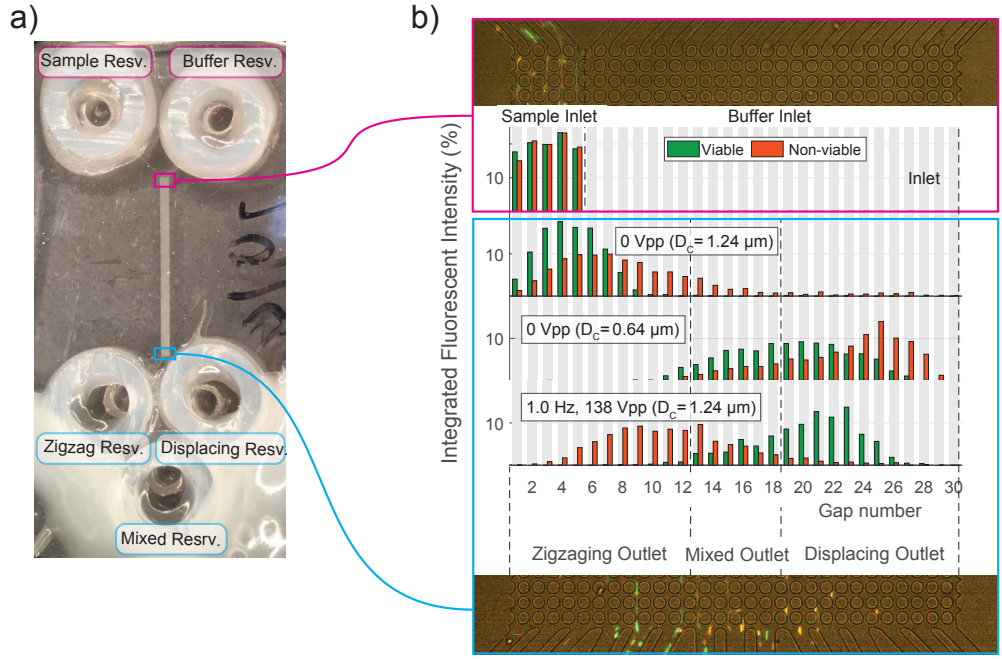

Figure 4.1: Separation of viable and non-viable *E. coli* using Electrokinetic DLD. a) Actual device sorting viable from non-viable *E. coli*. b) Distribution of *E. coli* at different gaps. First graph: inlet; second graph: outlet of a device having $D_C = 1.24\ \mu m$, no applied voltage; third graph: outlet of a device having $D_C = 0.64\ \mu m$, no applied voltage; fourth graph: outlet of a device having $D_C = 1.24\ \mu m$, when a voltage of 1 Hz, 138 Vpp was applied.

Figure 4.1b illustrates the benefit of electrokinetic DLD in sorting viable and non-viable *E. coli*. A mixture of bacteria was injected into the DLD array through five lanes close to the left wall. In the normal DLD mode (pressure driven flow, no voltage applied), at the outlet of a device having $D_C = 1.24\ \mu m$, both types of cells displayed zigzagging tendency, with non-viable cells appearing to be slightly larger and having a broader distribution. On the other hand, in a device having $D_C = 0.64\ \mu m$, also in normal DLD mode, both types of cells displayed displacing tendency, with non-viable cells appearing to be slightly larger and both types of cells having broad distributions. In both cases, separation of viable and non-viable *E. coli* at high purity was deemed to be difficult. However, if an AC voltage of 1 Hz, 138 Vpp was applied along the device having $D_C = 1.24\ \mu m$, viable and non-viable bacteria could then be separated laterally with a small overlap at the outlet. In this case, non-viable cells, interestingly, exhibited lower effective size.

4.2 Sorting Bacterial by Chain Length (Paper II)

Many bacteria are pathogenic, causing serious diseases in humans. Among them, *S. pneumoniae* is a major cause of pneumonia which leads to more than one million deaths worldwide annually, and is thus the subject of many biomedical studies. *S. pneumoniae* bacteria exist in their colonies as either single bacteria (cocci), diplococci, or chains of many cocci with varying length. It is believed that longer chains can adhere more to epithelial cells in the lung while shorter chains and single cocci are able to evade the immune system[134,135]. It is therefore of strong interest to sort these different morphologies of *S. pneumoniae* for further microbiological studies.

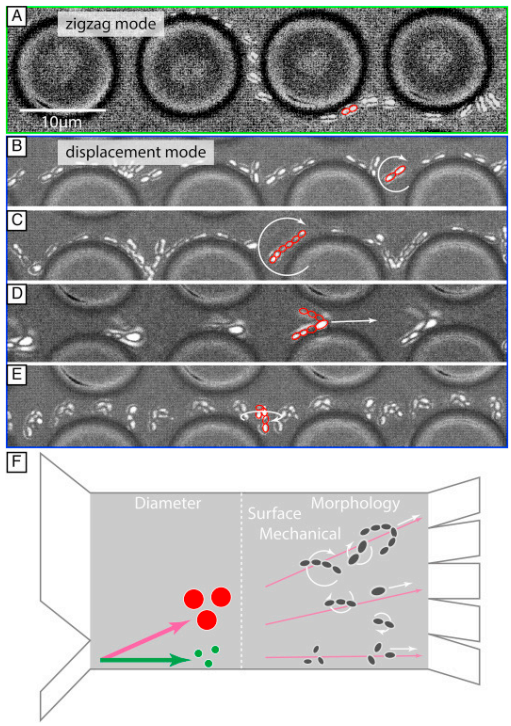

Figure 4.2: Sorting of *S. pneumonia* based on chain length. A)-E) Different trajectories of *S. pneumoniae* bacteria in a DLD device. F) Summary of the position a *S. pneumoniae* morphology can appear at the outlet, as a result of its width, length, and shape. Image taken from [109] (https://doi.org/10.1016/j.aca.2017.11.050, Creative Commons Attribution License (CC BY).

Different hydrodynamic behavior of long and short chains of *S. pneumoniae* in a DLD device, besides size, can be exploited for separation. It has been observed previously that in DLD a non-spherical particle would rotate to minimise its hydrodynamic resistance

and the smallest dimension would decide the particle's trajectory (*i.e.* zigzag or displacement)[76,97]. This is the case for the zigzagging thin diplococci exemplified in Figure 4.2A. However, when the length of the bacterial chains increase, the effective sizes of the chains are no longer their smallest dimension, due to their dynamical motions. For example, in Figure 4.2B and Figure 4.2C, the difference of fluid velocity between the two ends of a chain induces a flipping motion and leads to a displacement trajectory. In Figure 4.2D and Figure 4.2E, the chain became bent and appeared much larger than its width and as a result, travel in the displacement trajectory. In conclusion, the position of a single cocci or a chain at the outlet is dependent on its width, length, and shape (*i.e.* straight or bent chain) (Figure 4.2F).

In Paper II, with a device having the critical diameter approximately the size of a single coccus, we were able to enrich single cocci in the outlets corresponding to small effective sizes and long chains in the outlets corresponding to large effective sizes, for two different strains of *S. pneumoniae*: R6 (non-encapsulated) and D39 (encapsulated). During the experiments, we also managed to separate the two strains from each other. The separation might be contributed by their difference in size (width and chain length) or their surface property (R6 was found to be much more hydrophobic than D39).

Paper II proves that separation of different morphologies of *S. pneumoniae* is feasible with DLD. The next step is to scale up the number of bacteria sorted. A high throughput device is desirable due to two main reasons. First of all, to study a population of single cocci or a population of chains using RNA extraction and analysis, a large quantity of bacteria needs to be sorted, which is around 1-10 million colony-forming unit (CFU), within a time scale shorter than the bacteria's doubling time, which is around 20-30 minutes. This is far beyond the capability of the device presented in Paper II. Second of all, due to the inherent overlapping between the size distribution of singles and diplos and betweet chains and diplos, to obtain sufficiently pure population of single cocci, the critical diameter needs to be sufficiently small so that most of, if not all, diplo cocci are filtered out. Similar argument applies to sorting chains, but in this case the critical diameter should be large enough to remove diplo cocci from longer chains. This requirement on purity further reduces the quantity of bacteria can be collected after sorting. Inspired by the benefits a high throughput DLD device can bring, we have designed and fabricated such a device and tested it with polystyrene beads (Figure 4.3). The device was able to enrich 1.1 μm beads at high purity from a mixture of 1.1 μm and 2.1 μm beads (Figure 4.3c). The volumetric throughput

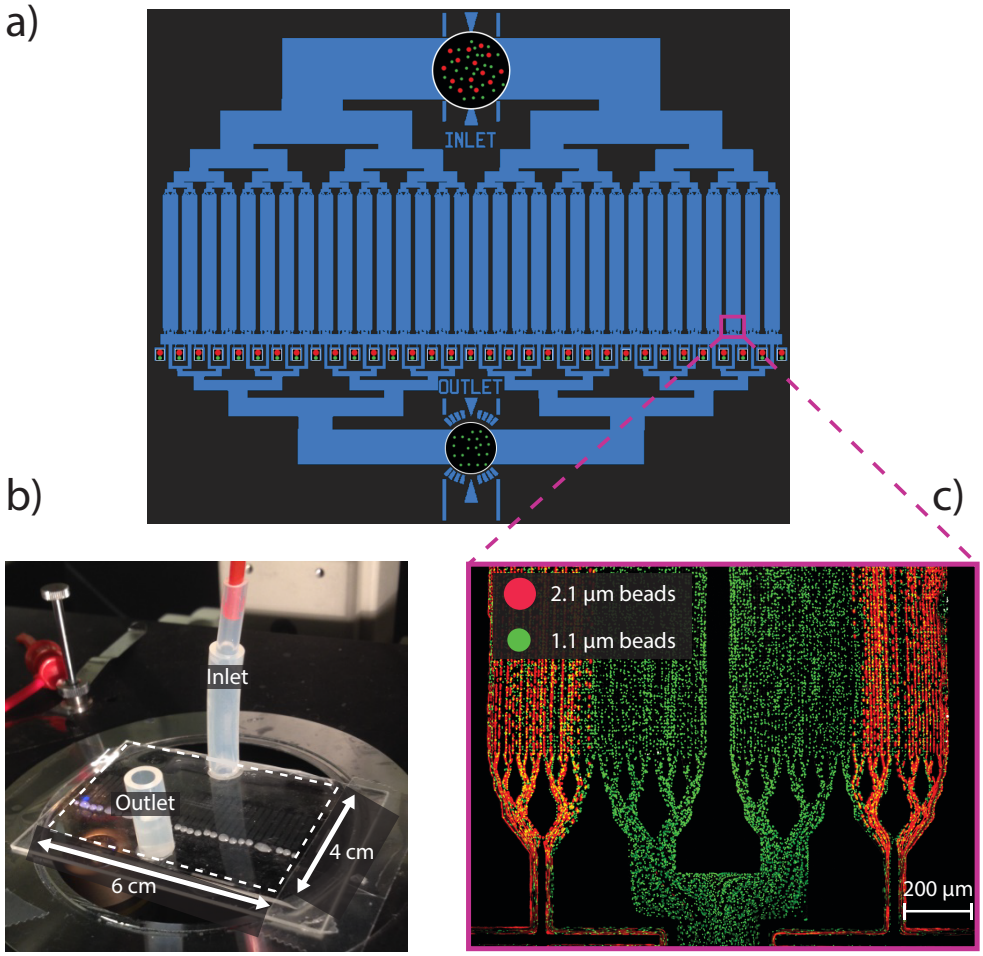

Figure 4.3: A high throughput DLD device intended for enrichment of single cocci. a) Design of device. The device has only one inlet reservoir and one outlet reservoir, with its sole purpose to enrich around half of all small particles in the mixture from the inlet reservoir into the outlet reservoir. There are 64 DLD arrays placed in parallel to increase the throughput. b) Actual image of the device. c) 1.1 μm beads were successfully enriched from the mixture into the outlet reservoir.

when running at 200 *mBar* over pressure was $43 mL/minute$ and the quantitative throughput into the outlet reservoir is roughly 25000 $beads/second$. This means to obtain a million beads, the running time is only 40 seconds, which is a promisingly short running time, with regards to the bacteria doubling time of around $20 - 30$ *minutes*.

4.3 Electrokinetic Deterministic Lateral Displacement on an Open Channel Device (paper III)

Conventional DLD devices, and microfluidic devices in general, employ pressure pumps or syringe pumps to drive fluid through an enclosed channel. While this configuration provides stable and well-controlled fluid flow, in some cases, an open channel DLD device is preferable. In such device, one of the walls (*i.e.* the lid) is removed and the pillars and the fluid are open to the environment. This new configuration offers two main advantages: simplicity, since lid bonding and fluid pumping are avoided, and reusability, since the DLD channel can be washed and stored for reuse. When open DLD is combined with electrokinetics, an additional benefit emerges: adjustability of electrodes.

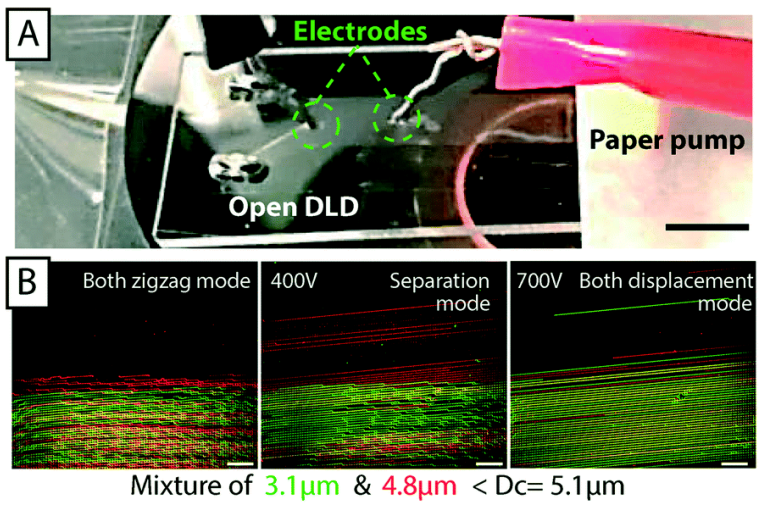

Figure 4.4: Combination of electrokinetics and open DLD. A) Setup of an electrokinetic open DLD where electrodes are placed directly on the pillar array surface. (Scale bar: $3\,mm$.) B) By tuning the voltage, $3.1\,\mu m$ and $4.8\,\mu m$ beads can be either separated or both displaced in a open DLD device with $D_C = 5.1\,\mu m$ (Scale bar: $100\,\mu m$). Image taken from [106], Published by The Royal Society of Chemistry.

The combination of electrokinetics and closed-channel DLD requires the electrodes to be embedded in the reservoirs (Beech *et. al* [107], paper I) and so, the distance between electrodes is fixed. In paper III, we tested the idea of placing electrodes directly on the surface of an open DLD device and as a result, were able to reduce the distance between electrodes from 30 mm down to 3 mm (Figure 4.4A). The placement of the electrodes on top of the array did not disturb the fluid flow and the separation of 3.1 μm and 4.8 μm beads in an open DLD device with $D_C = 5.1\,\mu m$ was demonstrated (Figure 4.4B).

4.4 Electrokinetic Rotation of Red Blood Cells in Deterministic Lateral Displacement (paper IV)

It has been proven that by controlling the depth of a DLD device, the orientation of red blood cells and thus their effective size can be changed. This effect was exploited to separate RBC from trypanosomes[97,98], the parasites which cause the *sleeping sickness* disease. Nevertheless, it is of interest to explore other methods which can also alter the orientation of red blood cells, as an alternative to fabricating DLD devices with the specific depth.

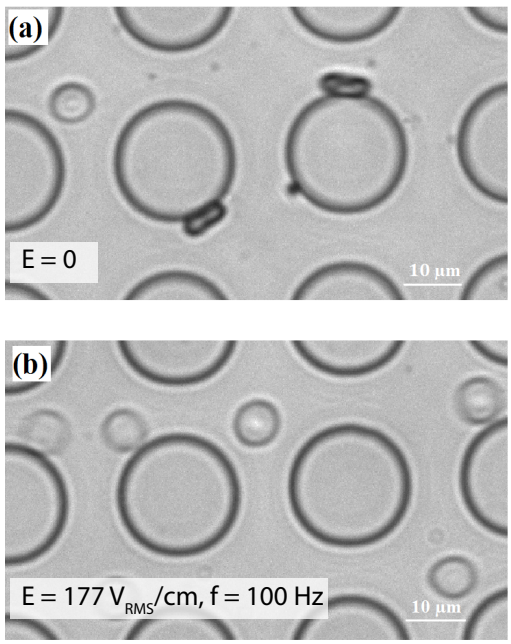

Figure 4.5: Effect of electric field on orientation of RBCs in a DLD device. a) In the absence of an electric field, when the cells travelled close to the pillars, they will lean against the pillars with their width, exhibiting a small effective size. b) When the field was on, the cells aligned horizontally like a disc, exhibiting larger effective size.

In paper IV, it was demonstrated that by applying a low frequency AC voltage (100 Hz) of a nominal value of around 177 V_{RMS}/cm, the orientation of red blood cells in deterministic lateral displacement (DLD) devices could be altered (Figure 4.5). Experiments showed that, due to this orientation change, the effective size of RBC can be increased by a factor of around 1.5, from below 3.47μm to 4.44 μm. In a future work, *Trypanosoma cyclops.* parasites can be tested in the same device and their displacement, as a function of voltage, can be compared with that of RBCs. If the difference in the effective

critical diameter of the RBCs and the parasites can be increased, then they can conceivably be separated by applying an AC voltage in DLD, as an alternative to fabricating DLD devices with specific depth. This would open up for deeper devices and therefore higher throughput.

4.5 Electrokinetic Deterministic Lateral Displacement with Metal-coated Pillar Array (paper V)

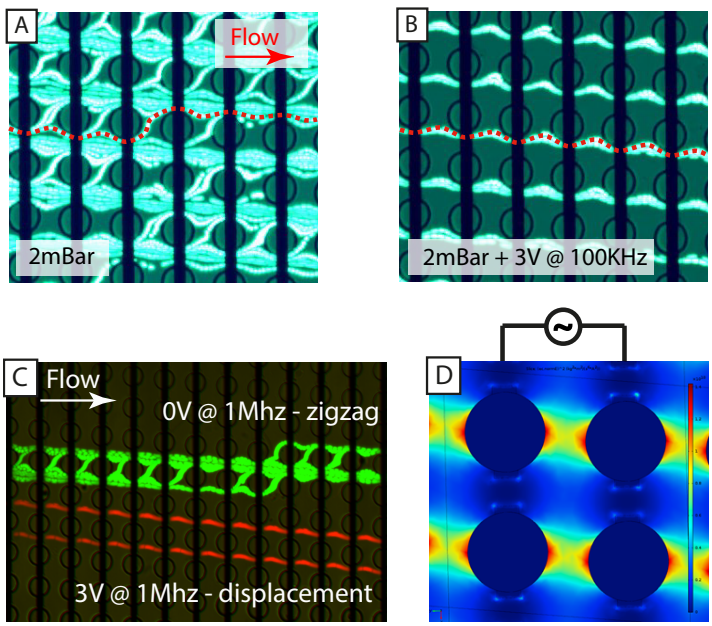

Figure 4.6: Trajectories of 2 μm carboxylate modified polystyrene particles in a metal DLD device having $D_C = 5.2\ \mu m$. A) The particles went zigzagging when no voltage was applied. B) The particles went displacing when a 3 V_{PP}, 100 kHz voltage was applied. C) Comparison of the trajectories of the same type of bead, with and without an applied voltage of 3 V_{PP}, 1 MHz. D) Numerical simulation of $|\mathbf{E}|^2$ in the metal-coated DLD array. Since the polystyrene beads experienced nDEP in our experimental conditions, they were repelled from the high field regions (red/yellow) and attracted to the low field regions (dark blue). If the flow is weak or the applied electric field is high, the beads will be trapped at the dark blue regions. Tweaking the flow and the applied field can result in particle being released from trapping, travelling with the flow but never crossing the red/yellow regions. Therefore, they will travel in displacing trajectories, following the orientation of the pillar array,

In Paper V, DLD devices with electrically connected metal-coated pillars were fabricated. Using this approach, a high field could be generated with a much smaller voltage than using macro electrodes embedded in reservoirs. By changing the applied voltage, tunable particle separations were achieved. At a voltage as low as 3 *Vpp*, it was possible to displace 2 μm polystyrene beads in a DLD device with a critical diameter of 5.2 μm, showing a large

dynamical range (Figure 4.6). Interestingly, by ramping up the voltage, separation of submicron polystyrene beads was achieved. This opens up the opportunity to sort bioparticles, for example viruses and exosomes, that are in the submicron range. The ability to displace exosomes with DLD has been demonstrated by Wunsch *et al.*[78] using a nano-DLD device, with a rather complicated fabrication process and low volumetric throughput.

4.6 Sorting of Adipocytes according to Size (project in progress)

Adipocytes (a.k.a. lipocytes or fat cells) are specialised cells making up the adipose tissue – the energy storage of humans and animals. The size of mature adipocytes vary significantly, $\sim 20\ \mu m - 200\ \mu m$ in diameter. Enlarged adipocytes are linked to insulin resistance and can be used to predict type 2 diabetes. Since the cells have lower mass density than water, to sort out different population of cells according to size, researchers allow the cells to float through nylon filters with appropriate pore size[26,27]. Although the method is practical and simple to perform, collecting of cells smaller than 50 μm is difficult since a large fraction of the smallest cells are lost in the process.

A setup has been built to fractionate adipocytes based on size using a DLD device[1]. It was demonstrated that by using a device[2] with $Gap = 50\ \mu m$, $Period = 14$, adipocytes larger and smaller than the critical diameter, $D_C = 20\ \mu m$, could be sorted (Figure 4.7). Near the outlet, most of the adipocytes, which were larger than 20 μm, were displaced toward the right wall, while a few cells which were smaller than 20 μm traveled in zigzag mode and stayed close to the left wall. In future work, a device with larger gap and as a result, larger critical diameter, can be used to fractionate the adipocytes into two separate populations of larger and smaller than 50 μm. In this way we can study the effects of adipocyte size on insulin resistance.

[1] In collaboration with Dr. Karin Stenkula, Faculty of Medicine, Lund University.

[2] The original master was designed and fabricated by Dr. Miguel Xavier, with help from Dr. Stefan Holm and Dr. Jason Beech.

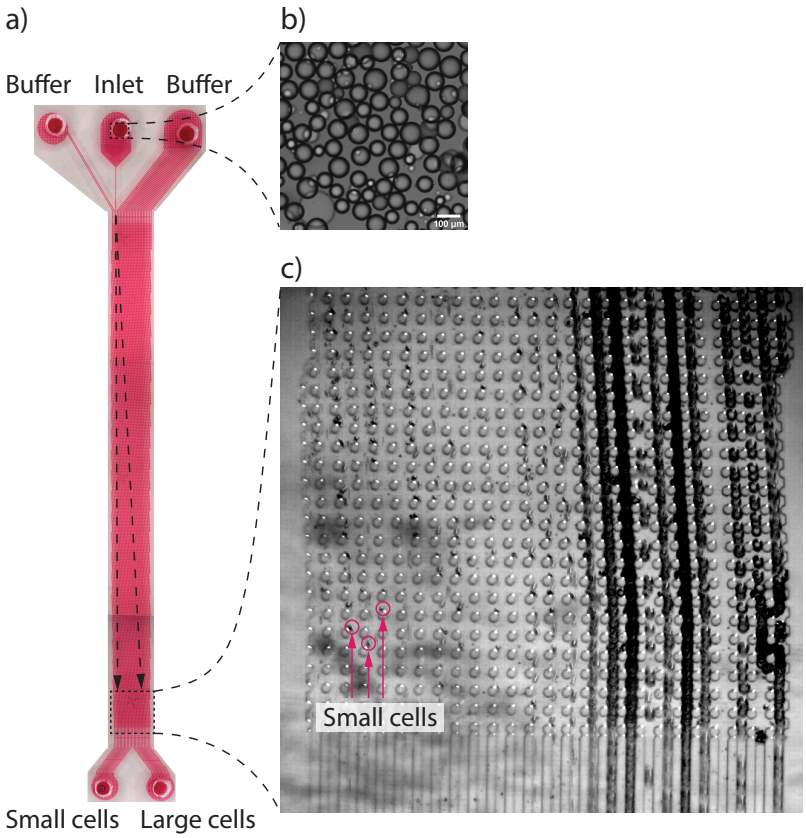

Figure 4.7: Sorting adipocytes by size using DLD. a) The device used to sort adipocytes has a gap width of 50 μm and a critical diameter of 20 μm. b) The adipocytes have a wide size distribution, ranging from below 20 μm to over 100 μm in the sample at the inlet. c) Near the outlet, most of the cells, which have a diameter of larger than 20 μm were displaced toward the right wall of the device while some of the cells which are smaller than 20 μm traveled in zigzag mode and stayed closer to the left wall. The image is a "minimum projection" of 853 frames taken at the outlet, 33 ms apart.

4.7 Conclusions and Outlooks

There is no "one-size-fit-all" approach in particle sorting. First of all, the parameters for sorting, which will decide the suitable methods, will be dependent on the intrinsic properties of the particles of interest. For example, while size can be an apparent criterion for sorting spherical cells, this parameter is somewhat ambiguous for *S. pneumoniae* (Paper II) since different morphologies of the bacteria have similar widths but different lengths. In other cases, for example viable/non-viable *E. coli* (Paper I), sorting by size is practically impossible and other properties must be exploited. Second of all, even when the same type of input samples and sorting parameters are given, different approaches can be used and each approach has its own advantages and disadvantages. An example could be sorting cells by their electrical/dielectric properties. While the metal DLD (Paper V) can offer a very high dynamical range to easily sort sub-micron particles, the fabrication is rather expensive and complicated. Insulating pillar electrokinetic DLD (Paper I) relaxes the need of metal layer deposition and etching, but requires a high voltage, and thus, an amplifier to operate. Electrokinetic open DLD (Paper III) requires simpler setup and offers reusability, but efforts should be made to stabilise the setups and the open device is prone to evaporation. In conclusion, the choice of the sorting methods should be considered based on both factors: the properties of the cells and bioparticles and the availability of sorting devices or equipment at the field.

Although my focus has been on applications (chain length sorting in Paper II and adipocyte sorting), the work described in this thesis concerns more the technical aspects of sorting techniques and efforts have been made to fractionate particles based on electrical/dielectric properties and morphologies. A future direction for this work could be applying the methods developed to sorting problems identified by researchers and professionals within the biomedical field. The adipocyte sorting project, which stemmed from discussions with diabetes researchers, is an example. In addition, there is room for improvement and development of the investigated techniques. For example, the device used to sort *S. pneumoniae* in Paper II has been enlarged and put in parallel to increase the throughput. Pilot experiments have been performed on the device with polystyrene microspheres and for the next step, bacterial sample can be tested. Paper III demonstrates a proof of principle of combining electrokinetic DLD with open DLD but to make this approach applicable for biological samples, more effort is required in designing an application-oriented integ-

rated device and improving the electrode-DLD channel contact, for example an electrode which has flat surface at the end would ensure better stability for running the experiments. The experimental work in Paper IV could be expanded to sorting *Trypanosoma cyclops* from RBCs, given the rotational effect induced on them by an AC field is different. Paper V is the beginning chapter of a promising series of study on employing the metal DLD device to sort a wide range of bioparticles, especially sub-micron ones like exosomes. For the adipocyte sorting project, new devices with larger gap and critical diameter have been made, targeting size thresholds required by biomedical researchers studying diabetes.

This chapter concludes the thesis but more details of the work can be found in the appendix and the papers attached at the end.

Chapter 5

Appendix: DLD devices

This chapter provides finer details into the DLD devices used throughout this work, mainly for Paper I and Paper II. The DLD devices used in Paper III and Paper V have been described in their ESI. The DLD device used in Paper IV has been documented by Holm[133].

DLD devices used in Paper I, for beads and yeast cells

Wafer level

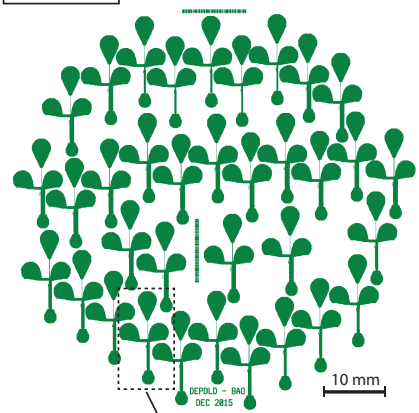

- The devices are for analytical purpose with only one single stream of inlet sample and one outlet reservoir.
- There are 33 different devices, having similar lengths and reservoir designs, but different gap widths (from 2 - 25 µm) and period (5, 10, and 20) to give a wide range of critical diameters (not all combinations were implemented). Four of them were used in Paper I.
- Device used in Paper I for polystyrene beads:

Gap width(µm)	Pillar diameter (µm)	Period	Critical diameter (µm)
6	20	10	2.8

- Devices used in Paper I for yeast cells:

Gap width (µm)	Pillar diameter (µm)	Period	Critical diameter (µm)
10	20	10	4.6
11	20	10	5.1
12	20	10	5.6

Device level

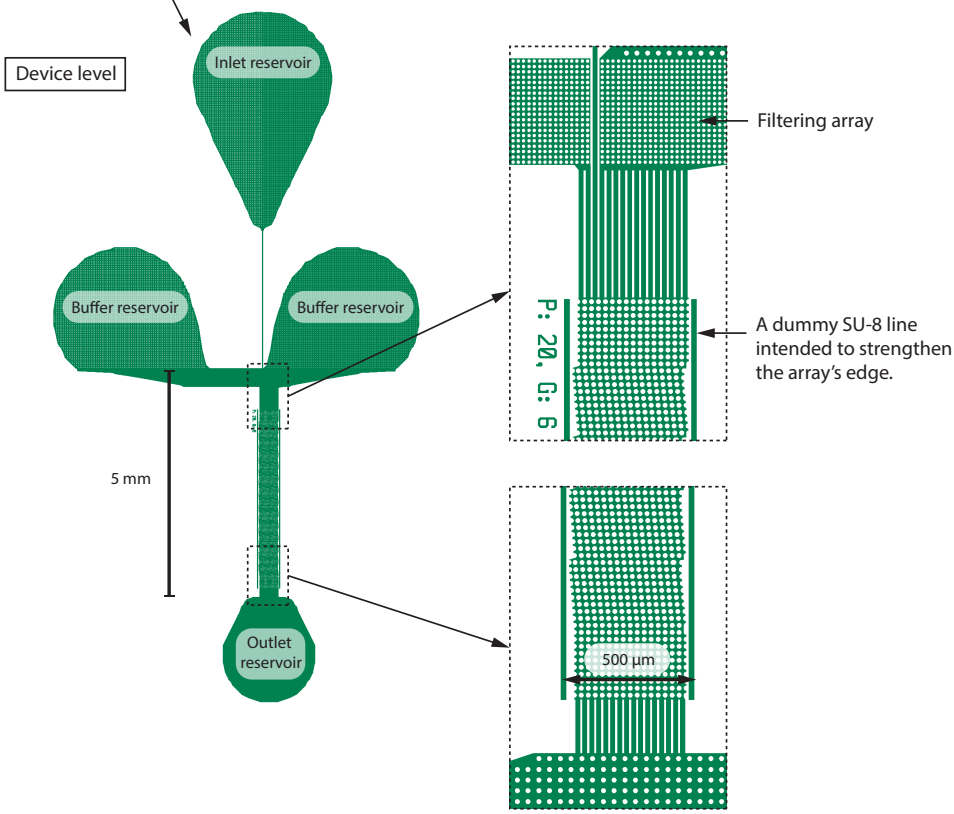

DLD devices used in Paper I and Paper II, for sorting *E. coli* and *S. pneumoniae*

Wafer level

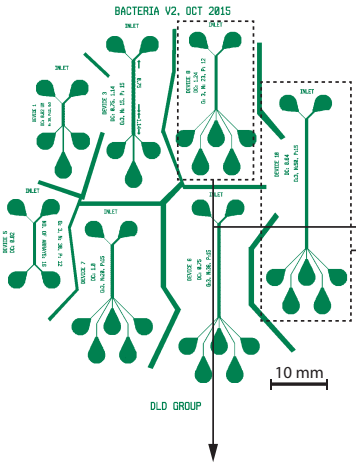

- The devices are for sorting and recovering sorted populations
- There are 7 different devices, having critical diameters varying around 1µm. Two of them were used for sorting *E. coli* and one for *S. pneumoniae.*
- Devices used in Paper I for *E. coli* :

Gap width (µm)	Pillar diameter (µm)	Period	Critical diameter (µm)
4	12	23	1.24
3	15	50	0.64

- Device used in Paper II for *S. pneumoniae* :

Gap width(µm)	Pillar diameter (µm)	Period	Critical diameter (µm)
4	12	23	1.24

Device level

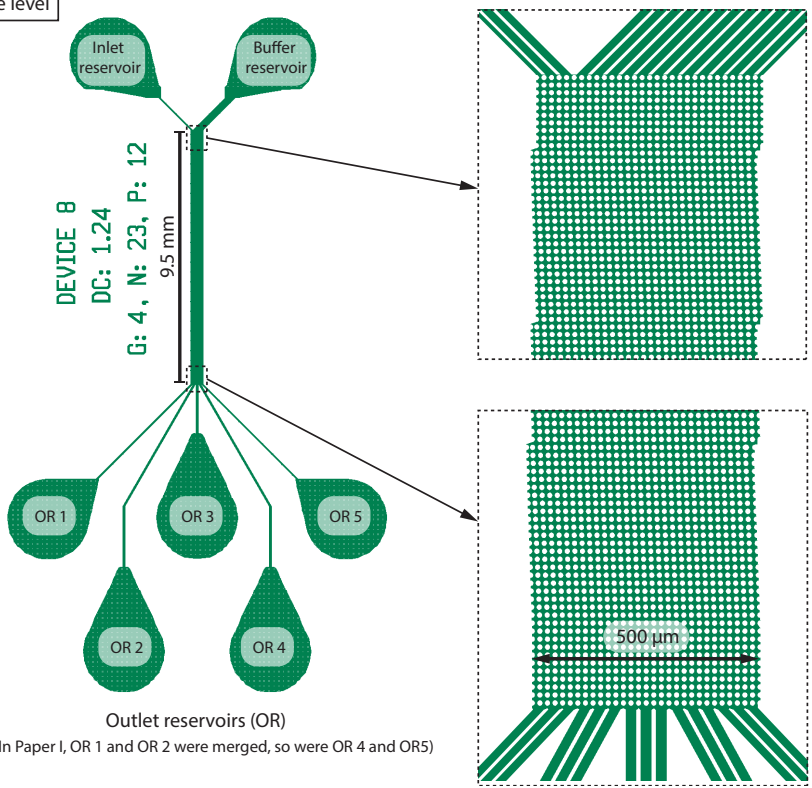

Outlet reservoirs (OR)

(In Paper I, OR 1 and OR 2 were merged, so were OR 4 and OR5)

Bibliography

[1] E. Bassous, H. H. Taub, and L. Kuhn. Ink jet printing nozzle arrays etched in silicon. *Applied Physics Letters*, 31(2):135–137, 1977.

[2] S. C. Terry, J. H. Jerman, and J. B. Angell. A gas chromatographic air analyzer fabricated on a silicon wafer. *IEEE Transactions on Electron Devices*, 26(12):1880–1886, 1979.

[3] Peter Gravesen, Jens Branebjerg, and O Søndergård Jensen. Microfluidics-a review. *Journal of Micromechanics and Microengineering*, 3(4):168, 1993.

[4] Younan Xia and George M Whitesides. Soft lithography. *Annual review of materials science*, 28(1):153–184, 1998.

[5] G. M. Whitesides. The origins and the future of microfluidics. *Nature*, 442(7101):368–73, 2006.

[6] E. K. Sackmann, A. L. Fulton, and D. J. Beebe. The present and future role of microfluidics in biomedical research. *Nature*, 507(7491):181–9, 2014.

[7] Curtis D Chin, Vincent Linder, and Samuel K Sia. Commercialization of microfluidic point-of-care diagnostic devices. *Lab on a Chip*, 12(12):2118–2134, 2012.

[8] Ali Kemal Yetisen, Muhammad Safwan Akram, and Christopher R Lowe. Paper-based microfluidic point-of-care diagnostic devices. *Lab on a Chip*, 13(12):2210–2251, 2013.

[9] Frank B Myers and Luke P Lee. Innovations in optical microfluidic technologies for point-of-care diagnostics. *Lab on a Chip*, 8(12):2015–2031, 2008.

[10] Derek Tseng, Onur Mudanyali, Cetin Oztoprak, Serhan O Isikman, Ikbal Sencan, Oguzhan Yaglidere, and Aydogan Ozcan. Lensfree microscopy on a cellphone. *Lab on a Chip*, 10(14):1787–1792, 2010.

[11] Shia-Yen Teh, Robert Lin, Lung-Hsin Hung, and Abraham P Lee. Droplet microfluidics. *Lab on a Chip*, 8(2):198–220, 2008.

[12] Samaneh Mashaghi, Alireza Abbaspourrad, David A Weitz, and Antoine M van Oijen. Droplet microfluidics: A tool for biology, chemistry and nanotechnology. *TrAC Trends in Analytical Chemistry*, 82:118–125, 2016.

[13] Pooria Mostafalu, Mohsen Akbari, Kyle A. Alberti, Qiaobing Xu, Ali Khademhosseini, and Sameer R. Sonkusale. A toolkit of thread-based microfluidics, sensors, and electronics for 3d tissue embedding for medical diagnostics. *Microsystems &Amp; Nanoengineering*, 2:16039, 2016.

[14] Zhihong Nie, Christian A Nijhuis, Jinlong Gong, Xin Chen, Alexander Kumachev, Andres W Martinez, Max Narovlyansky, and George M Whitesides. Electrochemical sensing in paper-based microfluidic devices. *Lab on a Chip*, 10(4):477–483, 2010.

[15] Yifan Liu, Lilian M Schweizer, Wenxing Wang, Robert L Reuben, Michael Schweizer, and Wenmiao Shu. Label-free and real-time monitoring of yeast cell growth by the bending of polymer microcantilever biosensors. *Sensors and Actuators B: Chemical*, 178:621–626, 2013.

[16] Georgette B. Salieb-Beugelaar, Giuseppina Simone, Arun Arora, Anja Philippi, and Andreas Manz. Latest developments in microfluidic cell biology and analysis systems. *Analytical Chemistry*, 82(12):4848–4864, 2010.

[17] Matthias Mehling and Savaş Tay. Microfluidic cell culture. *Current Opinion in Biotechnology*, 25:95–102, 2014.

[18] S Elizabeth Hulme, Sergey S Shevkoplyas, Javier Apfeld, Walter Fontana, and George M Whitesides. A microfabricated array of clamps for immobilizing and imaging c. elegans. *Lab on a Chip*, 7(11):1515–1523, 2007.

[19] Kwanghun Chung, Matthew M Crane, and Hang Lu. Automated on-chip rapid microscopy, phenotyping and sorting of c. elegans. *Nature methods*, 5(7):637, 2008.

[20] Trushal Vijaykumar Chokshi, Adela Ben-Yakar, and Nikos Chronis. Co 2 and compressive immobilization of c. elegans on-chip. *Lab on a Chip*, 9(1):151–157, 2009.

[21] Jan Krajniak and Hang Lu. Long-term high-resolution imaging and culture of c. elegans in chip-gel hybrid microfluidic device for developmental studies. *Lab on a Chip*, 10(14):1862–1868, 2010.

[22] Dongeun Huh, Yu-suke Torisawa, Geraldine A Hamilton, Hyun Jung Kim, and Donald E Ingber. Microengineered physiological biomimicry: organs-on-chips. *Lab on a Chip*, 12(12):2156–2164, 2012.

[23] Yosuke Nakao, Hiroshi Kimura, Yasuyuki Sakai, and Teruo Fujii. Bile canaliculi formation by aligning rat primary hepatocytes in a microfluidic device. *Biomicrofluidics*, 5(2):022212, 2011.

[24] Kyung-Jin Jang and Kahp-Yang Suh. A multi-layer microfluidic device for efficient culture and analysis of renal tubular cells. *Lab on a Chip*, 10(1):36–42, 2010.

[25] Dongeun Huh, Benjamin D Matthews, Akiko Mammoto, Martín Montoya-Zavala, Hong Yuan Hsin, and Donald E Ingber. Reconstituting organ-level lung functions on a chip. *Science*, 328(5986):1662–1668, 2010.

[26] Margareta Jernås, Jenny Palming, Kajsa Sjöholm, Eva Jennische, Per-Arne Svensson, Britt G. Gabrielsson, Max Levin, Anders Sjögren, Mats Rudemo, Theodore C. Lystig, Björn Carlsson, Lena M. S. Carlsson, and Malin Lönn. Separation of human adipocytes by size: hypertrophic fat cells display distinct gene expression. *The FASEB Journal*, 20(9):1540–1542, 2006.

[27] N. Franck, K. G. Stenkula, A. Öst, T. Lindström, P. Strålfors, and F. H. Nystrom. Insulin-induced glut4 translocation to the plasma membrane is blunted in large compared with small primary fat cells isolated from the same individual. *Diabetologia*, 50(8):1716–1722, 2007.

[28] Andreas Lenshof, Arshad Jamal, Josefina Dykes, Anke Urbansky, Ingbritt Åstrand Grundström, Thomas Laurell, and Stefan Scheding. Efficient purification of cd4+ lymphocytes from peripheral blood progenitor cell products using affinity bead acoustophoresis. *Cytometry Part A*, 85(11):933–941, 2014.

[29] D. R. Gossett, W. M. Weaver, A. J. Mach, S. C. Hur, H. T. Tse, W. Lee, H. Amini, and D. Di Carlo. Label-free cell separation and sorting in microfluidic systems. *Anal Bioanal Chem*, 397(8):3249–67, 2010.

[30] Andreas Lenshof and Thomas Laurell. Continuous separation of cells and particles in microfluidic systems. *Chemical Society Reviews*, 39(3):1203–1217, 2010.

[31] Edwin Mellor Southern. Detection of specific sequences among dna fragments separated by gel electrophoresis. *J mol biol*, 98(3):503–517, 1975.

[32] D Jed Harrison, Karl Fluri, Kurt Seiler, Zhonghui Fan, Carlo S Effenhauser, and Andreas Manz. Micromachining a miniaturized capillary electrophoresis-based chemical analysis system on a chip. *Science*, 261(5123):895–897, 1993.

[33] R. Pethig. Review article-dielectrophoresis: status of the theory, technology, and applications. *Biomicrofluidics*, 4(2), 2010.

[34] Michael P Hughes. Strategies for dielectrophoretic separation in laboratory-on-a-chip systems. *Electrophoresis*, 23(16):2569–2582, 2002.

[35] Filip Petersson, Lena Åberg, Ann-Margret Swärd-Nilsson, and Thomas Laurell. Free flow acoustophoresis: microfluidic-based mode of particle and cell separation. *Analytical chemistry*, 79(14):5117–5123, 2007.

[36] J Calvin Giddings. A new separation concept based on a coupling of concentration and flow nonuniformities. *Separation Science*, 1(1):123–125, 1966.

[37] Masumi Yamada, Megumi Nakashima, and Minoru Seki. Pinched flow fractionation: continuous size separation of particles utilizing a laminar flow profile in a pinched microchannel. *Analytical chemistry*, 76(18):5465–5471, 2004.

[38] L. R. Huang, E. C. Cox, R. H. Austin, and J. C. Sturm. Continuous particle separation through deterministic lateral displacement. *Science*, 304(5673):987–90, 2004.

[39] Dino Di Carlo. Inertial microfluidics. *Lab on a Chip*, 9(21):3038–3046, 2009.

[40] George Keith Batchelor. *An introduction to fluid dynamics*. Cambridge university press, 2000.

[41] G. Hauke. *An Introduction to Fluid Mechanics and Transport Phenomena*. Springer Netherlands, 2010.

[42] B. Lautrup. *Physics of Continuous Matter, Second Edition: Exotic and Everyday Phenomena in the Macroscopic World*. Taylor & Francis, 2011.

[43] Nam-Trung Nguyen, Steven T Wereley, and Steven T Wereley. *Fundamentals and applications of microfluidics*. Artech house, 2002.

[44] H. Bruus. *Theoretical Microfluidics*. OUP Oxford, 2008.

[45] Charles L Fefferman. Existence and smoothness of the navier-stokes equation. *The millennium prize problems*, 57:67, 2006.

[46] Bruno Eckhardt. Introduction. turbulence transition in pipe flow: 125th anniversary of the publication of reynolds' paper. *Philosophical Transactions of the Royal Society A: Mathematical, Physical and Engineering Sciences*, 367(1888):449–455, 2009.

[47] D. W. Inglis, J. A. Davis, R. H. Austin, and J. C. Sturm. Critical particle size for fractionation by deterministic lateral displacement. *Lab Chip*, 6(5):655–8, 2006.

[48] Jason Beech. *Microfluidics Separation and Analysis of Biological Particles*. PhD Thesis. Lund University, 2011.

[49] J. A. Davis. *Microfluidic Separation of Blood Components through Deterministic Lateral Displacement*, volume Doctors of *Electrical Engineering*. PhD Thesis. Princeton University, 2008.

[50] Kevin Loutherback, Jason Puchalla, Robert H Austin, and James C Sturm. Deterministic microfluidic ratchet. *Physical review letters*, 102(4):045301, 2009.

[51] M. Balvin, E. Sohn, T. Iracki, G. Drazer, and J. Frechette. Directional locking and the role of irreversible interactions in deterministic hydrodynamics separations in microfluidic devices. *Phys Rev Lett*, 103(7):078301, 2009.

[52] Joelle Frechette and German Drazer. Directional locking and deterministic separation in periodic arrays. *Journal of Fluid Mechanics*, 627:379–401, 2009.

[53] John Herrmann, Michael Karweit, and German Drazer. Separation of suspended particles in microfluidic systems by directional locking in periodic fields. *Physical Review E*, 79(6):061404, 2009.

[54] T. Bowman, J. Frechette, and G. Drazer. Force driven separation of drops by deterministic lateral displacement. *Lab on a Chip*, 12(16):2903–2908, 2012.

[55] R. Devendra and G. Drazer. Gravity driven deterministic lateral displacement for particle separation in microfluidic devices. *Analytical Chemistry*, 84(24):10621–10627, 2012.

[56] T. J. Bowman, G. Drazer, and J. Frechette. Inertia and scaling in deterministic lateral displacement. *Biomicrofluidics*, 7(6), 2013.

[57] S. R. Risbud and G. Drazer. Directional locking in deterministic lateral-displacement microfluidic separation systems. *Phys Rev E Stat Nonlin Soft Matter Phys*, 90(1):012302, 2014.

[58] S. Hanasoge, R. Devendra, F. J. Diez, and G. Drazer. Electrokinetically driven deterministic lateral displacement for particle separation in microfluidic devices. *Microfluidics and Nanofluidics*, 18(5-6):1195–1200, 2015.

[59] M. L. Jiang, K. Budzan, and G. Drazer. Fractionation by shape in deterministic lateral displacement microfluidic devices. *Microfluidics and Nanofluidics*, 19(2):427–434, 2015.

[60] M. L. Jiang, A. D. Mazzeo, and G. Drazer. Centrifuge-based deterministic lateral displacement separation. *Microfluidics and Nanofluidics*, 20(1), 2016.

[61] S. Q. Du and G. Drazer. Gravity driven deterministic lateral displacement for suspended particles in a 3d obstacle array. *Scientific Reports*, 6, 2016.

[62] S Cerbelli. Separation of polydisperse particle mixtures by deterministic lateral displacement. the impact of particle diffusivity on separation efficiency. *Asia-Pacific Journal of Chemical Engineering*, 7(S3), 2012.

[63] Gaetano D'Avino. Non-newtonian deterministic lateral displacement separator: theory and simulations. *Rheologica Acta*, 52(3):221–236, 2013.

[64] F. Khodaee, S. Movahed, N. Fatouraee, and F. Daneshmand. Numerical simulation of separation of circulating tumor cells from blood stream in deterministic lateral displacement (DLD) microfluidic channel. *Journal of Mechanics*, 32(4):463–471, 2016.

[65] M. Heller and H. Bruus. A theoretical analysis of the resolution due to diffusion and size dispersion of particles in deterministic lateral displacement devices. *Journal of Micromechanics and Microengineering*, 18(7), 2008.

[66] B. R. Long, M. Heller, J. P. Beech, H. Linke, H. Bruus, and J. O. Tegenfeldt. Multidirectional sorting modes in deterministic lateral displacement devices. *Physical Review E*, 78(4), 2008.

[67] S. Cerbelli, M. Giona, and F. Garofalo. Quantifying dispersion of finite-sized particles in deterministic lateral displacement microflow separators through brenner's macrotransport paradigm. *Microfluidics and Nanofluidics*, 15(4):431–449, 2013.

[68] Stefano Cerbelli, Fabio Garofalo, and Massimiliano Giona. Effective dispersion and separation resolution in continuous particle fractionation. *Microfluidics and Nanofluidics*, 19(5):1035–1046, 2015.

[69] Junchao Wang, Victor GJ Rodgers, Philip Brisk, and William H Grover. Mopsa: A microfluidics-optimized particle simulation algorithm. *Biomicrofluidics*, 11(3):034121, 2017.

[70] Timm Krüger, David Holmes, and Peter V Coveney. Deformability-based red blood cell separation in deterministic lateral displacement devices—a simulation study. *Biomicrofluidics*, 8(5):054114, 2014.

[71] Rohan Vernekar and Timm Krüger. Breakdown of deterministic lateral displacement efficiency for non-dilute suspensions: A numerical study. *Medical Engineering and Physics*, 37(9):845–854, 2015.

[72] Jianhui Wei, Hui Song, Zaiyi Shen, Ying He, Xianzhi Xu, Yong Zhang, and Bing Nan Li. Numerical study of pillar shapes in deterministic lateral displacement microfluidic arrays for spherical particle separation. *IEEE transactions on nanobioscience*, 14(6):660–667, 2015.

[73] Q. Wei, Y. Q. Xu, X. Y. Tang, and F. B. Tian. An ib-lbm study of continuous cell sorting in deterministic lateral displacement arrays. *Acta Mechanica Sinica*, 32(6):1023–1030, 2016.

[74] Raymond Quek, Duc Vinh Le, and K-H Chiam. Separation of deformable particles in deterministic lateral displacement devices. *Physical Review E*, 83(5):056301, 2011.

[75] Shangjun Ye, Xueming Shao, Zhaosheng Yu, and Wenguang Yu. Effects of the particle deformability on the critical separation diameter in the deterministic lateral displacement device. *Journal of Fluid Mechanics*, 743:60–74, 2014.

[76] E. Henry, S. H. Holm, Z. M. Zhang, J. P. Beech, J. O. Tegenfeldt, D. A. Fedosov, and G. Gompper. Sorting cells by their dynamical properties. *Scientific Reports*, 6, 2016.

[77] J. A. Davis, D. W. Inglis, K. J. Morton, D. A. Lawrence, L. R. Huang, S. Y. Chou, J. C. Sturm, and R. H. Austin. Deterministic hydrodynamics: taking blood apart. *Proc Natl Acad Sci U S A*, 103(40):14779–84, 2006.

[78] B. H. Wunsch, J. T. Smith, S. M. Gifford, C. Wang, M. Brink, R. L. Bruce, R. H. Austin, G. Stolovitzky, and Y. Astier. Nanoscale lateral displacement arrays for the separation of exosomes and colloids down to 20 nm. *Nature Nanotechnology*, 11(11):936–940, 2016.

[79] S. Y. Zheng, Y. C. Tai, and H. Kasdan. A micro device for separation of erythrocytes and leukocytes in human blood. *2005 27th Annual International Conference of the IEEE Engineering in Medicine and Biology Society, Vols 1-7*, pages 1024–1027, 2005.

[80] J. P. Beech and J. O. Tegenfeldt. Tuneable separation in elastomeric microfluidics devices. *Lab Chip*, 8(5):657–9, 2008.

[81] David W Inglis, Megan Lord, and Robert E Nordon. Scaling deterministic lateral displacement arrays for high throughput and dilution-free enrichment of leukocytes. *Journal of Micromechanics and Microengineering*, 21(5):054024, 2011.

[82] B. Bilenberg, M. Hansen, D. Johansen, V. Ozkapici, C. Jeppesen, P. Szabo, I. M. Obieta, O. Arroyo, J. O. Tegenfeldt, and A. Kristensen. Topas-based lab-on-a-chip microsystems fabricated by thermal nanoimprint lithography. *Journal of Vacuum Science & Technology B*, 23(6):2944–2949, 2005.

[83] C. I. Civin, T. Ward, A. M. Skelley, K. Gandhi, Z. P. Lee, C. R. Dosier, J. L. D'Silva, Y. Chen, M. Kim, J. Moynihan, X. C. Chen, L. Aurich, S. Gulnik, G. C. Brittain, D. J. Recktenwald, R. H. Austin, and J. C. Sturm. Automated leukocyte processing by microfluidic deterministic lateral displacement. *Cytometry Part A*, 89A(12):1073–1083, 2016.

[84] K. Loutherback, K. S. Chou, J. Newman, J. Puchalla, R. H. Austin, and J. C. Sturm. Improved performance of deterministic lateral displacement arrays with triangular posts. *Microfluidics and Nanofluidics*, 9(6):1143–1149, 2010.

[85] K. Loutherback, J. D'Silva, L. Liu, A. Wu, R. H. Austin, and J. C. Sturm. Deterministic separation of cancer cells from blood at 10 ml/min. *AIP Adv*, 2(4):42107, 2012.

[86] Z. Liu, F. Huang, J. Du, W. Shu, H. Feng, X. Xu, and Y. Chen. Rapid isolation of cancer cells using microfluidic deterministic lateral displacement structure. *Biomicrofluidics*, 7(1):11801, 2013.

[87] Z. M. Zhang, E. Henry, G. Gompper, and D. A. Fedosova. Behavior of rigid and deformable particles in deterministic lateral displacement devices with different post shapes. *Journal of Chemical Physics*, 143(24), 2015.

[88] J. D'silva, R. H. Austin, and J. C. Sturm. Inhibition of clot formation in deterministic lateral displacement arrays for processing large volumes of blood for rare cell capture. *Lab on a Chip*, 15(10):2240–2247, 2015.

[89] Z. B. Liu, Y. Lee, J. H. Jang, Y. Li, X. Han, K. Yokoi, M. Ferrari, L. D. Zhou, and L. D. Qin. Microfluidic cytometric analysis of cancer cell transportability and invasiveness. *Scientific Reports*, 5, 2015.

[90] Zongbin Liu, Rui Chen, Ying Li, Jianqiao Liu, Ping Wang, Xuefeng Xia, and Lidong Qin. Integrated microfluidic chip for efficient isolation and deformability analysis of circulating tumor cells. *Advanced Biosystems*, 0(0):1800200, 2018.

[91] K. K. Zeming, S. Ranjan, and Y. Zhang. Rotational separation of non-spherical bioparticles using i-shaped pillar arrays in a microfluidic device. *Nature Communications*, 4, 2013.

[92] S. Ranjan, K. K. Zeming, R. Jureen, D. Fisher, and Y. Zhang. Dld pillar shape design for efficient separation of spherical and non-spherical bioparticles. *Lab on a Chip*, 14(21):4250–4262, 2014.

[93] S. H. Au, J. Edd, A. E. Stoddard, K. H. K. Wong, F. Fachin, S. Maheswaran, D. A. Haber, S. L. Stott, R. Kapur, and M. Toner. Microfluidic isolation of circulating tumor cell clusters by size and asymmetry. *Sci Rep*, 7(1):2433, 2017.

[94] Nezihi Murat Karabacak, Philipp S. Spuhler, Fabio Fachin, Eugene J. Lim, Vincent Pai, Emre Ozkumur, Joseph M. Martel, Nikola Kojic, Kyle Smith, Pin-i Chen, Jennifer Yang, Henry Hwang, Bailey Morgan, Julie Trautwein, Thomas A. Barber, Shannon L. Stott, Shyamala Maheswaran, Ravi Kapur, Daniel A. Haber, and Mehmet Toner. Microfluidic, marker-free isolation of circulating tumor cells from blood samples. *Nature Protocols*, 9:694, 2014.

[95] J. C. Hyun, J. Hyun, S. Wang, and S. Yang. Improved pillar shape for deterministic lateral displacement separation method to maintain separation efficiency over a long period of time. *Separation and Purification Technology*, 172:258–267, 2017.

[96] M. Al-Fandi, M. Al-Rousan, M. A. K. Jaradat, and L. Al-Ebbini. New design for the separation of microorganisms using microfluidic deterministic lateral displacement. *Robotics and Computer-Integrated Manufacturing*, 27(2):237–244, 2011.

[97] S. H. Holm, J. P. Beech, M. P. Barrett, and J. O. Tegenfeldt. Separation of parasites from human blood using deterministic lateral displacement. *Lab Chip*, 11(7):1326–32, 2011.

[98] S. H. Holm, J. P. Beech, M. P. Barrett, and J. O. Tegenfeldt. Simplifying microfluidic separation devices towards field-detection of blood parasites. *Anal. Methods*, 8(16):3291–3300, 2016.

[99] Rohan Vernekar, Timm Krüger, Kevin Loutherback, Keith Morton, and David W Inglis. Anisotropic permeability in deterministic lateral displacement arrays. *Lab on a Chip*, 17(19):3318–3330, 2017.

[100] David W Inglis. Efficient microfluidic particle separation arrays. *Applied Physics Letters*, 94(1):013510, 2009.

[101] T Kulrattanarak, RGM Van der Sman, YS Lubbersen, CGPH Schroën, HTM Pham, PM Sarro, and RM Boom. Mixed motion in deterministic ratchets due to anisotropic permeability. *Journal of colloid and interface science*, 354(1):7–14, 2011.

[102] T Kulrattanarak, RGM Van Der Sman, CGPH Schroën, and RM Boom. Analysis of mixed motion in deterministic ratchets via experiment and particle simulation. *Microfluidics and Nanofluidics*, 10(4):843–853, 2011.

[103] S. C. Kim, B. H. Wunsch, H. Hu, J. T. Smith, R. H. Austin, and G. Stolovitzky. Broken flow symmetry explains the dynamics of small particles in deterministic lateral displacement arrays. *Proceedings of the National Academy of Sciences of the United States of America*, 114(26):E5034–E5041, 2017.

[104] N. Tottori, T. Nisisako, J. Park, Y. Yanagida, and T. Hatsuzawa. Separation of viable and nonviable mammalian cells using a deterministic lateral displacement microfluidic device. *Biomicrofluidics*, 10(1), 2016.

[105] S. L. Feng, A. M. Skelley, A. G. Anwer, G. Z. Liu, and D. W. Inglis. Maximizing particle concentration in deterministic lateral displacement arrays (vol 11, 024121, 2017). *Biomicrofluidics*, 11(3), 2017.

[106] Trung SH Tran, Bao D Ho, Jason P Beech, and Jonas O Tegenfeldt. Open channel deterministic lateral displacement for particle and cell sorting. *Lab on a Chip*, 17(21):3592–3600, 2017.

[107] J. P. Beech, P. Jonsson, and J. O. Tegenfeldt. Tipping the balance of deterministic lateral displacement devices using dielectrophoresis. *Lab Chip*, 9(18):2698–706, 2009.

[108] J. P. Beech, S. H. Holm, K. Adolfsson, and J. O. Tegenfeldt. Sorting cells by size, shape and deformability. *Lab Chip*, 12(6):1048–51, 2012.

[109] Jason P Beech, Bao Dang Ho, Geneviève Garriss, Vitor Oliveira, Birgitta Henriques-Normark, and Jonas O Tegenfeldt. Separation of pathogenic bacteria by chain length. *Analytica chimica acta*, 1000:223–231, 2018.

[110] A. J. Laki, L. Botzheim, K. Ivan, T. Szabo, V. Tamasi, E. Buzas, and P. Civera. Microvesicle fractionation using deterministic lateral displacement effect. *2014*

9th IEEE International Conference on Nano/Micro Engineered and Molecular Systems (Nems), pages 490–493, 2014.

[111] A. J. Laki, L. Botzheim, K. Ivan, V. Tamasi, and P. Civera. Separation of microvesicles from serological samples using deterministic lateral displacement effect. *Bio Nanoscience*, 5(1):48–54, 2015.

[112] R Huang, TA Barber, MA Schmidt, RG Tompkins, M Toner, DW Bianchi, R Kapur, and WL Flejter. A microfluidics approach for the isolation of nucleated red blood cells (nrbcs) from the peripheral blood of pregnant women. *Prenatal diagnosis*, 28(10):892–899, 2008.

[113] James V. Green, Milica Radisic, and Shashi K. Murthy. Deterministic lateral displacement as a means to enrich large cells for tissue engineering. *Analytical Chemistry*, 81(21):9178–9182, 2009.

[114] D. W. Inglis, N. Herman, and G. Vesey. Highly accurate deterministic lateral displacement device and its application to purification of fungal spores. *Biomicrofluidics*, 4(2), 2010.

[115] B. Y. Zhang, J. V. Green, S. K. Murthy, and M. Radisic. Label-free enrichment of functional cardiomyocytes using microfluidic deterministic lateral flow displacement. *Plos One*, 7(5), 2012.

[116] H. N. Joensson, M. Uhlen, and H. A. Svahn. Droplet size based separation by deterministic lateral displacement-separating droplets by cell-induced shrinking. *Lab on a Chip*, 11(7):1305–1310, 2011.

[117] N. Tottori, T. Hatsuzawa, and T. Nisisako. Separation of main and satellite droplets in a deterministic lateral displacement microfluidic device. *Rsc Advances*, 7(56):35516–35524, 2017.

[118] Y. Chen, J. D'Silva, R. H. Austin, and J. C. Sturm. Microfluidic chemical processing with on-chip washing by deterministic lateral displacement arrays with separator walls. *Biomicrofluidics*, 9(5), 2015.

[119] N. Li, D. T. Kamei, and C. M. Ho. On-chip continuous blood cell subtype separation by deterministic lateral displacement. In *2007 2nd IEEE International Conference on Nano/Micro Engineered and Molecular Systems*, pages 932–936.

[120] D. Holmes, G. Whyte, J. Bailey, N. Vergara-Irigaray, A. Ekpenyong, J. Guck, and T. Duke. Separation of blood cells with differing deformability using deterministic lateral displacement. *Interface Focus*, 4(6), 2014.

[121] H. Okano, T. Konishi, T. Suzuki, T. Suzuki, S. Ariyasu, S. Aoki, R. Abe, and M. Hayase. Enrichment of circulating tumor cells in tumor-bearing mouse blood by a deterministic lateral displacement microfluidic device. *Biomedical Microdevices*, 17(3), 2015.

[122] H. Morgan and N.G. Green. *AC Electrokinetics: Colloids and Nanoparticles*. Research Studies Press, 2003.

[123] JO'M Bockris, MAV Devanathan, and K Müller. *On the structure of charged interfaces*, pages 832–863. Elsevier, 1965.

[124] J.O.M. Bockris, A.K.N. Reddy, and M.E. Gamboa-Aldeco. *Modern Electrochemistry 2A: Fundamentals of Electrodics*. Springer US, 2007.

[125] W.B. Russel, W.B. Russel, D.A. Saville, and W.R. Schowalter. *Colloidal Dispersions*. Cambridge University Press, 1991.

[126] FF Reuss. Charge-induced flow. In *Proceedings of the Imperial Society of Naturalists of Moscow*, volume 3, pages 327–344.

[127] Jean-Louis Viovy. Electrophoresis of dna and other polyelectrolytes: Physical mechanisms. *Reviews of Modern Physics*, 72(3):813–872, 2000.

[128] David Erickson. *Electroosmotic Flow (DC)*, pages 560–567. Springer US, Boston, MA, 2008.

[129] Brian J Kirby and Ernest F Hasselbrink Jr. Zeta potential of microfluidic substrates: 2. data for polymers. *Electrophoresis*, 25(2):203–213, 2004.

[130] R.R. Pethig. *Dielectrophoresis: Theory, Methodology and Biological Applications*. Wiley, 2017.

[131] Thomas B. Jones. *Electromechanics of Particles*. Cambridge University Press, Cambridge, 1995.

[132] Lung-Hsin Hung and Abraham P Lee. Optimization of droplet generation by controlling pdms surface hydrophobicity. In *ASME 2004 International Mechanical Engineering Congress and Exposition*, pages 47–48. American Society of Mechanical Engineers.

[133] Stefan Holm. *Microfluidic Cell and Particle Sorting Using Deterministic Lateral Displacement*. PhD Thesis. Lund University, 2018.

[134] A. B. Dalia and J. N. Weiser. Minimization of bacterial size allows for complement evasion and is overcome by the agglutinating effect of antibody. *Cell Host Microbe*, 10(5):486–96, 2011.

[135] J. L. Rodriguez, A. B. Dalia, and J. N. Weiser. Increased chain length promotes pneumococcal adherence and colonization. *Infect Immun*, 80(10):3454–9, 2012.

Paper I

Electrokinetic DLD

(The manuscript is not shown due to copyright reason)

Bacteria chain length sorting with DLD

Paper II

Analytica Chimica Acta 1000 (2018) 223–231

Contents lists available at ScienceDirect

Analytica Chimica Acta

journal homepage: www.elsevier.com/locate/aca

Separation of pathogenic bacteria by chain length

Jason P. Beech [a], Bao Dang Ho [a], Geneviève Garriss [b], Vitor Oliveira [b], Birgitta Henriques-Normark [b, c, d], Jonas O. Tegenfeldt [a, *]

[a] Division of Solid State Physics and NanoLund, Lund University, SE-221 00, Sweden
[b] Department of Microbiology, Tumor and Cell Biology, Karolinska Institutet, SE-171 77 Stockholm, Sweden
[c] Department of Clinical Microbiology, Karolinska University Hospital, SE-171 76 Stockholm, Sweden
[d] SCELSE and LKC, Nanyang Technological University, NTU, Singapore 639798, Singapore

HIGHLIGHTS

- Fractionation of the human bacterial pathogen, *Streptococcus pneumoniae*, into subpopulations based on morphological type.
- The results open up for detailed studies of the association of morphology and virulence mechanisms among bacteria.
- The fractionation tool is based on microfluidics and deterministic lateral displacement.

GRAPHICAL ABSTRACT

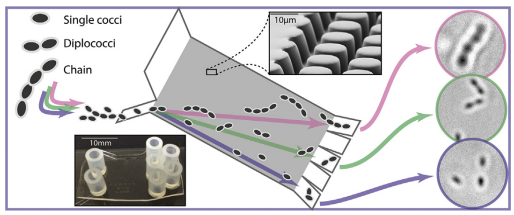

ARTICLE INFO

Article history:
Received 21 November 2017
Accepted 22 November 2017
Available online 25 November 2017

Keywords:
Deterministic lateral displacement
Separation
Bacterial virulence
Morphology

ABSTRACT

Using Deterministic Lateral Displacement devices optimized for sensitivity to particle length, we separate subpopulations of bacteria depending on known properties that affect their capability to cause disease (virulence). For the human bacterial pathogen *Streptococcus pneumoniae*, bacterial chain length and the presence of a capsule are known virulence factors contributing to its ability to cause severe disease. Separation of cultured pneumococci into subpopulations based on morphological type (single cocci, diplococci and chains) will enable more detailed studies of the role they play in virulence. Moreover, we present separation of mixed populations of almost genetically identical encapsulated and non-encapsulated pneumococcal strains in our device.

1. Introduction

1.1. Streptococcus pneumoniae

Streptococcus pneumoniae is a major human pathogen responsible for over a million deaths per year worldwide. The gram-positive *S. pneumoniae* is a round-shaped bacterium (coccus) that grows as a mixed population of various morphological types: single cocci, diplococci and chains of various lengths (Fig. 1). It is a common colonizer of the nasopharynx of preschool children but is also the causative agent of various invasive diseases such as pneumonia, septicemia and meningitis [1]. The different cell arrangements (single cocci, diplococci and chains), are thought to contribute differently to virulence and colonization. Previous studies show that long chains promote adherence to human lung epithelial cells *in vitro* and in colonization in a mouse model [2] while short chains better evade the complement, a component of the immune system [3]. One of the main virulence factors of *S. pneumoniae* is its

* Corresponding author.
E-mail address: jonas.tegenfeldt@ftf.lth.se (J.O. Tegenfeldt).

https://doi.org/10.1016/j.aca.2017.11.050

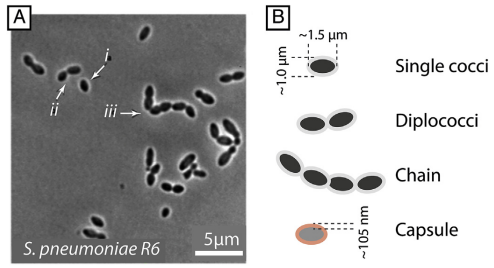

Fig. 1. Morphology of pneumococcal cells. (A) Phase-contrast micrograph of *S. pneumoniae* R6 (a non-encapsulated strain) showing i) single coccus ii) diplococcus and iii) chain of 4 cells (next to a diplococcus). (B) Definitions of different morphologies used in this work.

polysaccharide capsule that surrounds the bacterium [4]. More than 97 capsular serotypes of *S. pneumoniae* have been described to date, some of which are predominately associated with invasive disease or with colonization [5,6].

1.2. Microfluidics separation - deterministic lateral displacement

Deterministic Lateral Displacement (DLD) [7] is a microfluidic separation technique that has been applied to the label-free and continuous sorting of various biological particle systems. DLD devices contain ordered arrays of obstacles through which particles flow, see Fig. 2. As particles flow through the device, interactions with the obstacle arrays cause them to follow trajectories that depend on a combination of their size [7,8], shape [9–14], deformability [9,15,16] and dielectric properties [17]. Typically, the relative effects of these particle parameters on the particles' trajectories are determined by array parameters such as inter-obstacle distance and array tilt angle [7,8,18,19], obstacle shape [13,20,21] and device depth [9–11]. Tweaking these array parameters at the design stage allows us to choose which particle property (or properties) will dominate the particle behaviour and allows us to perform separations accordingly.

1.3. DLD for S. pneumoniae separations

Gaining a deeper understanding on how different morphological types contribute to the virulence of *S. pneumoniae* requires their separation into individual subpopulations. We designed DLD devices with the aim of sorting cultured *S. pneumoniae* cells into subpopulations based on cell size and morphological type, something that is otherwise impossible to achieve as this organism naturally grows as a mix of these morphological types. Ranjan et al. [12] showed some difference in the behaviour of differently shaped bacteria in DLD, using examples of cocci, coccobacilli and bacilli cells. They used H-shaped pillars and looked at how the rotation of single cells affected their trajectories. Many important human pathogens such as *Streptococcus pneumoniae*, *Staphylococcus aureus* and *Neisseria meningitidis* do not grow as single cells and are rather found in pairs, clusters or chains. We have previously separated trypanosomes (long thin microorganisms) from red blood cells (discoid cells) using DLD [10,11]. While hard spheres move in one of two trajectories determined by their diameter, long, thin particles (such as trypanosomes) move in a variety of modes with various rotational and morphological effects contributing to their trajectories, see Fig. 3. We used a similar approach here in designing a device that would be sensitive to different morphological types. We used the non-encapsulated *S. pneumoniae* strain R6 and the closely related encapsulated serotype 2 strain D39. Both are reference strains used as models for studying pneumococcal genetics and pathogenesis. In our device we separated genetically identical bacteria into morphological subpopulations and genetically similar strains from one another based on the presence of a capsule.

2. Methods

2.1. Device design

Our device was designed to focus a bacterial sample stream and collect 5 fractions that are laterally displaced by varying amounts, see Fig. 2 and the ESI for more details. The DLD array has circular posts with a diameter $D_p = 12$ µm with a gap width $G = 4$ µm. The period of the array $N = 23$. This gives us the critical diameter [18]:

$$D_C = 1.4 \times G \times N^{-0.48} = 1.24\ \mu m$$

The critical diameter was designed to be larger than single cocci (1 µm) but smaller than the length of diplococci and chains. The depth of the device was chosen to be 10 µm. Based on our previous experience of the behaviour of long thin particles in DLD devices we expected this depth to increase the effective size of the chains such

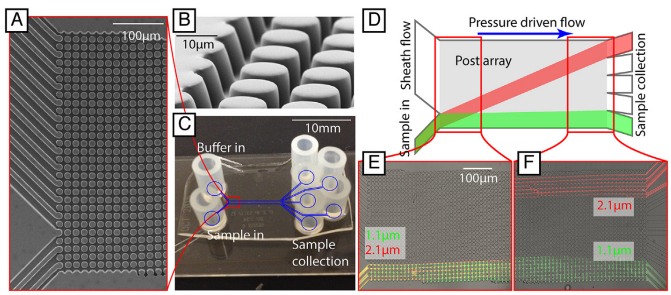

Fig. 2. Overview of a DLD device fabricated in PDMS. (A) and (B) DLD devices consist of pillar arrays through which particles flow. (C) Devices are fabricated in PDMS using replica moulding and bonded to glass slides. Tubes are attached to reservoirs and overpressure applied to both inlet reservoirs to generate flow. Separated fractions can be collected in the outlet reservoirs. (D) The mechanism of DLD causes particles to follow trajectories that depend primarily on their size and shape. (E) In this device 1.1 µm and 2.1 µm polystyrene beads are input into the array. The two different sized bead populations are completely separated and can be collected at different outlets (see ESI for more details).

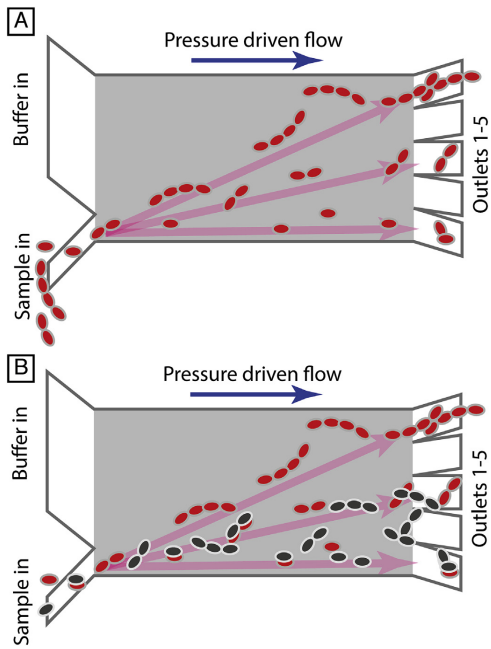

Fig. 3. Principles of sorting bacteria by morphology. (A) Displacement is a function of both cell width and chain length, longer particles are displaced more and fractions are generated at the device outlets. (B) Strains that grow in differing chain lengths can be separated. The presence of a capsule also affects trajectories (black colour illustrates non-encapsulated and red colour encapsulated cells). (For interpretation of the references to colour in this figure legend, the reader is referred to the web version of this article.)

that longer chains become more displaced than shorter chains, diplococci and single cocci of the same width.

The geometry of the DLD array and the positions of the outlet reservoirs were chosen such that the non-displaced fraction would be collected in reservoir 1, the fully displaced fraction (for hard spheres this would be the fraction with a diameter $> D_c = 1.24$ μm) would be collected in reservoir 5, and reservoirs 2–4 would collect the fractions with intermediate displacements.

2.2. Device fabrication

L-Edit 11.02 (Tanner Research, Monrovia, CA USA) was used for device design and photolithographic masks were ordered from Delta Mask (Delta Mask, Enschede, The Netherlands). Masters for replica moulding were fabricated in SU8 (SU8-2010, Microchem Corp., MA, USA) spun onto 3″ silicon wafers using UV-lithography (Karl Suss MJB4, Munich, Germany). After treatment of the master with an anti-adhesion layer of 1H,1H,2H, 2H-per-fluorooctyl-trichlorosilane (ABCR GmbH & Co. KG, Karlsruhe, Germany) [22] to facilitate demoulding, replicas were created in PDMS (Sylgard 184, Dow Corning, Midland, MI, USA) by standard replica moulding [23]. PDMS casts were oxygen plasma bonded to microscope slides spun with a thin layer of PDMS (Plasma Preen II-862, Plasmatic Systems Inc., North Brunswick, NJ, USA) to obtain devices with all internal surfaces consisting of PDMS. To prevent the sticking of cells to the internal surfaces of devices, their surfaces were treated immediately after bonding by filling the devices with 0.2% (w/v) PLL(20)-g [3.5]-PEG(2) (SuSoS AG, Dubendorf, Switzerland) in deionized water and allowing them to rest for at least 20 min before flushing them with deionized water for another 20 min. Silicon tubing with 3 mm inner and 5 mm outer diameter (228–0725 and 228–0707, VWR International LLC, Radnor, PA, USA) were glued (Elastosil A07, Wacker Chemie AG, Munich, Germany) onto the devices as reservoirs.

2.3. Experimental setup

Flow was generated in the device using an overpressure applied at the inlets with an MFCS-4C pressure controller (Fluigent, Paris, France) and the outlet reservoirs kept at ambient pressure. All images were taken through (1) An inverted Nikon Eclipse Ti microscope (Nikon Corporation, Tokyo, Japan) with an Andor NEO sCMOS camera (Andor Technology, Belfast, Northern Ireland) and Lumencor SOLA light engine™ (Lumencor Inc, OR, USA) with a FITC filter, or brightfield and (2) an inverted Nikon Eclipse Ts2 microscope (Nikon Corporation, Tokyo, Japan) with built in GFP optimized epifluorescence filter, or brightfield, and an Exmor USB 3.0 monochrome industrial camera (USB29 UXG M). In both cases 10x (Nikon, 0.25 NA, 7.23 WD), 20x (Nikon 0.40 NA, 3.9 WD), 60x water immersion (Nikon, 1.00 NA, 2.0 WD) or 100x oil immersion (Nikon 1.25 NA, 0.23 WD) objectives were used. All movies were acquired at 10 frames per second.

2.4. Bacterial strains, growth conditions and sample preparation

Streptococcus pneumoniae strains R6, R6 *hlpA-gfp*_Cam^r (BHN1226) and D39 *hlpA-gfp*_Cam^r (BHN1224) were grown in blood agar plates and incubated overnight at 37 °C in 5% CO_2. BHN1224 and BHN1226 were constructed by transforming a PCR product containing the *hlpA-gfp*_Cam^r locus [24] provided by J.-W. Veening into D39 and R6 as described in Ref. [24]. In order to minimize the adhesion of bacteria to the DLD device, cells were scraped from the plates and resuspended in a PBS +1% BSA solution at a final optical density (OD) of 1 (measured at 620 nm). Thanks to the surface coating of PLL-*g*-PEG (see above) we were able to run separations for several hours without any problematic clogging.

2.5. Hydrocarbon adherence assay

Pneumococcal surface hydrophobicity was determined by bacterial adherence to hexadecane as described elsewhere [25]. Briefly, three 5 mL cultures of each strain were grown to mid-log phase in Todd-Hewitt Broth supplemented with 0.5% Yeast Extract (THY), collected by centrifugation, washed twice and resuspended in 1 mL of PBS. The OD_{620nm} was measured and used as the control value (C0). 200 μL of hexadecane was added, the mixture was vortexed for 1 min and the phases allowed to separate. The OD_{620nm} of the aqueous phase was measured (CH). The percent hydrocarbon adherence (HA) was calculated as: HA = [(C0 - CH)/C0] x 100.

2.6. Bacterial cell count and viability

For counting bacterial cells, serial dilutions of the input sample and the fractions collected in the outlet were prepared in PBS. 10 μL of each dilution was spotted on blood agar plates and plates were incubated overnight at 37 °C in 5% CO_2. Colony forming units (CFU) were counted manually and the bacterial concentration (CFU/mL) was calculated. The impact of passage through the DLD device on bacterial cell viability was determined by counting the number of viable cells in the input sample and in each outlet. Survival was

expressed as the percentage of cells of the input sample recovered in the outlet. Survival was measured repeated twice with different input samples.

2.7. Bacterial cell size analysis

Size measurements of R6 and D39 cells were performed on microscopy images taken of the cells mounted on a standard microscope slide under a cover slip using a 100× oil immersion objective. A full description of the process can be found in the ESI.

2.8. Counting morphological types in separated fractions and unsorted samples

Separation results were determined by visual inspection of the cells collected in the outlet reservoirs of the device or from samples prior to separation. For counting in the outlets, images of 10s–100s of cells in each reservoir were randomized and analysed in a blind fashion (no knowledge of reservoir number) by experienced microbiologists. The microbiologists gave the cells the designation single cocci (for single cells), diplococci (for two cells attached together), or chains (for strings of 3 attached cells or more). The data was then compiled and plotted. More details can be found in the ESI. For experiments on the separation of R6 and D39 the fluorescence of the D39 cells was used to distinguish between the two strains.

3. Results

3.1. Morphology of S. pneumoniae

The D39 strain was found to have somewhat wider (1.09 ± 0.13 μm) and longer (1.43 ± 0.17 μm) cocci than R6 (0.92 ± 0.13 μm) and (1.32 ± 0.18 μm) respectively. D39 was also found to build longer chains (4.82 ± 1.17 μm) than R6 (3.78 ± 1.37 μm) in the culturing conditions used. The width and length distributions (irrespective of morphology) for the two strains are shown in Fig. 4A and B. Fig. 4C and D shows a breakdown of lengths for the different morphological types (single cocci, diplococci and chains). Interestingly there are significant overlaps

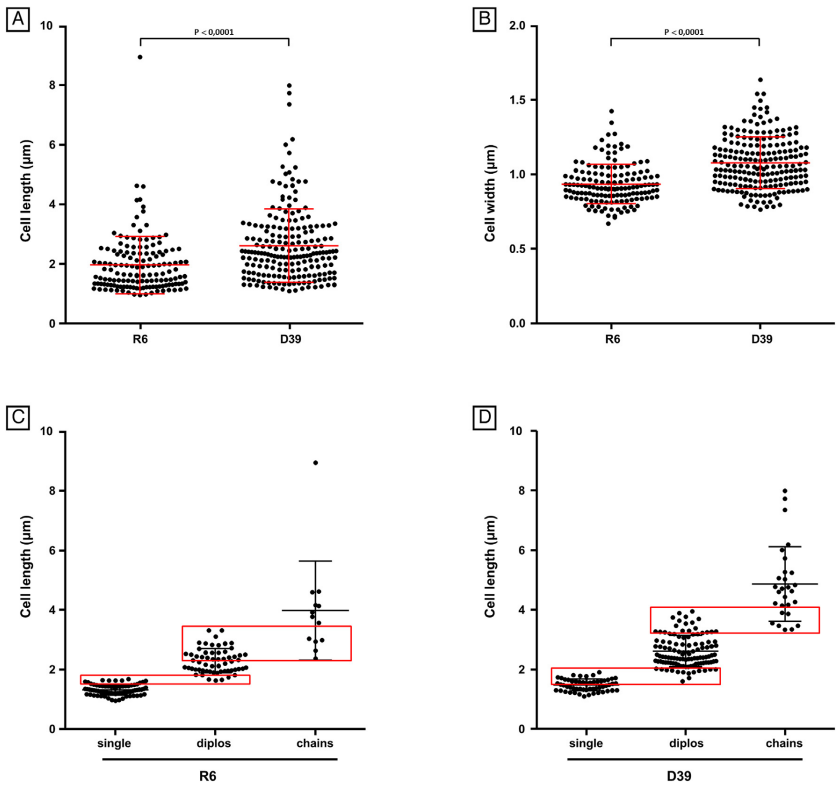

Fig. 4. Cell-size measurements. (A) Length of R6 and D39 cells. (B) Width of R6 and D39 cells. Each point represents a measured cell from 146 (R6) and 226 (D39) data points. The means are statistically different, based on an unpaired *t*-test analysis. The red lines represent the average and standard deviations for each group. (C) Length of R6 single cocci, diplococci and chains. (D) Length of D39 single cocci, diplococci and chains. Average and standard deviations are indicated. Red boxes indicate the overlap in sizes between different morphological types. (For interpretation of the references to colour in this figure legend, the reader is referred to the web version of this article.)

between the sizes of cocci and diploccoci, and diploccoci and chains for both D39 and R6. These differences might be due to cells being in various states of their replicative cycle and to variations in nutrient availability during growth and will be discussed in relation to the separation results in sections 3.5 and 3.6 below.

3.2. Surface properties of S. pneumoniae

Using a hydrocarbon adherence assay a previous study [25] showed that D39 and one of its non-encapsulated variant had significantly different hydrophobic characters, where the non-encapsulated strain was shown to be significantly more hydrophobic. We performed the same assay to confirm that we observed the same properties in our strains. As expected, the non-encapsulated strain R6 displayed much higher hydrophobicity (42.4 ± 2.10% adherence) than the encapsulated D39 strain (2.7 ± 0.16% adherence). These results corroborate the previously published data [25] and indicate that R6 and D39 could potentially be affected by different interactions with the device during separation.

3.3. Viability

We assessed the viability of two bacterial cell samples run through a device and collected during 2.5 h. We diluted the sample in the outlet and plated the bacterial cells on blood agar plates. Viability of both samples was >87%.

3.4. Sample recovery and throughput

We assessed the number of bacterial cells that could be recovered in the 5 outlets of our device by plating the samples recovered on blood agar plates and counting the CFU. After a 3-h run, during which the device was maintained upside-down (this facilitates sample recovery), we recovered between 15 and 1850 bacterial cells in the different outlets (specifically, outlet 1: 260; outlet 2: 250; outlet 3: 1850; outlet 4: 37; outlet 5: 15), in total 2412 bacterial cells. We estimated the volumetric throughput to approximately 1.0 μL/h based on measurements of the flow velocity of fluorescent beads in the device.

3.5. Chain length separations

For the non-encapsulated strain R6, specific morphological types were enriched in the different outlets of the device. Single cocci showed zero displacement and were enriched in outlet 1, whereas chains showed the most displacement and were enriched in outlet 5 (Fig. 5A). Diplococci, however, were found in all outlets (see discussion below in section 4). For the D39 strain results were similar (Fig. 5B). With both strains we significantly enriched single cocci and chains in outlets 1 and 5, respectively, when compared to unsorted samples (Fig. 5C and D).

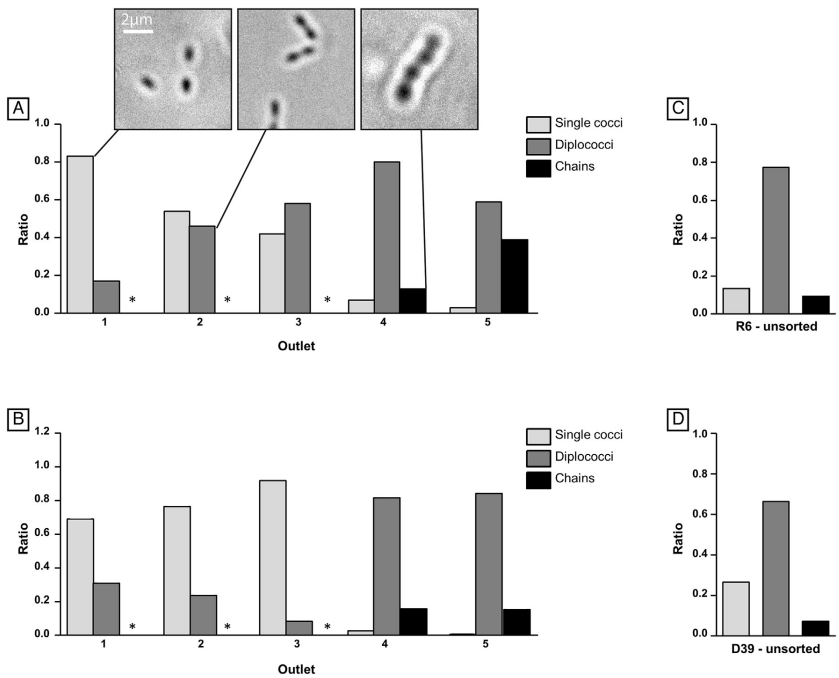

Fig. 5. Distributions of single cocci, diplococci and chains in outlet reservoirs after separation and in unsorted samples. (A) Distribution after separation, R6. Microscopy pictures of representative R6 single cocci, diplococci and chains in different outlets of the device are shown. (B) Distribution after separation, D39. Asterisks indicate that no chains were found. Distribution of each morphological type in unsorted R6 (C) and D39 (D) samples. Ratios were calculated by dividing the number of cells of each morphological type by the total number of cells in each sample or outlet.

3.6. Separation of R6 and D39

As shown in Fig. 6 the pneumococcal strains R6 and D39 could be separated. The majority of the D39 cells were displaced into outlet reservoirs 4 and predominantly 5, whereas almost all R6 were collected in reservoirs 1 to 3.

4. Discussion

Our device separates pneumococcal strains into morphologically different fractions. It is able to do this for both strains tested, R6 and D39, but the same approach should work for any bacteria that grow in chains, or indeed any long thin cells or particles. The mechanism of separation differs from that of hard, spherical particles that are bimodally separated into two fractions, one smaller than the critical size and one larger. Non-spherical entities move through the DLD array in a variety of modes, see Fig. 7, that lead to trajectories between zero displacement and maximum displacement. As shown in Fig. 7A, a diplococcus can move with zero displacement, despite one of its dimensions (length) being greater than D_c. This is due to a rotation of the cells (180° per row) that ensures that this dimension aligns with the flow and that the smaller width of the cells defines the effective size, which in this case is smaller than D_c. Fig. 7B and C shows a slightly larger diplococcus and a chain of 6 cells being displaced. In both cases the cells rotate 180° between each post in a motion that is reminiscent

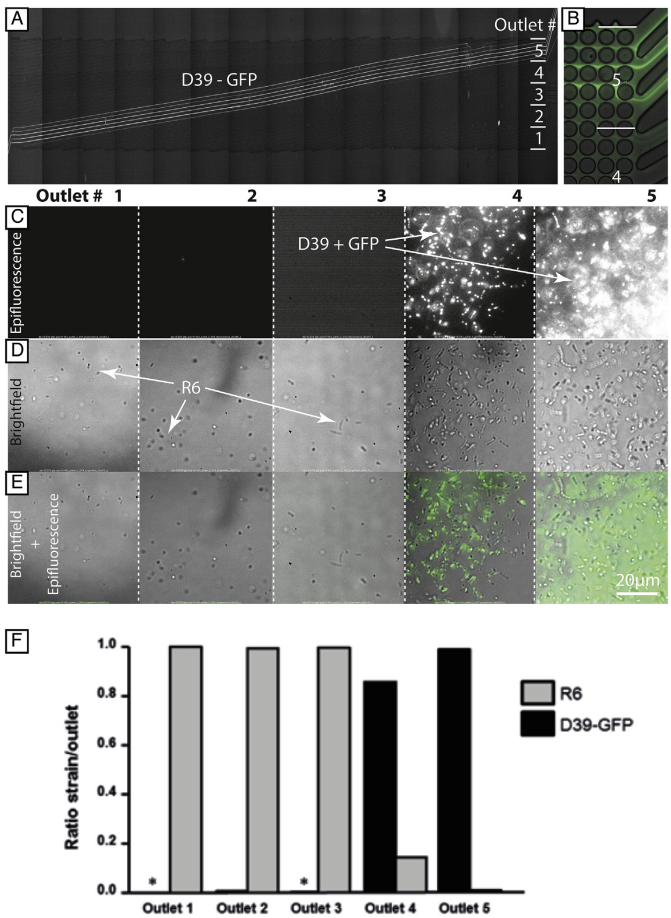

Fig. 6. Separation of R6 and D39. (A) A scanned image of the entire DLD array taken during a separation experiment. The mean trajectories of the fluorescent D39 cells can be seen. Note that the image is compressed in the x-direction. The length of the device is 9.5 mm and the width is 0.4 mm. (B) D39 cells predominantly exiting the device into outlet 5. (C) Fluorescent images taken in reservoirs show D39 cells. (D) In brightfield both R6 and D39 can be seen. (E) Strains can be identified by comparison of fluorescence and brightfield images. (F) Ratio of non-encapsulated (R6) and encapsulated (D39) cells in each of the 5 outlets of DLD device 8. Ratios were calculated by dividing the number of cells of each strain by the total number of cells in each outlet. Asterisks indicate that no D39 cells were found.

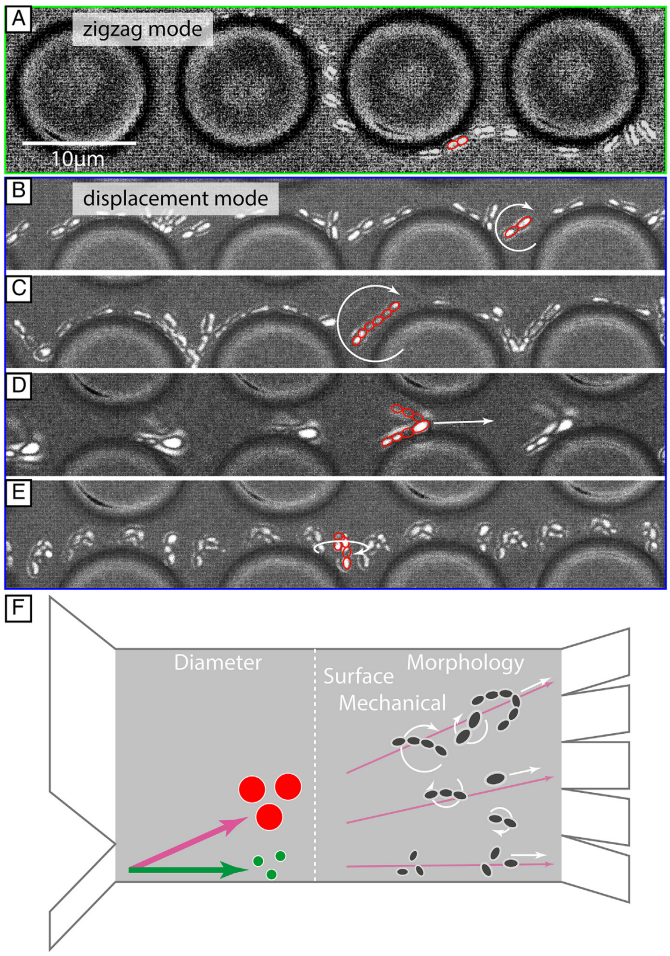

Fig. 7. Different transport modes for long thin particles in DLD. (A-E) Show a selection of the most common modes of transport for rod-like particles through the array (these images are extracted from movies that can be found in the ESI). (F) While hard spherical particles move in either displacement or zero displacement modes, rod-like diplococci and chains are distributed between the two based on length.

of a flick-flacking gymnast and has been called the flipping mode. Fig. 7D shows another mode that is common for very long and flexible particles. In this case a chain of 8–10 (narrow depth of focus compared to the length of the chain makes it hard to determine exactly) is bent into a parachute shape. Locked in this orientation the chain has the largest possible effective size. Fig. 7E shows a bent chain but in this case it appears to be too short or too bent to move in the parachute mode. The bent chain can be seen to rotate and move in the flipping mode. The movies from which the images in Fig. 7A–E were extracted can be found in the ESI.

The reason that a distribution of morphologies can be generated in a device with only two size-dependent modes can be understood in the following way. Long particles move in a variety of modes (flipping, parachuting), some of which cause displacement and some of which do not. The DLD array is long and a particle will sample several modes during transit through the device. Transitions from one mode to another can be triggered by random fluctuations of particle shape, by bending due to viscous forces, by interactions between particles or possibly by local fluctuations in the fluid flow. The wider or longer a particle is, the more likely it is to spend time in modes that lead to displacement and the greater the accumulated displacement will be at the end of the device as illustrated in Fig. 7F. This is evident in the greater displacement of the marginally larger D39 cells compared to the R6.

It is interesting that diplococci were found in all outlets in the experiments done with both R6 and D39. We were expecting some

overlap in the populations of cocci and diplococci and of diplococci and chains based on the size measurements shown in Fig. 4C and D where the sizes are seen to overlap. Upon analysis of the sizes of diplococci we found that we had actually separated the diplococci into size-based sub-populations. This difference in size was seen in the individual cells making up all morphological types (Figure S4 in the ESI). This size difference can likely be attributed to the cells being in various stages of their replicative cycle, or to varying levels of access to nutrients during growth. We can conclude that our approach has the power to resolve small differences in cells belonging to the same morphological type.

While we are able to greatly enrich the concentration of cocci in reservoir 1 and chains in reservoir 5 the presence of the diplococci is a problem. The performance of the device could be improved by emphasizing the purity of only one fraction. By increasing the size of the gaps in the array, diplococci would be less likely to displace than longer chains and purity could be improved. Conversely if a more pure fraction of cocci were required then a small decrease in the gap would cause diplococci to displace more and the purity of cocci would be improved. In both cases increasing the length and width of the array (with all other array parameters unchanged) would also improve separation since the probability that two morphologically different particles follow the same trajectory would decrease with the length of the path. A longer, wider device would also have space for a greater number of outlets and therefore a greater number of distinct populations could be resolved and collected.

The two strains of *S. pneumoniae*, R6 and D39, are almost genetically identical except for the presence of the capsule and a fluorescent marker: R6 (non-encapsulated, non-labeled) and D39 (capsulated, GFP-labeled). Despite this seemingly small difference the separation of the two strains was extremely efficient in our device, as can be seen in Fig. 6. While the separation results shown in Fig. 5 show that for each strain the different morphologies are distributed in all outlets this figure only shows the ratios of morphologies in each outlet, not the absolute number, which is harder to determine. The separation in Fig. 6 can be explained by a combination of the cell sizes and the distribution of morphologies for the two strains. Individual D39 cells are larger than R6 cells, as shown in panels A and B of Fig. 4 and, as can be seen in panels C and D, there is a much higher prevalence of larger diplococci and chains present for the D39 than the R6 strain. It is also possible that parameters other than size could influence the behaviour of the strains. It is unknown whether the mechanical properties of the diplococci and chains, specifically the stiffness, differs between the two strains. Further studies will show whether our method is sensitive to the rigidity of long particles or not but since DLD has been shown to be sensitive to the deformation of other particles [9,15], this is quite likely to be the case. What is more, as discussed in section 3.2, as measured by the hydrocarbon adherence assay, the presence of the capsule affects the hydrophobicity of the cells. Cells of the non-encapsulated R6 strain are much more hydrophobic than the capsulated D39 cells. Again, further studies will show whether hydrophobicity plays a role in the separation, or if it can be leveraged as a separation parameter. Here it is interesting to note that interactions between particles and posts, other than hard steric interactions, have been shown to greatly affect particle behaviour in DLD devices [17,26].

To summarize, Fig. 8 shows, by way of an illustration of a separation phase diagram, an overview of how our device works. Hard spherical particles fall along the diagonal line and are, if we neglect diffusion, either displaced (red zone) or not (green zone). Deformation causes particle to move away from the diagonal. Very deformable particles are able to move through the device even if they are larger than the gaps between the posts. Near to the critical

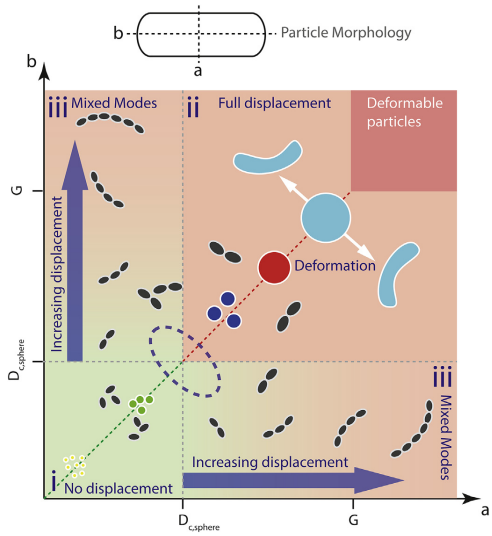

Fig. 8. An illustration of a separation phase diagram for a DLD device. On the axis are a and b, particle width and length. $D_{c,sphere}$ is the critical diameter in the device (the diameter at which a switch in trajectory occurs for hard spherical particles) and G is the gap between posts. The diagonal shows the bimodal separation of particles with $a = b < D_{c,sphere}$ from those with $a = b > D_{c,sphere}$. The coloured quadrants show i) Green, no displacement for particles with $a,b < D_{c,sphere}$. ii) Red, full displacement for particles with $a,b > D_{c,sphere}$. iii) Green/Red, mixed modes for a or $b > D_{c,sphere}$. As either a or b increases the trajectory of the particle approaches full displacement. The red area at top right ($a,b > G$) is unavailable for hard particles that are unable to pass between posts. However for deformable particles transit through the array is possible. Deformable particles become less spherical upon deformation and move away from the diagonal. This can cause them to move from the displacement to non-displacement modes. The blue dashed line illustrates where particles with a or b close to $D_{c,sphere}$ are sensitive to the effects of perturbations, particularly those arising from forces with a component perpendicular to the flow direction such as diffusion or non-steric interactions with posts.

size D_c trajectories are more likely to be sensitive to effects such as diffusion, particle post interactions and any other applied force, intentional or not. For long thin particles, even if they are narrow enough to theoretically move with zero displacement, the increasing length leads to higher probabilities that they spend time in modes that are associated with displacement.

5. Conclusions

We have shown the separation of cultured, pathogenic pneumococcal cells into fractions predominantly defined by their morphologies. We can enrich for single cocci or chains of 3 cells or longer and we describe strategies for the further improvement of future devices. We show the separation of two genetically similar strains, non-encapsulated R6 and encapsulated D39, based on small differences in size, possibly due to the presence of the capsule, and on differences in chain length. We successfully demonstrate collection of viable cells after sorting. While the throughput is moderate in this work, we expect it to be quite straightforward to increase the throughput to the levels necessary for detailed biomolecular studies of the resulting fractions by careful optimization of the device parameters, using wider devices, larger spacing between posts and parallelization. Overall, we believe that our work

will allow us to study virulence factors that have hitherto been difficult to study. What is more, our approach is not limited to the study of bacterial chains but opens up for separation of any high aspect ratio particles such as parasites and inorganic structures.

Acknowledgements

We thank Jan-Willem Veening for kindly providing us with the *hlpA-gfp*_Cam^r PCR product and Sulman Shafeeq for transformations yielding strains BHN1224 and BHN1226.

This work was carried out within NanoLund at Lund University with funding from LAPASO (EU FP7 project 607350) and the Swedish Research Council (VR) grants no. 2015-05426 and 2016-01861. In addition, the work was supported by funding from the Knut and Alice Wallenberg Foundation, the Swedish Foundation for Strategic Research and the Stockholm County Council with grant numbers SLL20170308 and SLL20160854. All device processing was conducted within Lund Nano Lab.

Appendix A. Supplementary data

Supplementary data related to this article can be found at https://doi.org/10.1016/j.aca.2017.11.050.

References

[1] N.F. Maraqa, Pneumococcal infections, Pediatr. Rev. 35 (7) (2014) 299–310.
[2] J.L. Rodriguez, A.B. Dalia, J.N. Weiser, Increased chain length promotes pneumococcal adherence and colonization, Infect. Immun. 80 (10) (2012) 3454–3459.
[3] A.B. Dalia, J.N. Weiser, Minimization of bacterial size allows for complement evasion and is overcome by the agglutinating effect of antibody, Cell Host Microbe 10 (5) (2011) 486–496.
[4] C. Hyams, et al., The Streptococcus pneumoniae capsule inhibits complement activity and neutrophil phagocytosis by multiple mechanisms, Infect. Immun. 78 (2) (2010) 704–715.
[5] J.Y. Song, M.H. Nahm, M.A. Moseley, Clinical implications of pneumococcal serotypes: invasive disease potential, clinical presentations, and antibiotic resistance, J. Korean Med. Sci. 28 (1) (2013) 4–15.
[6] S. Browall, et al., Intraclonal variations among Streptococcus pneumoniae isolates influence the likelihood of invasive disease in children, J. Infect. Dis. 209 (3) (2014) 377–388.
[7] L.R. Huang, et al., Continuous particle separation through deterministic lateral displacement, Science 304 (5673) (2004) 987–990.
[8] D.W. Inglis, et al., Critical particle size for fractionation by deterministic lateral displacement, Lab a Chip 6 (5) (2006) 655–658.
[9] J.P. Beech, et al., Sorting cells by size, shape and deformability, Lab a Chip 12 (6) (2012) 1048–1051.
[10] S.H. Holm, et al., Separation of parasites from human blood using deterministic lateral displacement, Lab a Chip 11 (7) (2011) 1326–1332.
[11] S.H. Holm, et al., Simplifying microfluidic separation devices towards field-detection of blood parasites, Anal. Methods 8 (16) (2016) 3291–3300.
[12] S. Ranjan, et al., DLD pillar shape design for efficient separation of spherical and non-spherical bioparticles, Lab a Chip 14 (21) (2014) 4250–4262.
[13] K.K. Zeming, S. Ranjan, Y. Zhang, Rotational separation of non-spherical bioparticles using I-shaped pillar arrays in a microfluidic device, Nat. Commun. (2013) 4.
[14] S.H. Au, et al., Microfluidic isolation of circulating tumor cell clusters by size and asymmetry, Sci. Rep. 7 (1) (2017) 2433.
[15] E. Henry, et al., Sorting cells by their dynamical properties, Sci. Rep. (2016) 6.
[16] D. Holmes, et al., Separation of blood cells with differing deformability using deterministic lateral displacement, Interface Focus 4 (6) (2014).
[17] J.P. Beech, P. Jonsson, J.O. Tegenfeldt, Tipping the balance of deterministic lateral displacement devices using dielectrophoresis, Lab a Chip 9 (18) (2009) 2698–2706.
[18] J.A. Davis, Microfluidic Separation of Blood Components through Deterministic Lateral Displacement, PhD thesis in Electrical Engineering, Princeton University, Princeton, NJ, USA, 2008.
[19] K.K. Zeming, et al., Asymmetrical deterministic lateral displacement gaps for dual functions of enhanced separation and throughput of red blood cells, Sci. Rep. (2016) 6.
[20] K. Loutherback, et al., Improved performance of deterministic lateral displacement arrays with triangular posts, Microfluid. Nanofluidics 9 (6) (2010) 1143–1149.
[21] J.C. Hyun, et al., Improved pillar shape for deterministic lateral displacement separation method to maintain separation efficiency over a long period of time, Sep. Purif. Technol. 172 (2017) 258–267.
[22] M. Beck, et al., Improving nanoimprint lithography stamps for the 10 nm features, Proc. 2001 1st Ieee Conf. Nanotechnol. (2001) 17–22.
[23] Y.N. Xia, et al., Replica molding using polymeric materials: a practical step toward nanomanufacturing, Adv. Mater. 9 (2) (1997) 147–149.
[24] M. Kjos, et al., Bright fluorescent Streptococcus pneumoniae for live-cell imaging of host-pathogen interactions, J. Bacteriol. 197 (5) (2015) 807–818.
[25] E. Swiatlo, et al., Contribution of choline-binding proteins to cell surface properties of *Streptococcus pneumoniae*, Infect. Immun. 70 (1) (2002) 412–415.
[26] K.K. Zeming, et al., Real-time modulated nanoparticle separation with an ultra-large dynamic range, Lab a Chip 16 (1) (2016) 75–85.

Electronic Supporting Information – Separation of bacteria by chain length

Jason P. Beech[a], Bao Dang Ho[a], Geneviève Garriss[b], Vitor Oliveira[b], Birgitta Henriques-Normark[b, c, d], Jonas O. Tegenfeldt[a]

[a] *Division of Solid State Physics and NanoLund, Lund University, SE-221 00, Sweden*
[b] *Department of Microbiology, Tumor and Cell Biology, Karolinska Institutet, SE-171 77 Stockholm, Sweden*
[c] *Department of Clinical Microbiology, Karolinska University Hospital, SE-171 76 Stockholm, Sweden*
[d] *SCELSE and LKC, Nanyang Technological University, NTU, Singapore 639798, Singapore*

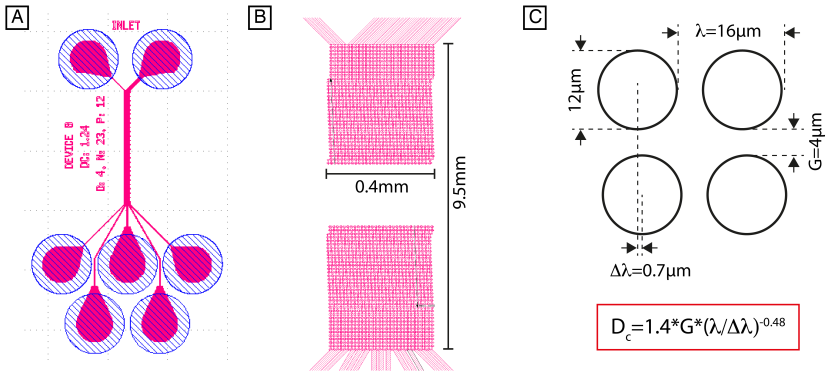

Figure S1. Device parameters. (A) An overview of the device taken from the mask design file. The blue circles indicate where inlet and outlet reservoirs are attached. (B) The DLD array dimensions. (C) The dimensions of the array itself and how they combine to give a give a critical diameter for particle separation.

1. DLD device parameters

Figure S1 gives an overview of our device parameters. Figure S1A shows the overall design with inlet and outlet channels. One of the inlet channel is denoted the sample inlet and the other the buffer inlet. The blue circles denote the positions of reservoirs that are attached to the PDMS/glass device. Figure S1B shows the dimensions of the separation array and Figure S1C shows the DLD array parameters.

Our device has gap width G = 4 μm and post diameter D_p = 12 μm. The center-to-center distance of the posts is given by $\lambda = G + D_p$ = 16 μm. Each row is shifted by $\Delta\lambda$ = 0.7 μm and the period of the array $N = \lambda/\Delta\lambda$ = 23. Using the equation for the critical diameter given by Davis [1]:

$$D_C = 1.4 \times G \times N^{-0.48} = 1.24\ \mu m$$

In order to test the device we first ran an experiment with fluorescent polystyrene microspheres 1.1 μm and 2.1 μm in diameter. A mixture of the two bead types in 0.1% SDS (to prevent adhesion of particles to the surface of the device) was introduced into the device via the sample inlet and a water solution of 0.1% SDS into the buffer inlet, both at 30 mBar. 400 frames @ 20 fps were captured using different

fluorescence filter sets to image each microsphere type individually. Averages were then created to show the trajectories of the particles. Colourised images of the particles at the beginning and end of the device are shown in Figure 2 of the main text. The 1.1 μm beads show zero displacement and the 2.1 μm beads are displaced by the maximum amount possible in this particular device geometry. We can conclude therefore that the critical size in the device lies between 1.1 μm and 2.1 μm. Due to lack of suitable sizes of microspheres we did not determine the exact critical size in the device. However, we conclude from our initial characterisation that the critical size in the device (in relationship to the size of the bacteria we are interested in) is in the correct range.

The depth of the device is 9.8 μm.

2. Morphology - Analysis of separated fractions

Separation results were determined by visual inspection of the cells collected in the outlet reservoirs of the device. Separations were run until the concentration of cells in the reservoirs was sufficiently high to obtain statistically significant results but low enough that individual cells could be identified. Movies of 200 frames were taken with a 60x long-working distance objective (Nikon, NA 1.00, WD 2.0). The focus was moved up and down slowly during the movie, which makes it easier to determine the morphology of cells that do not lie perfectly in the image plan. At least 4 movies per outlet reservoir were taken for each separation experiment with 10s to 100s of cells per movie. The movies were designated random names and then analyzed in a blind fashion by experienced microbiologists (coauthors: GG and VO). The microbiologists gave the cells the following designations: single cocci (for single cells), diplococci (for two cells attached together), or chains (for strings of 3 attached cells or more). The data was then compiled and plotted.

3. Cell size measurements

Size measurements of R6 and D39 cells were performed on microscopy images taken of the cells mounted on a standard microscope slide under a cover slip using a 100x oil immersion objective (Nikon 1.25 NA, 0.23 WD). The width and total length of units (cocci, diplococci and chains) was measured used NIS Elements software, as shown in Figure S2A. The pixel size was calibrated using an image of a ruler with 10 μm gradations using the same optical setup, Figure S2B. Cells appear larger when below or above the focal plane. In order to avoid errors due to this effect only in-focus cells were measured. Cells were deemed in-focus when they appeared dark with a minimal bright ring as shown in Figure S2A, inset, and the dark areas can be considered as the silhouettes of the cells where cell size can be measured, which can be confirmed in the superimposition of the bright field image and the fluorescence image of some R6-gfp bacteria in Figure S2C, where the green areas match with the dark areas in size.

To measure the width and the length of a cell, two pairs of parallel lines are positioned right at the boarder of the dark area of such cell, as shown in the inset of Figure S2A. If the cocci of a diplo or a chain did not line up, the length of each coccus were measured and then added up.

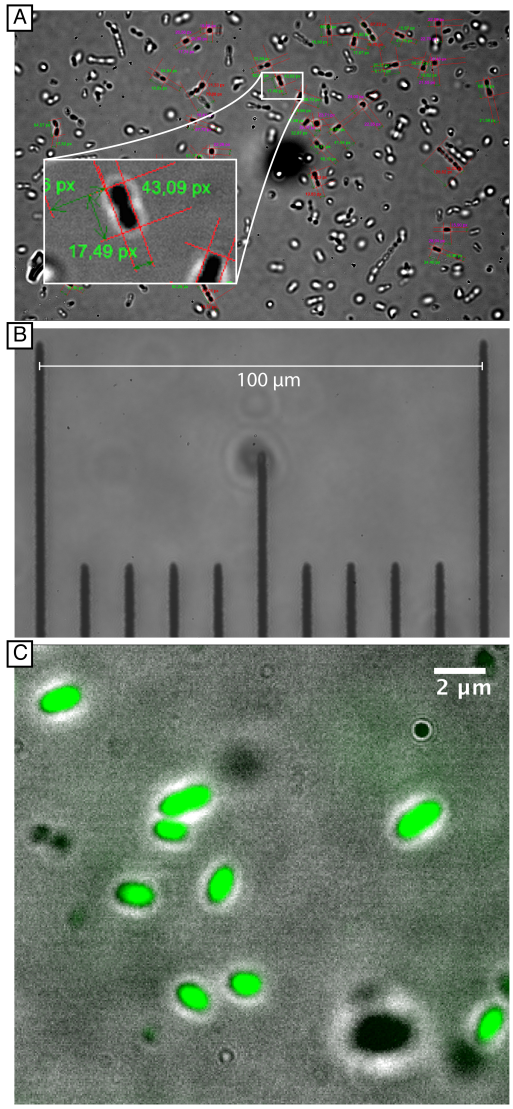

Figure S2. Cell-size measurements. (A) Both R6 and D39 were imaged on a microscope slide with a 100x oil immersion objective (Nikon 1.25 NA, 0.23 WD). To ensure that only cells in the correct focal plane were included, only those that appear dark with a small bright outlet were measured. (B) The pixel values were converted to lengths after calibration based on imaging of a ruler using the same imaging setup. (C) Superimposed bright field and fluorescence images of R6-gfp.

4. Hydrocarbon adherence assay

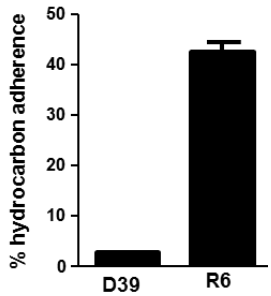

Figure S3. Pneumococcal surface hydrophobicity was determined by bacterial adherence to hexadecane as described elsewhere [2]. Bars represent the average of three measurements made on three cultures and standard deviations are indicated.

5. Size variation of diplococci in sorted fractions

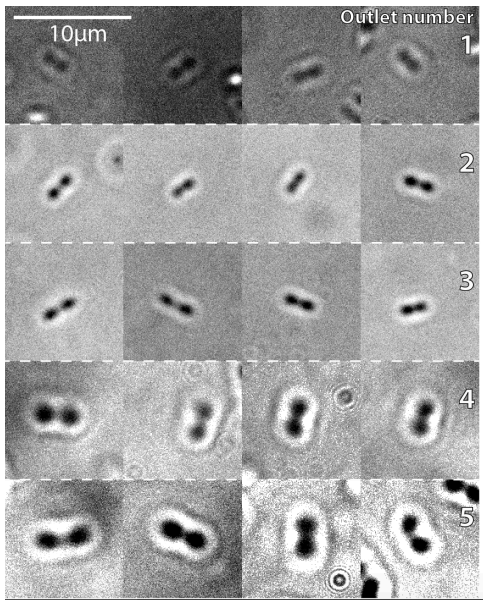

Figure S4. Size variation in sorted fractions of diplococci.

6. Movies

The movies in the ESI show the dynamics of the bacteria as they move through a device. They correspond to Figure 7A-E in the main text.

References

1. Davis, J.A., *Microfluidic Separation of Blood Components through Deterministic Lateral Displacement*, PhD thesis in *Electrical Engineering* (2008), Princeton University, Princeton, NJ, USA.
2. Swiatlo, E., et al., *Contribution of Choline-Binding Proteins to Cell Surface Properties of Streptococcus pneumoniae.* Infection and Immunity, 2002. **70**(1): p. 412-415.

Open DLD

Paper III

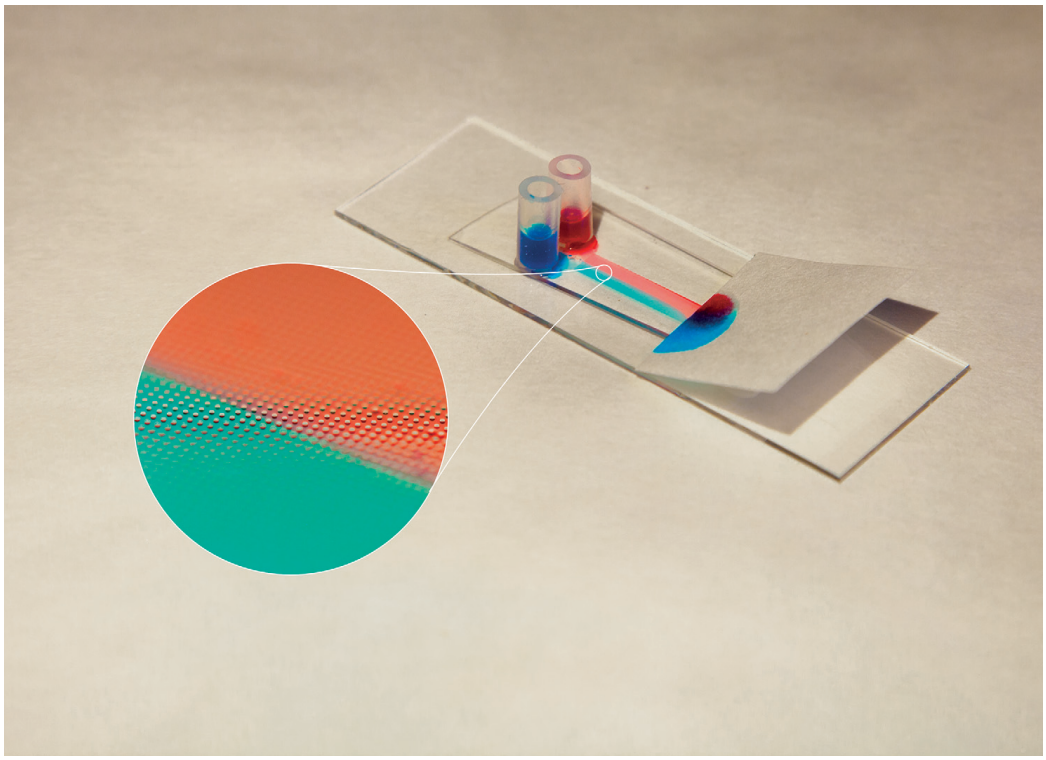

Featuring work from NanoLund, Prof. Jonas O. Tegenfeldt, Lund University, Sweden

A simple, low-cost and robust approach was developed for sorting complex samples using open-architecture fluidics. The liquid flow was driven by a paper capillary pump that doubles as a reservoir for collection of the sorted fractions.

Open channel deterministic lateral displacement for particle and cell sorting

Image reproduced by permission of Jason Beech/Tegenfeldt group

As featured in:

See Jonas O. Tegenfeldt *et al.*, *Lab Chip*, 2017, **17**, 3592.

ROYAL SOCIETY OF CHEMISTRY

rsc.li/loc

Registered charity number: 207890

Lab on a Chip

PAPER

View Article Online
View Journal | View Issue

Cite this: *Lab Chip*, 2017, **17**, 3592

Open channel deterministic lateral displacement for particle and cell sorting†

Trung S. H. Tran, Bao D. Ho, Jason P. Beech and Jonas O. Tegenfeldt *

Received 6th July 2017,
Accepted 18th September 2017

DOI: 10.1039/c7lc00707h

rsc.li/loc

We present the use of capillary driven flow over patterned surfaces to achieve cheap and simple, but powerful separation of biologically relevant particle systems. The wide use of microfluidics is often hampered by the propensity for devices to clog due to the small channel sizes and the inability to access the interior of devices for cleaning. Often the devices can only be used for a limited duration and most frequently only once. In addition the cost and power requirements of flow control equipment limits the wider spread of the devices. We address these issues by presenting a simple particle- and cell-sorting scheme based on controlled fluid flow on a patterned surface. The open architecture makes it highly robust and easy to use. If clogging occurs it is straightforward to rinse the device and reuse it. Instead of external mechanical pumps, paper is used as a capillary pump. The different fractions are deposited in the paper and can subsequently be handled independently by simply cutting the paper for downstream processing and analyses. The sorting, based on deterministic lateral displacement, performs equivalently well in comparison with standard covered devices. We demonstrate successful separation of cancer cells and parasites from blood with good viability and with relevance for diagnostics and sample preparation. Sorting a mixture of soil and blood, we show the potential for forensic applications.

Introduction

Cell separation is a critical process in cell biology, disease diagnostics and prognosis. While standard techniques such as FACS and MACS are widely used, there is a need to miniaturize systems in order to minimize sample and reagent use, simplify systems for the user, and integrate components into comprehensive analysis tools. Depending on the exact applications, different types of microfluidic sorting schemes may be utilized. Inertial[1] and acoustophoretic methods[2] give high volumetric throughput but with a relatively low size resolution and must be operated at low particle concentrations. Deterministic lateral displacement (DLD) is a method of particle separation, based on the continuous flow of particles through an array of obstacles that exhibits exceptional resolution in size-based separations.[3] DLD has been used for cell and bioparticle separations such as blood fractionation,[4–8] trypanosome enrichment from blood,[9,10] cancer cell isolation[11–13] and CTC cell cluster isolation from whole blood,[14] DNA and exosome separation,[15] and the separation of cells based on parameters other than size, namely shape and deformability,[16,17] and dielectric properties.[18] Early theoretical work by Inglis *et al.*[19] and Davis *et al.*[20] describing the critical size in DLD arrays has been improved upon by studying the effects of post shape.[21,22] Further improvements to theoretical descriptions have been made by considering other parameters such as diffusion,[23] dynamical properties,[17] and alternative trajectories through DLD arrays.[23–25] Being a passive method its basic operation does not require any application of external fields, like those used in acoustophoresis, and because it functions at high particle concentrations and low flow rates, relevant throughput can be achieved without the pressures required to generate the high particle velocities needed for inertial-effect based approaches. Even at high volume flow rates (10 mL min^{-1}) DLD has been shown to separate a variety of cells with minimal effect on viability.[12] Taken together, these qualities make DLD our method of choice for the development of a simple, cheap but effective approach to particle separation.

Here we show that by removing the lid of the DLD devices and using capillary flow we are able to perform separations, equally powerful as those in closed devices, but with many added advantages. While the benefits of open fluidics in general[26,27] and of capillary driven DLD has been demonstrated previously,[28,29] we here show proof of principle of their usefulness for sorting of biologically relevant particles not only based on size but also based on morphology and dielectric properties with relevance for *e.g.* medical diagnostics and

NanoLund and Division of Solid State Physics, Physics Department, Lund University, PO Box 118, 221 00, Lund, Sweden. E-mail: jonas.tegenfeldt@ftf.lth.se; Tel: +46 46 222 8063

† Electronic supplementary information (ESI) available. See DOI: 10.1039/c7lc00707h

forensics. What is more, this can be done in devices that are cheaper and easier to fabricate, since oxygen plasma and bonding is not required, and also cheaper and easier to run since pressure controllers are not required. A common limitation of standard fluidics devices, based on sealed small channels, is a propensity to clog, especially when handling complex samples. The difficulties to clean these closed devices make them unsuitable for prolonged and repeated use. We show that our open devices are easy to clean and reuse, which together with the use of the paper capillary pumps further contributes to the lowering of the costs. While standard pumps and pressure control units are ultimately more versatile, they are bulky, power consuming and expensive. We show that paper capillary pumps are compatible with open DLD devices allowing us to handle larger volumes than can fit into a device alone, and that they have the added advantage of doubling as sample collection substrates, further simplifying downstream process steps and analyses.

Results and discussion

Device fabrication and assembly

Both open and closed devices are fabricated in PDMS using replica molding on SU8 masters (see Materials and methods section). The final step in fabricating closed devices is to bond a glass slide to the PDMS cast and to then attach fluidics connectors. Open devices are much simpler in that they require neither of these two last steps. In order for the open device to function, PDMS must be rendered hydrophilic using *e.g.* oxygen plasma or, alternatively, prewetted by submersion in water. Fig. S3† in the supplementary material shows an overview of hydrophobic, hydrophilic and pre-wetted devices. Pre-wetting is much simpler to perform and negates the requirement of an oxygen plasma system, helping to keep the method cheap and simple. When a device is submerged in water the device features (channels and arrays) will fill with water after 5 minutes. When the PDMS slab is removed from submersion, water runs off of all flat areas and the only liquid remaining is that which is trapped within the patterned areas constituting the device. Sample can now be applied to the inlets and paper to the outlets and the sample will flow through the patterned areas of the device, confined to within the defined height of the features.

DLD devices in open configuration

Fig. 1A and B show a typical configuration of a closed DLD device. PDMS is bonded to glass to form closed channels and a pump or pressure control unit is used to drive flow through the device. As shown in Fig. 1C and D, our approach is to remove the glass lid and replace the pressure-driven flow with capillary flow. Provided the channels are hydrophilic, any aqueous solution placed at the inlet of the device will flow into the channels until they are filled. For our typical DLD devices (*e.g.* device 1, 20 mm length, 4 mm width and 24 μm depth, see ESI,† Fig. S1) the array volume is approximately 1.1 μL.

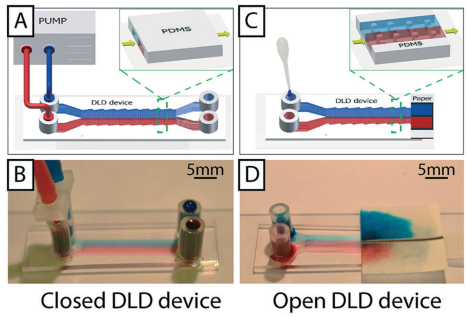

Fig. 1 Comparison of closed and open devices. (A and B) Conventional closed device where fluid is confined inside channels in a complicated setup of tubes and a pump or a pressure control unit. (C and D) Open DLD without lid. In these devices the interplay between surface tension and geometry keeps the fluid confined to the separation array and a paper reservoir at the outlet maintains flow, *via* capillary action, and collects the sample. We see, by observing the red and blue food coloring, that the flow is laminar in both devices.

To run the device, reservoirs are mounted at the device inlets and tested for volumes up to 60 μL using the paper capillary pump. At the beginning of the device there is a transition in liquid height from the reservoir to the bulk of the separation array. In this transition zone the sample flows across the top of the array, but the liquid height falls to that of the posts within 1–5 mm. Fig. 1D shows how we are able to maintain a stable, laminar flow (of red and blue food dye in this case) in the device using the paper capillary pump. The figure also shows how the fluids are collected in the paper. The resulting flow rates are measured to be 71 ± 19 nL s^{-1}, which is comparable to what we achieve with an applied pressure of 21 mBar in a corresponding closed device. This also compares well with a closed device driven by a paper capillary pump.

The liquid in the reservoirs gives a hydrostatic pressure that is less than 1 mBar and is therefore negligible in comparison with the equivalent driving pressure in a closed device. The result is that the liquid is pulled through the device by the negative pressure imposed by the capillary pump, minimizing any liquid build-up on top of the posts.

To estimate the liquid profile along the device we resorted to three approaches. Direct imaging (Fig. 2A and B) indicates that the liquid is indeed thicker at the beginning of the device close to the reservoirs and that it levels out rather quickly away from the reservoirs. Confocal imaging supports the conclusion giving a direct view of the profile (Fig. 2C–F). Finally we studied the flow in the channels. We measure the velocities of the flow (Fig. S4B†) and combine that with the cross sectional area of the device based on the design parameters to obtain a value of the volumetric flow. The resulting flow rate is consistent with what we obtain in direct measurements of the volumetric flow rate (Fig. S5†) and measurements of the average flow by measuring the elapsed time

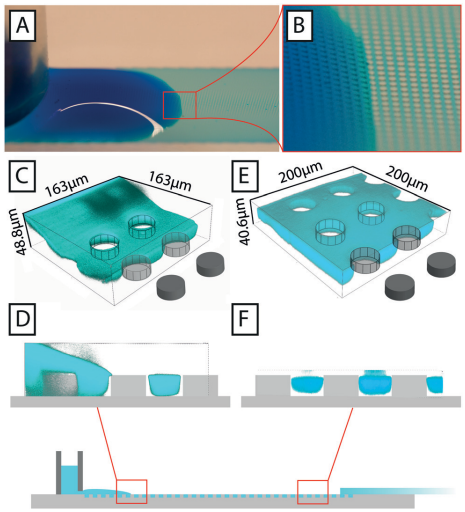

Fig. 2 Images of aqueous fluids in an open DLD device. A) Photograph of an aqueous solution of food color in an open device. B) Close-up of the transition between the area where the fluid forms a droplet and where it is confined to the post array. C) and D) 3d rendering and cross section, respectively, of confocal images of an aqueous solution of FITC in the same device, taken near to the reservoir. The drop formed by the reservoir can be seen to fall below the height of the posts. E) and F) 3d rendering and cross section, respectively, at the end of the device closest to the paper. The device is filled with liquid but no liquid can be seen above the posts.

between loading of a defined volume and the emptying of the reservoirs (Fig. S4D†) suggesting that the liquid is indeed filling the device to the top of the pillars. Note that there is a trend of lower flow velocities close to the reservoirs, in line with the local buildup of liquid on top of the post array that we observe by direct inspection.

The throughput of the paper capillary pump driven device is ultimately limited by the absorption rate of the paper. In a very simplified but illustrative picture the paper capillary pump can be viewed as a battery with an internal resistance and a hydromotive force in analogy to standard electrical batteries. If the external load is much less than the internal flow resistance, the flow rate is limited by the internal resistance. By measuring the flow rates in a free paper as well as a paper connected to a device (Fig. S5†), we could estimate the internal resistance, 16×10^{12} kg s^{-1} m^{-4}, which is within an order of magnitude of the resistance of our closed devices, 30×10^{12} kg s^{-1} m^{-4} (from Fig. S4†), and open devices 23×10^{12} kg s^{-1} m^{-4} (from Fig. S5†). From these data we could also estimate the hydromotive force to 32 mBar. Higher throughputs can now be realized by decreasing the device flow resistance through an increase in the depth of the devices or by using paper pumps with higher absorption rates. While the flow in narrow strips of paper follows the Washburn law[30] such that the flow rate is inversely proportional to the square root of time, we use wider strips of paper where the liquid fans out leading to a constant flow rate as shown by Mendez *et al.*[31] To obtain specific volumes and flow rates as a function of time, the paper capillary pumps can be programmed by selecting appropriate geometries of the paper.[32–34] Further details on the flow generated in our open devices by the paper capillary pump can be found in the ESI.†

In addition to the simplifications compared to standard DLD devices we can demonstrate good separation performance. Fig. 3B shows the separation of 3 μm and 7 μm polystyrene microspheres. The sample (a mixture of the two beads) was placed in one inlet and buffer placed in the other. As the sample stream flows through the device, in parallel with the buffer stream, the mechanism of DLD causes the 7 μm particles, which are larger than the critical size, D_c, to be displaced into the buffer stream while the 3 μm particles, which are smaller than D_c remain in the sample stream. This lateral displacement is caused by steric interactions between particles and posts, which cause particles to move with a component perpendicular to the flow direction. The net result is the continuous, spatial separation of particles, Fig. 3B, in this case based on size. We also show here how the particles are collected in the paper, in regions divided by wax lines, which we will return to below. Despite the lack of a lid in our open DLD devices, flow is well defined and confined to the pillar array, and high-resolution separations can be performed fully comparable to those demonstrated for closed DLD devices. Fig. 3C shows experimental comparison of 3 devices and 10 particle sizes run in open configurations. Filled circles show particles following the flow (as expected if they are below the critical size) and open circles show those that are displaced (above the critical size). These points fall on either side of the expected critical size (indicated by red double arrows) as calculated using the empiric expressions given by Inglis *et al.*[35] and Davis *et al.*[20] for closed devices demonstrating good correspondence between particle behavior in open and closed configurations.

Application areas – proof of principle

To show the applicability of open DLD devices to relevant bio-separations, we tested separation of a range of relevant bioparticles in different modalities, as described below.

Size-based separation. Deterministic lateral displacement provides a powerful mechanism for highly precise continuous sorting based on size. In addition to the size-based separation of polystyrene beads shown above (Fig. 3) we show the separation of cells of higher biological relevance. Fig. 4A shows the size-based separation of cells from a breast cancer cell line (MCF7 cells with diameter 17.3 ± 2.1 μm) from erythrocytes (red blood cells, RBC) (diameter 7.8 ± 0.6 μm) in an open device with D_c = 10.7 μm (device 2, see ESI,† Fig. S1) and Fig. 4B shows the size-based separation of white blood cells (WBC) (diameter 12.2 ± 0.9 μm) and RBCs in a device with D_c = 5.1 μm (device 1, see ESI,† Fig. S1). In both cases

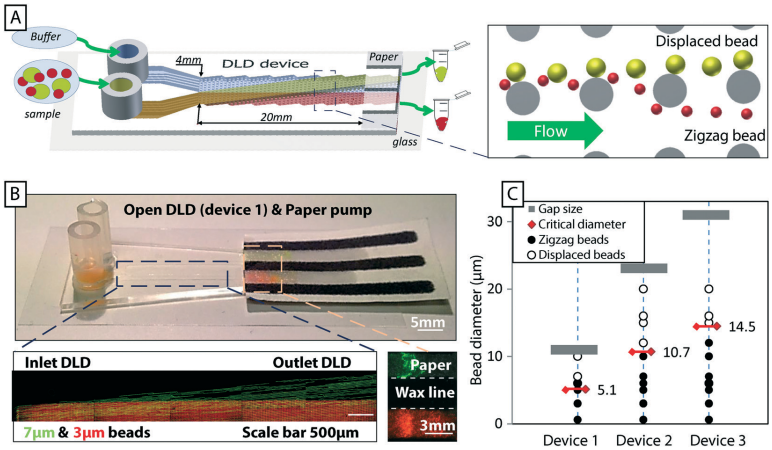

Fig. 3 An overview of open DLD, device layout and typical results. (A) Particles are introduced *via* one inlet and buffer *via* the other. The mechanism of deterministic lateral displacement pushes particles (yellow) larger than a critical size, D_c, from the sample stream to the co-flowing buffer stream as they move along the device. Smaller particles (red) remain in the sample stream. (B) Paper is used both as a capillary pump and as a method of sample collection. Here colored beads are visualized after separation and collected in zones in the paper pump defined with wax (yellow/green 7 μm and red 3 μm, black lines are wax). Time averaged images of fluorescent beads (green 7 μm and red 3 μm) in the beginning and end of the device show the trajectories of the beads in the device, which lead to separation. Note the collection of particles in separate, wax-delimited zones in the paper. (C) The behavior of open DLD devices is consistent with that of standard closed DLD devices. The red double arrows indicate theoretical critical sizes for a conventional closed device based on Davis' estimate.[20] The results for the open DLD are shown with filled black circles for particles in zigzag mode (following the flow), and open circles for particles in displacement mode (displaced into the buffer stream). The grey bars indicate the upper limit of the particle sizes as imposed by the gap sizes between posts.

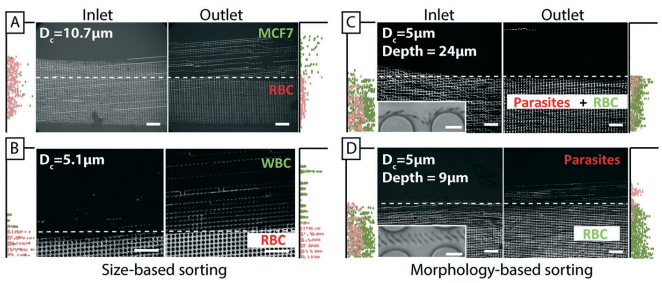

Fig. 4 Cell and parasite sorting in open DLD devices. All images show plots of inlet distributions (to the left) and outlet distributions (to the right) together with time-averaged micrographs of different cells moving through open DLD devices. The micrographs show the trajectories of the different cells in each case and the outlet distributions show the resulting separations. (A) Size-based separation of RBCs (red dots) and MCF7 cells (green dots) (B) sizebased sorting of RBCs (red dots) and WBCs (green dots) (C) in a 24 μm deep device RBCs (green dots) and parasites (*T. cyclops*) (red dots) have the same trajectories, but in a shallower device (9 μm deep) (D) they are separated. Scale bars 100 μm and 10 μm for the insets.

the performance of the devices in the simpler open configuration is equivalent to that of the same device with a lid and pressure-driven flow.

Morphology-based separation. To leverage the differences in morphology of bioparticles as a separation parameter, DLD devices can be made in which the orientation of non-spherical particles is controlled. In this way a specific aspect of the shape can be selected to influence the effective size of the particles.[9,36] As in previous work, but now in the open device, we control the orientation of parasites to optimize their separation from erythrocytes. In a 24 μm deep device 4 (Fig. 4C), both RBCs and parasites follow the flow, whereas in a 9 μm deep device 5 (Fig. 4D) RBCs follow the flow but parasites are displaced and separation is achieved based on the same principle as was shown in ref. 9 and 36. Device parameters are shown in ESI,† Fig. S1.

Complex samples. We demonstrate the robustness of the open DLD by introducing a mixture of soil and blood into a

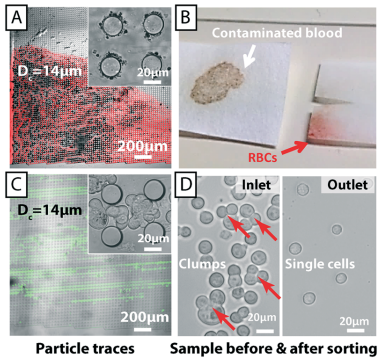

Fig. 5 Sorting of complex samples in open DLD devices. Even if large particles become trapped at the beginning of a device they do not block the flow of liquid and smaller particles as they would in a closed device. This allows extremely "dirty" samples to be analysed. A mixture of soil and RBCs is introduced into an open device. Despite the large amount of soil particles trapped at the beginning of the device (A), a clean fraction of RBCs is collected at the end of the device (B). (C) & (D) A combination of filtering and continuous separation of suspensions of cells containing large clusters that would otherwise block the inlets of a closed device.

device (Fig. 5). Soil sediments quickly and sticks in the separation array, as can be seen in Fig. 5A, but this does not cause the flow to stop. RBCs are still able to traverse the post array and a soil free fraction of RBCs is readily collected in paper at the end of the device (Fig. 5B).

A common challenge in microfluidics is the aggregation of cells that often lead to clogging even with careful surface passivation. Using the open DLD we clearly demonstrate the retention of cell aggregates of MCF7 cells while the individual cells are collected at the end of the device (Fig. 5C and D). While cell aggregates may be of interest in their own right,[37] in many cases, such as in cell culturing, drug screening and fluorescence activated cell sorting, it is often necessary to remove cell aggregates. Those experiments are conducted in device 3 with D_c = 14 μm (see ESI,† Fig. S1).

Application of electric fields

Electrokinetic effects can be utilized in DLD devices to widen the scope and add specificities associated with the distribution of charge on the particles of interest as shown previously by Beech *et al.*[18] in closed DLD devices. We added electrodes to the inlet and outlet reservoirs of a DLD device generating an electric field in the device. The electric field lines were "squeezed" between the insulating PDMS posts and field gradients were generated near the post surfaces. Polarizable particles interacted with the field gradient and the resulting dielectrophoretic (DEP) forces were used to modify the DLD-based behavior and tune size-based separations. Because there is no lid on an open device it is easy to access the fluid at any point in the device, during a separation. In the example shown in Fig. 6 electrodes are dipped into the fluid (KCl with a conductivity of 24 mS m^{-1}) and an AC electric field is applied. In a closed device the electrodes are usually mounted in the inlet and outlet reservoirs, which are 30 mm apart in this device. Here we could easily place them 3 mm apart allowing for the generation of much higher fields at a given voltage. In Fig. 6B we see the effects of adding an electric field. In the absence of an applied voltage, 3.1 μm sulphate-terminated polystyrene and 4.8 μm carboxy-terminated polystyrene microspheres are following the flow (zigzagging), which is to be expected in a device with a critical diameter of 5.1 μm (device 1, see ESI,† Fig. S1), showing that the electrodes do not greatly perturb the flow. At 400 V applied AC voltage (100 Hz) the 4.8 μm microspheres are displaced and separation is achieved. At 700 V, all microspheres are displaced.

Applying electrodes in this manner, rather than in the inlets and outlets, decouples the electrode geometry from the flow geometry in a very simple way, giving us freedom to apply any number of electrodes in any pattern and at any angle to the flow direction.

Sample collection and recovery

The paper at the end of the device functions not only as a capillary pump but also as a sample recovery matrix from which fractions can be cut in a manner similar to that shown by Osborn *et al.*[38] Filter paper with a thickness of 150 μm and a pore size of 25–60 μm has excellent absorption. Liquid reservoirs of the required volume can be defined using a wax printer. The wax lines serve to maintain the separation of collected fractions (Fig. 1, 3 and 7). Fluorescent samples with good signal can be imaged directly in the paper with low magnification (Fig. 3 and 7). For samples with lower, or no fluorescent signal, higher magnification together with transmitted light can be used to image cells. In Fig. 7 separated MCF7 cells and RBCs are imaged inside the paper reservoirs.

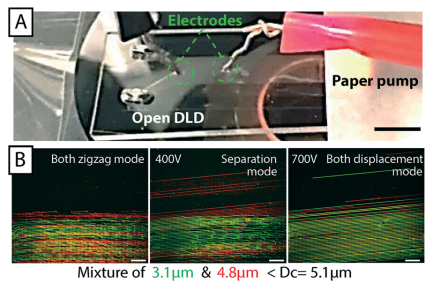

Fig. 6 Combination of electrokinetics and open DLD. (A) With direct access to the fluid it is straight-forward to position external electrodes at any point in the device. Scale bar 3 mm. An AC field at 100 Hz and various applied voltages (B) 0 V/400 V/700 V, change the trajectories of particles consistent with what was previously shown by Beech *et al.*[18] in closed DLD devices. Scale bars 100 μm.

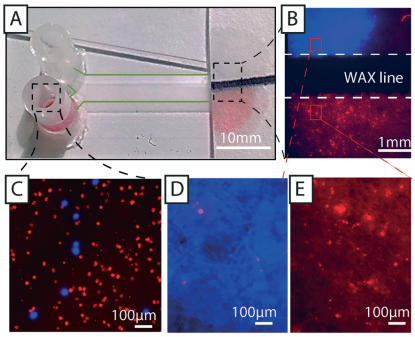

Fig. 7 Paper functions both as a capillary pump and as a collection reservoir for separated cells. (A and C) A sample containing RBCs (red fluorescence) and MCF7 cells (blue fluorescence) is introduced into an open DLD. RBCs (smaller than D_c) and MCF7 cells (larger than D_c) follow different trajectories through the device (from left to right) and can be collected to the right in two areas on the paper, separated by a printed wax line. The RBCs are more numerous than the MCF7 cells and can easily be seen in the paper through their red color (no fluorescence). Note the green dotted line that delineates the boarders of the device. (B) Trapped MCF7 cells and RBCs imaged in the paper. The high concentration makes it difficult to pick out individual cells in the image, but as (D) shows, very few RBCs were observed in the top zone where the MCF7 fraction dominates. (E) No MCF7 cells are seen in the RBC fraction.

To recover cells from the paper, we have developed a simple protocol that does not negatively affect viability or proliferation (Fig. 8). The desired fractions are cut out of the paper and placed inside a liquid medium of choice (*e.g.* in a 1.5 mL Eppendorf tube). Gentle vortexing releases most of the collected sample from the paper and subsequent centrifugation may then be performed to concentrate and/or collect the freed cells or particles. Fig. 8D shows a micrograph of MCF7 cells after separation in an open device, release from paper, and collection *via* centrifugation. Fig. 8E shows the recovery of 75% of cells from filter paper using this method.

While having good absorptive qualities, which is good for maintaining flow, fibrous filter paper with large pore size, is not ideal for sample collection due to trapping of particles and cells within the structure of the paper. Instead a two-layer paper system was used to increase the collection rate. By sandwiching a layer of filter membrane (1 μm pore size, polycarbonate membrane) between the filter paper and the device, the good absorptive qualities of the filter paper could be used while the polycarbonate membrane stopped the particles/cells from entering the paper and becoming trapped. Particles and cells captured on the surface of the polycarbonate membrane were easily resuspended with higher yields observed. Fig. 8E shows how 95% of cells could be recovered using the extra membrane layer.

To measure the effect of sorting in both open and closed devices on the health of cells, we performed viability and proliferation assays of MCF7 cells. Cell counting using viability dyes (trypan blue) was conducted to measure the percentage of viable cells and the rate of proliferation. Fig. 8F demonstrates viabilities of >90% for sorted cells. A small difference in the viability of cells (control, open, and closed devices) could be seen in our measurements but the difference has no practical significance and shows nothing more than the

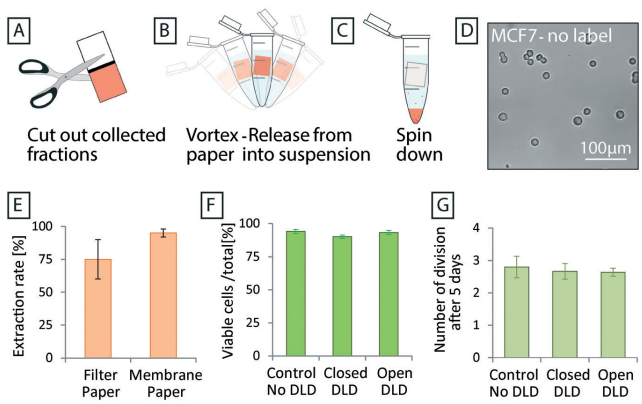

Fig. 8 Post-separation sample recovery. (A) Separated fractions are accumulated in the paper and kept separated by hydrophobic wax lines. The desired fractions are collected separately by dividing the paper along the wax line. (B) To re-suspend the collected fractions vortexing is used, which shakes the cells free of the paper matrix, followed by (C) centrifugation. (D) MCF7 cells after separation and collected using the process described in (A)–(C). (E) Recovery statistics for the filter paper and the two-layer system. Error bars show max/min values from 5 experiments. (F) Cell viability and (G) proliferation assay for MCF7 after separation in closed and open DLD. Error bars show the standard deviation in (F) and (G). No significant difference could be seen in the proliferation rates of sorted and non-sorted cells.

common variation between cultures using these cells. Furthermore, Fig. 8G shows that after 5 days of culturing, no difference in the proliferation rates of cells, (~2.5 divisions in 5 days), can be seen as a consequence of sorting.

The performance of the devices is qualitatively comparable to the conventional closed devices with clear separation of the different fractions. Purity and capture rate are performance parameters that do not depend on the DLD as much as on the overall design and will have to be optimized carefully for each specific application. For example the paper capillary pump in Fig. 3B can be extended to three lanes instead of two. In that way the purity of the sample collected in the two extreme lanes can be enhanced by discarding the central lane. The data in Fig. 4 shows clearly that by appropriate choice of cut-offs we would be able to achieve close to 100% purity of the separated fractions. With longer devices, this is expected to be done with minimum loss of capture efficiency.

Cleaning and reusing devices

The fouling of devices with particles and cells is the most common reason for device failure and limits device lifetime. Fouling can be due to several mechanisms. Particles can adhere to surfaces and they can become trapped because they are too large to move through constrictions. These mechanisms are also linked. For example, particles can stick to one another, forming agglomerations that are much more likely to get stuck. Fig. 9A shows an image of 4.5 and 10 μm particles that have become stuck in a closed device with a D_c = 5.1 μm and gap size of 11 μm after operating for 30 min (device 1, see ESI,† Fig. S1). At this point the device has ceased to work and particles are no longer able to enter the array. This kind of clogging is detrimental for all kinds of microfluidics devices, in particular for DLD devices since a well-defined flow direction is crucial for the successful operation. Even a small deviation of flow direction may change the critical size significantly.

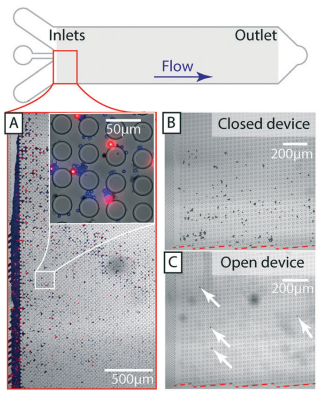

Fig. 9 Cleaning and reusing open DLD devices. (A) Depending on the array parameters, particle sizes and surface chemistries, devices eventually clog. (B) A closed device after attempted cleaning using sonication, high pressures and reversing the flow direction. (C) An open device after sonication and rinsing is almost completely free of particles (30 times fewer). Those remaining are highlighted with arrows. Channel walls are shown in red dashed lines.

Closed devices are most often irreversibly sealed (to avoid leaking) and are difficult to clean and reuse. Fig. 9B shows the same device after sonication, reversal of the flow direction and an increase in pressure in an effort to remove clogging. Despite these efforts many particles remain stuck in the device and the device is unusable. Open devices are considerably easier to clean and can be cleaned to a much higher degree. Fig. 9C shows the same kind of device as above after first being run in an open configuration and then cleaned by sonication and rinsing. This device is free of particles after rinsing and can be reused.

Conclusion

We have shown that by combining patterned surfaces in PDMS with paper based capillary pumps we can fabricate potentially cheap, simple to use, and reusable continuous flow separation devices. We have demonstrated proof-of-principle separations of samples based on size and morphology and what is more, in samples containing very large contaminant particles. Being open, access to flowing fluid is possible in these devices allowing for easy electric contact through electrodes. Flow rates can be held constant by choice of size and properties of the paper used in the capillary pump. Paper is not only useful as a pump but also as a matrix for the collection of separated fractions. The separational functionality of DLD is retained in open devices paving the way for simple, robust and clogging insensitive sorting using pillar arrays with potential applications in medicine and forensic science. Our device opens up for sample preparation applications in paper fluidics based diagnostics.[39,40]

The limitations and challenges introduced by working with open devices on the other hand include the risk for evaporation, contamination and biohazard.[41] These issues can be mitigated through a cover that is positioned in close proximity, yet not in contact with the actual device.

Materials and methods

PDMS device fabrication

In a contact mask aligner (Karl Suss MJB3 and MJB4, Munich, Germany), negative photoresist SU8 (MicroChem, Newton, MA, USA) spun on a 3″ silicon wafer was exposed with UV light through a chrome-mask designed in L-Edit 11.02 (Tanner Research, Monrovia, CA USA) and printed by Delta Mask (Delta Mask, Enschede, The Netherlands). Before casting of PDMS, a monolayer of 1*H*,1*H*,2*H*,2*H*-perfluorooctyltrichlorosilane (ABCR GmbH & Co. KG, Karlsruhe, Germany) was applied in the gas phase to the master

as an anti-adhesion agent to facilitate demoulding. A 10 : 1 mixture (monomer : curing agent) of PDMS (Sylgard 184, Dow Corning, Midland, MI, USA) was degassed, poured onto the master then baked for 2 hours at 80 °C. For the closed devices vias are punched and an oxygen plasma treatment step (Plasma Preen II-862, Plasmatic Systems, Inc., North Brunswick, NJ, USA) is performed to enable bonding to glass slides and the attaching of silicone tubes for fluidic connections, none of which are necessary for the open devices. In Fig. S2† (supplementary of device fabrication), a comparison among a protocol of closed DLD fabrication and optional protocol for open DLD fabrication (with and without oxygen plasma plus reservoir) is presented.

Paper capillary pump

A two-layer paper system was used as a capillary pump and for sample capture and collection for the experiments described in Fig. 8. For liquid absorption (Herzberg flow rate[42] 110 s/100 mL), filter paper of 0.15 mm thickness, a 25–60 μm pore size and 8 μm particle retention (Grade 600, VWR, Sweden) was used. For sample capture a layer of polycarbonate paper (Grade 28158, VWR, Sweden), (1 μm pore size) was sandwiched between the separation device and the lower grade filter paper. For the other experiments only the filter paper was used. Wax barriers were printed onto the filter paper using a wax printer (ColorQube 8570, Xerox, USA) followed by baking for 3 minutes at 100 ° C.

For the experiments characterizing the evaporation, a grid was printed onto the paper to facilitate measurement of the wetted area. The grid was printed using a standard laser writer (Canon iR-ADV C5250i).

Sample preparation (beads, RBCs, WBCs, parasites and MCF7 cells)

Fluorescently labeled polystyrene microspheres with varying diameters (from 1 μm to 20 μm) (Polyscience Inc., Warrington, PA, USA) were suspended in MilliQ water and 1% SDS and used in both closed and open DLD devices for calibration.

Small volumes of blood (10 μL) were obtained from healthy, consenting donors *via* finger pricking. Blood samples were diluted 20 times in autoMACS™ running buffer (Miltenyi Biotec, Auburn, CA, USA).

Trypanosoma cyclops parasites were thawed (after storage in 10% dimethyl sulfoxide (DMSO, Fluka, St. Louis, MO, USA: 41639) at −80 °C) and cultured in Cunningham's medium with 20% fetal calf serum (FCS, Sigma-Aldrich) at 28 °C. Parasites were harvested after proliferating to cover 80% of the culture dish and spiked into blood samples.

MCF-7 (breast carcinoma cell lines obtained from the American Type Culture Collection (ATCC)) was cultured at 37 °C and 5% CO_2. Cell culture medium was Dulbecco's modified Eagle's medium (DMEM), 10% FBS and 1% penicillin streptomycin (Sigma-Aldrich). After one week of subculture, the cells proliferated to fill more than 80% of the culture flasks and were considered ready for separation experiments.

Image acquisition and analysis

Particle and cell distributions were calculated from images acquired using an inverted epifluorescence microscope (Nikon Eclipse Ti, Nikon Corporation, Tokyo, Japan) and scientific CMOS camera (Flash4.0 V2, Hamamatsu, Japan). ImageJ 1.48v software downloaded from the National Institutes of Health, and NIS-elements 4.51 were used for image analysis and the preparation of figures. Images of particle trajectories are generated by time-averaging. Two color-images generated by adding color to separate images, taken in succession with different filter sets, and superimposing.

Conflicts of interest

There are no conflicts to declare.

Acknowledgements

We thank Stefan Holm and Bo Baldetorp for their kind donation of trypanosomes and MCF-7 cells respectively. This work was carried out within NanoLund at Lund University with funding from the Child Cancer Foundation (MT2013-0031), LAPASO (EU FP7 project 607350) and the Swedish Research Council (VR) grant no. 2015-05426. All device processing was conducted within Lund Nano Lab. We thank Christelle Prinz for valuable comments after carefully reading the manuscript.

References

1 D. Di Carlo, D. Irimia, R. G. Tompkins and M. Toner, *Proc. Natl. Acad. Sci. U. S. A.*, 2007, **104**, 18892–18897.
2 T. Laurell, F. Petersson and A. Nilsson, *Chem. Soc. Rev.*, 2007, **36**, 492–506.
3 L. R. Huang, E. C. Cox, R. H. Austin and J. C. Sturm, *Science*, 2004, **304**, 987–990.
4 J. A. Davis, D. W. Inglis, K. J. Morton, D. A. Lawrence, L. R. Huang, S. Y. Chou, J. C. Sturm and R. H. Austin, *Proc. Natl. Acad. Sci. U. S. A.*, 2006, **103**, 14779–14784.
5 D. W. Inglis, M. Lord and R. E. Nordon, *J. Micromech. Microeng.*, 2011, **21**, 054024.
6 C. I. Civin, T. Ward, A. M. Skelley, K. Gandhi, Z. P. Lee, C. R. Dosier, J. L. D'Silva, Y. Chen, M. Kim, J. Moynihan, X. C. Chen, L. Aurich, S. Gulnik, G. C. Brittain, D. J. Recktenwald, R. H. Austin and J. C. Sturm, *Cytometry, Part A*, 2016, **89A**, 1073–1083.
7 K. K. Zeming, T. Salafi, C. H. Chen and Y. Zhang, *Sci. Rep.*, 2016, **6**, 22934.
8 M. Yamada, W. Seko, T. Yanai, K. Ninomiya and M. Seki, *Lab Chip*, 2017, **17**, 304–314.
9 S. H. Holm, J. P. Beech, M. P. Barrett and J. O. Tegenfeldt, *Lab Chip*, 2011, **11**, 1326–1332.
10 S. H. Holm, J. P. Beech, M. P. Barrett and J. O. Tegenfeldt, *Anal. Methods*, 2016, **8**, 3291–3300.

11 Z. B. Liu, F. Huang, J. H. Du, W. L. Shu, H. T. Feng, X. P. Xu and Y. Chen, *Biomicrofluidics*, 2013, **7**, 011801.
12 K. Loutherback, J. D'Silva, L. Y. Liu, A. Wu, R. H. Austin and J. C. Sturm, *AIP Adv.*, 2012, **2**, 042107.
13 H. Okano, T. Konishi, T. Suzuki, T. Suzuki, S. Ariyasu, S. Aoki, R. Abe and M. Hayase, *Biomed. Microdevices*, 2015, **17**, 59.
14 S. H. Au, J. Edd, A. E. Stoddard, K. H. K. Wong, F. Fachin, S. Maheswaran, D. A. Haber, S. L. Stott, R. Kapur and M. Toner, *Sci. Rep.*, 2017, **7**, 2433.
15 B. H. Wunsch, J. T. Smith, S. M. Gifford, C. Wang, M. Brink, R. L. Bruce, R. H. Austin, G. Stolovitzky and Y. Astier, *Nat. Nanotechnol.*, 2016, **11**, 936–940.
16 J. P. Beech, S. H. Holm, K. Adolfsson and J. O. Tegenfeldt, *Lab Chip*, 2012, **12**, 1048–1051.
17 E. Henry, S. H. Holm, Z. M. Zhang, J. P. Beech, J. O. Tegenfeldt, D. A. Fedosov and G. Gompper, *Sci. Rep.*, 2016, **6**, 34375.
18 J. P. Beech, P. Jonsson and J. O. Tegenfeldt, *Lab Chip*, 2009, **9**, 2698–2706.
19 D. W. Inglis, J. A. Davis, R. H. Austin and J. C. Sturm, *Lab Chip*, 2006, **6**, 655–658.
20 J. A. Davis, *Doctoral thesis*, Princeton, 2008.
21 Z. Zhang, E. Henry, G. Gompper and D. A. Fedosov, *J. Chem. Phys.*, 2015, **143**, 243145.
22 K. Loutherback, K. S. Chou, J. Newman, J. Puchalla, R. H. Austin and J. C. Sturm, *Microfluid. Nanofluid.*, 2010, **9**, 1143–1149.
23 B. R. Long, M. Heller, J. P. Beech, H. Linke, H. Bruus and J. O. Tegenfeldt, *Phys. Rev. E*, 2008, **78**, 046304.
24 J. Frechette and G. Drazer, *J. Fluid Mech.*, 2009, **627**, 379–401.
25 S. C. Kim, B. H. Wunsch, H. Hu, J. T. Smith, R. H. Austin and G. Stolovitzky, *Proc. Natl. Acad. Sci. U. S. A.*, 2017, **114**, E5034–E5041.
26 J. Melin, W. van der Wijngaart and G. Stemme, *Lab Chip*, 2005, **5**, 682–686.
27 B. P. Casavant, E. Berthier, A. B. Theberge, J. Berthier, S. I. Montanez-Sauri, L. L. Bischel, K. Brakke, C. J. Hedman, W. Bushman, N. P. Keller and D. J. Beebe, *Proc. Natl. Acad. Sci. U. S. A.*, 2013, **110**, 10111–10116.
28 J. P. Beech and J. O. Tegenfeldt, Capillary driven separation on patterned surfaces, *microTAS 2009, The 13th International Conference on Miniaturized Systems for Chemistry and Life Sciences*, Jeju, Korea, November 1–5, 2009, pp. 785–787.
29 K. Morton, O. K. C. Tsui, C. K. Tung, J. C. Sturm, S. Y. Chou and R. Austin, *New J. Phys.*, 2010, **12**, 085008.
30 E. W. Washburn, *Phys. Rev.*, 1921, **17**, 273–283.
31 S. Mendez, E. M. Fenton, G. R. Gallegos, D. N. Petsev, S. S. Sibbett, H. A. Stone, Y. Zhang and G. P. Lopez, *Langmuir*, 2010, **26**, 1380–1385.
32 E. Elizalde, R. Urteaga and C. L. Berli, *Lab Chip*, 2015, **15**, 2173–2180.
33 P. Yager, T. Edwards, E. Fu, K. Helton, K. Nelson, M. R. Tam and B. H. Weigl, *Nature*, 2006, **442**, 412–418.
34 B. M. Cummins, R. Chinthapatla, B. Lenin, F. S. Ligler and G. M. Walker, *Technology*, 2017, **5**, 21–30.
35 D. W. Inglis, J. A. Davis, R. H. Austin and J. C. Sturm, *Lab Chip*, 2006, **6**, 655–658.
36 S. H. Holm, J. P. Beech, M. P. Barrett and J. O. Tegenfeldt, *Anal. Methods*, 2016, **8**, 5726–5726.
37 A. F. Sarioglu, N. Aceto, N. Kojic, M. C. Donaldson, M. Zeinali, B. Hamza, A. Engstrom, H. Zhu, T. K. Sundaresan, D. T. Miyamoto, X. Luo, A. Bardia, B. S. Wittner, S. Ramaswamy, T. Shioda, D. T. Ting, S. L. Stott, R. Kapur, S. Maheswaran, D. A. Haber and M. Toner, *Nat. Methods*, 2015, **12**, 685–691.
38 J. L. Osborn, B. Lutz, E. Fu, P. Kauffman, D. Y. Stevens and P. Yager, *Lab Chip*, 2010, **10**, 2659–2665.
39 Y. Yang, E. Noviana, M. P. Nguyen, B. J. Geiss, D. S. Dandy and C. S. Henry, *Anal. Chem.*, 2017, **89**, 71–91.
40 K. Yamada, H. Shibata, K. Suzuki and D. Citterio, *Lab Chip*, 2017, **17**, 1206–1249.
41 Y. Temiz, R. D. Lovchik, G. V. Kaigala and E. Delamarche, *Microelectron. Eng.*, 2015, **132**, 156–175.
42 W. Herzberg, *Papierprüfung*, Springer, Berlin, Heidelberg, 1921, p. 109, DOI: 10.1007/978-3-662-25211-6_18.

Open Channel Deterministic Lateral Displacement for Particle and Cell Sorting

Trung S.H. Tran, Bao D. Ho, Jason P. Beech and Jonas O. Tegenfeldt

Electronic Supporting Information

Design and fabrication

The basic operational principle of DLD along with relevant parameters and critical separation diameters for our DLD devices are shown in Figure S1.

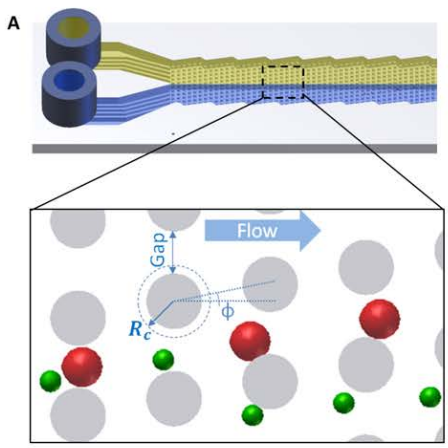

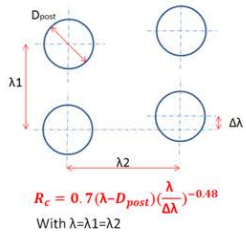

C

Device	Dpost	Gap	Dc	Depth
1	30	11	5.1	24
2	30	23	10.7	24
3	30	31	14.4	24
4	20	12	5	24
5	20	12	5	9

***Figure S1**. (A) Schematic of a typical DLD device with particle trajectories, (B) Key parameters determining the critical diameter (D_c) of a DLD array, (C) List of DLD devices used in this report (length units are µm). Length of the devices is 20 mm and width is 4 mm.*

Several fabrication and surface treatment schemes were tested for our devices (Figure S2). Figure S2A shows the conventional method of fabricating closed PDMS/glass devices with a plasma-bonding step (that also renders the PDMS hydrophilic) and the attachment of reservoirs/pressure control connections.

Preparation of devices

For the open devices, if a drop of aqueous solution is applied at the end of an untreated (hydrophobic) DLD array, the droplet will stay on the surface and will not wet the channels or array area of the device. This can be overcome in two ways. Figure S2B shows an open device in which the channels are selectively rendered hydrophilic by use of a mask during oxygen plasma treatment. The untreated, hydrophobic PDMS surrounding the active area of the device serves to confine the sample, which would otherwise spread outside the features of the device. Another approach, that is simpler because oxygen plasma is not needed, is

shown in Figures S2C and D. By submerging the device in an aqueous solution (1% SDS for polystyrene bead sorting, AutoMacs™ for RBC, and complete Dulbecco's Modified Eagle's Medium (DMEM) for cancer cell experiments) at room temperature for 5 minutes, the entire surface of the device can be forced to wet. When the device is removed from the solution the flat PDMS surface is sufficiently hydrophobic to repel the aqueous solution, but the water inside the structures of the device remains. After the positioning of the paper capillary pump at the outlet and the addition of more sample at the inlet, flow is maintained and separation can be performed. The reservoir, shown in Figure S2D, is not essential but allows for greater control of the sample and the handling of larger sample volumes.

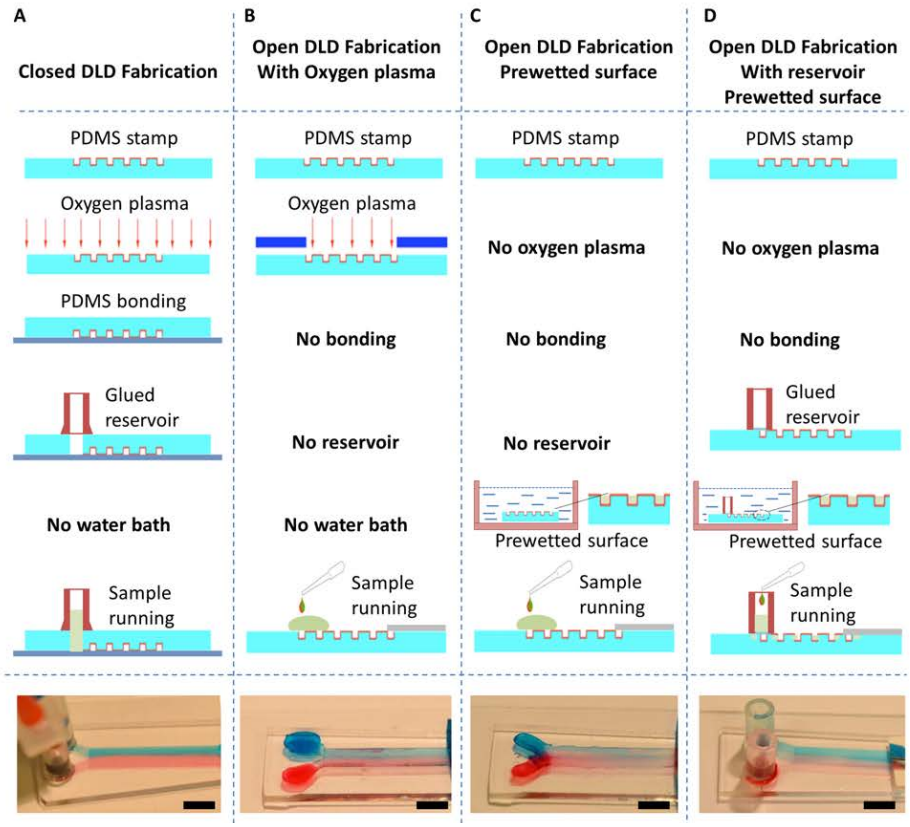

***Figure S2**. Comparison of different fabrication methods for closed and open DLD devices. (A) Conventional closed device fabrication. (B) Open device where the sorting structures are selectively treated with oxygen plasma to make them hydrophilic. (C) Rendering the PDMS hydrophilic by immersion (prewetting) in a water bath (plain water at room temperature in 5 minutes) instead of in an oxygen plasma. (D) Addition of a reservoir gives better control of the sample and allows for larger volumes. Scale bars 5 mm.*

The wetting of the devices using the different surface treatment strategies was characterized in more detail as presented in Figure S3. Selective oxygen plasma treatment gives a strongly hydrophilic surface with contact angle ~ 0°. Immersing the device in aqueous buffer gives a less hydrophilic surface (contact angle ~ 60° outside the device and an effective contact angle ~ 0° in the DLD array). The latter approach is fully adequate for the operation of the device and much simpler as it does not require any oxygen plasma equipment.

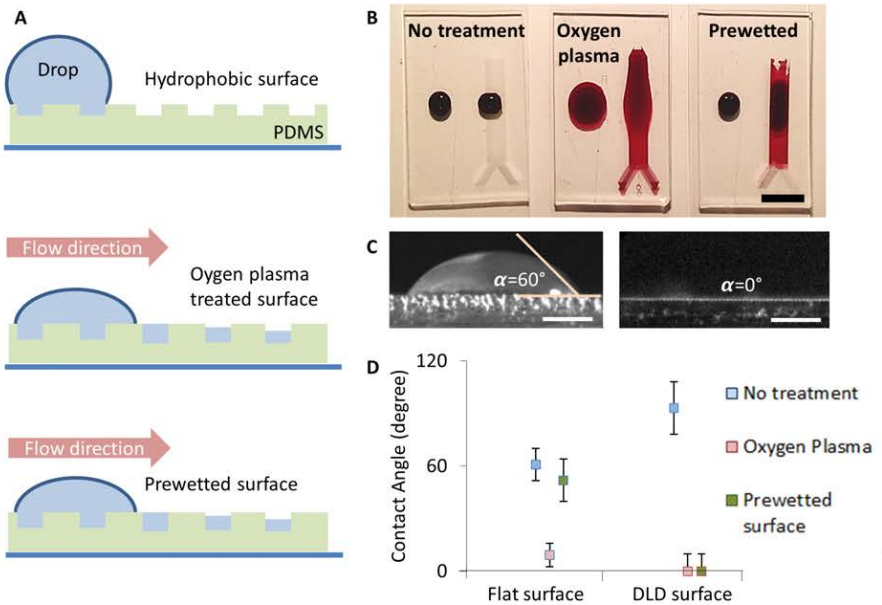

***Figure S3**. Hydrophobic and hydrophilic devices. (A) Schematic of a water droplet on an untreated (hydrophobic) surface and the two treated hydrophilic surfaces (B) Visualization of the wetting behavior of the three kinds of surface treatments on flat and patterned PDMS using an aqueous solution of red food coloring. (C) Cross-sectional view of water drop outside and on the DLD array for a prewetted surface. (D) Comparison of wetting angles on flat and patterned surfaces after no treatment, oxygen plasma and prewetting. The error bars represent the standard deviation of the measurement.*

Volume of a filled device

The volume of the liquid in a filled device is calculated based on the table in figure S1C. The ratio of the area of the fluid and the total area of the unit cell is 0.58, which is multiplied with the overall dimensions of the device (length 20 mm, width 4 mm and depth 24 µm), giving us the total volume of device 1 of 1.1 µL.

Uniformity of wetting

The characteristics and uniformity of the wetted array are characterized by confocal microscopy and direct imaging with a macro objective. In both cases device 3 was used with added reservoirs. For the confocal images fluorescein isothiocyanate (FITC) was first dissolved in methanol to 10% that was in turn diluted in water 100 times and the methanol

allowed to evaporate. The confocal microscope is based on a Yokogawa CSU22 spinning disc, Andor laser combiner and Andor iXon DU-897 CCD camera on an inverted Nikon Ti microscope. A Plan 50x ELWD Dry and a Plan Fluor ELWD 40x Ph2 ADL objective with NA 0.32 and 0.4 respectively where used for figures 2C-F. Since the microscope is inverted, the device was turned upside-down for imaging (surface tension dominates and so this has little to no effect on the shape of the liquid surface). The image contrast was adjusted such that scattered light was rejected from the image.

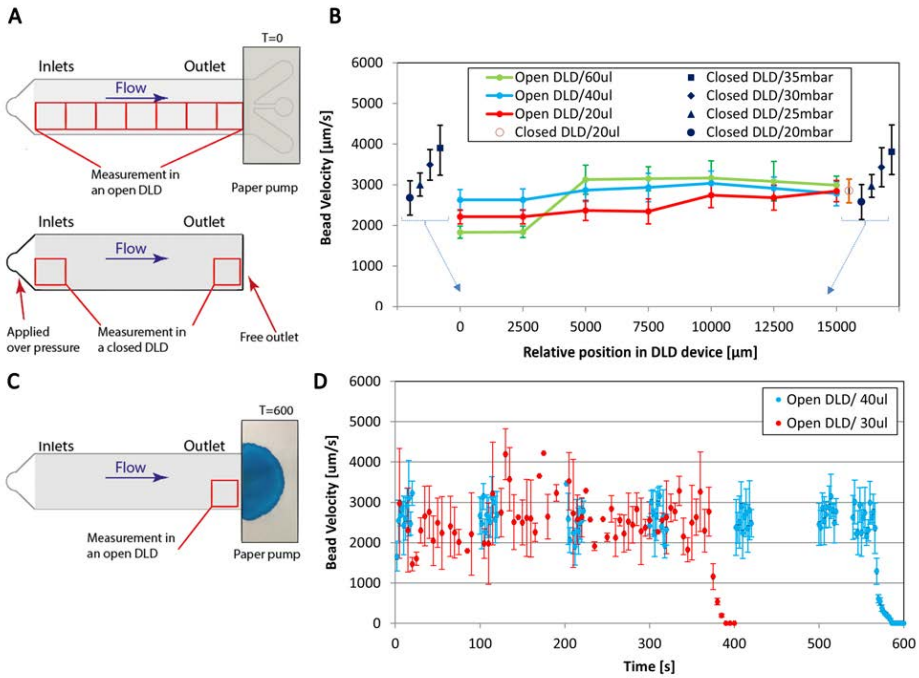

Figure S4. *Particle velocity measurements for open and closed DLD devices. The flow in the open devices is driven by a paper capillary pump without any wax-defined channels. The paper is shown at t=0 s in (A) and t=600 s in (C). The flow in the closed devices is driven by over pressure as well as by a paper capillary pump. The different sets of experiments took place using the same design of DLD (Device 1 (Figure S1)). The following microspheres were used at a dilution of 50x in deionized water: green fluorescent polystyrene beads with diameter 1.57 µm (CV 2%) and functionalized with carboxylate groups from Polysciences Inc. (Warrington, PA). (A) Schematic of measurement setup for velocity measurements at different locations for open and closed devices. (B) Velocity of the beads as a function of position for open and closed devices. For the data where a paper capillary pump was used the volume in the reservoir is indicated. For the pressure driven flow the applied pressure difference is given. (C) Schematic of measurement setup for velocity measurements as a function of time. (D) Velocity of beads as a function of time when 30 µL (red) and 40 µL (blue) of sample is added to the reservoir. The error bars represent the standard deviations of the measurements.*

For the images with the macro objective, the device is wetted with an aqueous food dye and imaged, with the liquid facing upwards, using a macro objective (Canon MP-E 65 mm f/2.8 1-5x) with a Canon 5D Mark II camera house. Basic contrast and brightness adjustments were made to ensure that the image reflects what is seen by the naked eye.

We could observe a tendency that the flow velocity (see below) is slightly lower for the first ~5 mm along the device. This indicates that the flow cross section is larger here, which is consistent with the flow extending above the posts since the volume flow rate is a conserved quantity. We observed that this effect vanishes as the fluid level drops, away from the reservoir and also decreases as the sample volume in the reservoir decreases with time.

Flow measurements

We measured the flow rates at different positions along open and closed devices using an applied overpressure or using a paper capillary pump (Figure S4). Velocities of fluorescent microspheres were observed between two neighboring posts in the same row.

The volumetric flow rates were measured directly by running the device with reservoirs filled with well-defined volumes and recording the elapsed time until the reservoirs were empty (Figure S4D). The volumes were corrected by subtracting the evaporated volume from the device based on figure S5 (8.5 nL/s). The time was measured until the velocity was half of the mean velocity. The remaining liquid in the device was crudely estimated to half the volume of the device, i.e. 0.5*1.1 µL. This volume was subtracted from the total volume considered. From these two measurements we obtain approximate values of 70 nL/s and 61 nL/s for the two different volumes tested. These results are consistent with the results of combining the velocity measurements (Figure S4B) with the total flow cross section based on the designed dimensions (Device 1 in Figure S1C) of the device giving flow rates of 71±19 nL/s. The correspondence of the two types of measurements indicate that the flow is indeed taking place such that it fills up the space between the posts without overflowing.

Equivalent pressures applied to the device

The equivalent pressure exerted by the paper capillary pump is found to be 21 mBar by comparing the applied over-pressure necessary across a closed device to achieve the same flow velocities as for a closed device with a paper capillary pump (Figure S4B). The pressure exerted by the paper capillary pump exceeds the pressure due to the water pillar in the reservoir. The pressure generated in the reservoir depends on the height difference between the inlet and outlet ($\rho\, g\, \Delta h$ ~ 1 mBar/cm with ρ = 1000 kg/m^3 density of water, g = 9.8 m/s^2 gravitational acceleration, Δh height of water pillar). The tested volumes, 30 µL, 40 µL and 60 µL, correspond to heights of 4.2 mm, 5.6 mm and 8.4 mm of sample respectively in the reservoir (inner diameter 3mm) giving hydrostatic pressures of 0.4 mBar, 0.6 mBar and 0.8 mBar which is much less than the involved estimated negative pressures exerted by the capillary paper pump pulling the sample. The capillary pumping effect of the paper therefore dominates the flow and the fluid is predominantly pulled through the device.

Flow resistance

Flow resistance for the closed devices is estimated based on the relationship

$$Q_{pump}^{closed} = \frac{\Delta P_{pump}}{R_{load}^{closed}}$$

where R is the fluidic resistance, Q is the volumetric flow rate and ΔP is the applied pressure difference across the device. From figure S4B we obtain R^{closed} = 30 10^{12} $kgs^{-1}m^{-4}$.

The flow resistance of the open device is expected to be slightly lower than that for the closed device. It is calculated below based on figure S5.

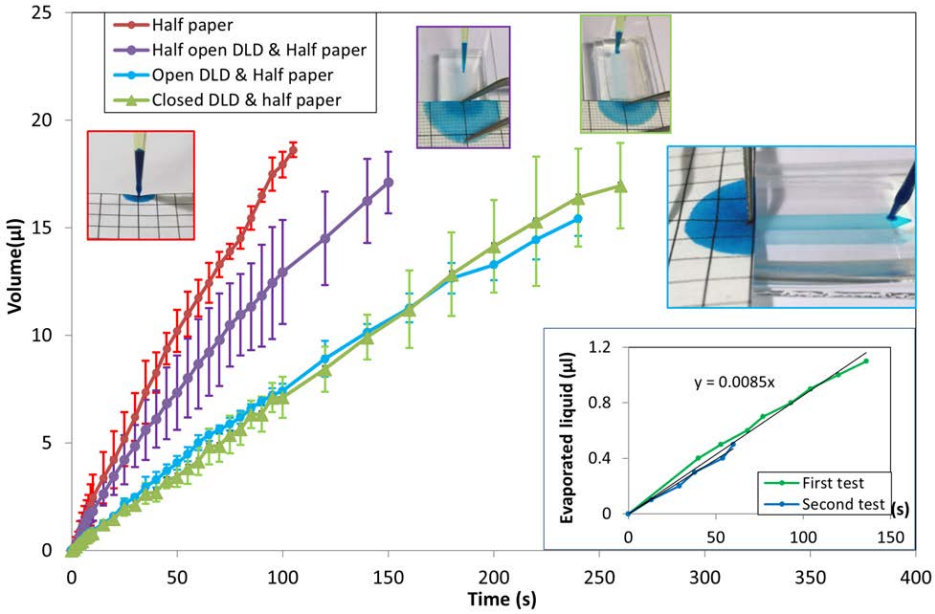

Figure S5. *Liquid flows versus time corrected for evaporation. The liquid is 0.5% food coloring diluted in deionized water. The graph shows four cases. From the left to the right we have: liquid added at the edge of a paper (half paper), open DLD device of length 10 mm (half device) connected to paper, open DLD of length 20 mm (whole device) connected to paper, closed DLD of length 20 mm (whole device) connected to paper. To be able to easily judge the extent of the drops on the paper, a grid pattern is printed on the paper using a standard laser writer. The inset shows the accumulated evaporated liquid from a filled device (device 1). From this graph we can conclude that the evaporation rate from the device is 8.5 nL per second.*

Characterization of the paper capillary pump

The paper capillary pump can be treated as a battery with an internal resistance and an internal negative pressure or, in analogy to electronics, a hydromotive force. To estimate the internal resistance and the hydromotive force the following system of equations (number 1 to 4) are considered. Note that we will obtain an estimate of the flow resistance of the open device from these calculations.

$$\begin{cases} Q_{paper} = \dfrac{\Delta P_{internal}}{R_{internal}} \\ Q_{paper}^{openHALF} = \dfrac{\Delta P_{internal}}{\frac{1}{2}R_{load}^{open} + R_{internal}} \\ Q_{paper}^{open} = \dfrac{\Delta P_{internal}}{R_{load}^{open} + R_{internal}} \\ Q_{paper}^{closed} = \dfrac{\Delta P_{internal}}{R_{load}^{closed} + R_{internal}} \end{cases}$$

We first calculate the internal resistance of the paper by combining equations 1 and 4 above to eliminate the internal pressure (hydromotive force).

$$R_{internal} = \frac{\Delta P_{pump}}{Q_{pump}^{closed}} \frac{Q_{paper}^{closed}}{Q_{paper} - Q_{paper}^{closed}}$$

Numerical data is extracted from Figures S4 (for the pump driven flow) and S5 (for the paper capillary pump driven flow) based on the initial flow rates for each case and combined with the flow resistance of the closed device as calculated above.

$$\Delta P_{pump} = 21 mBar$$
$$Q_{pump}^{closed} = 71 nL s^{-1}$$
$$Q_{paper} = 198 nL s^{-1}$$
$$Q_{paper}^{closed} = 71 nL s^{-1}$$
$$\Rightarrow R_{internal} = 16.5 \cdot 10^{12} kg s^{-1} m^{-4}$$

The hydromotive force is now calculated by using the number of the flow rate of the paper without any device (“Half paper”) in fig S5 combined with equation 1 above.

$$Q_{paper} = 198 nL s^{-1}$$
$$\Rightarrow \Delta P_{internal} = 32 mBar$$

Plugging the results above into equation 3 above, the flow resistance of the open device.

$$Q_{paper}^{open} = 80 nL s^{-1}$$
$$\Rightarrow R_{load}^{open} = 23.1 \cdot 10^{12} kg s^{-1} m^{-4}$$

Finally, as a simple control the flow rate of the device cut in half is estimated based on equation 2 above.

$$Q_{paper}^{openHALF*} = 113 nLs^{-1}$$

The value is lower but still consistent with the value obtained by measuring the initial slope of the corresponding curve in figure S5.

$$Q_{paper}^{openHALF} = 157 nLs^{-1}$$

Evaporation

To obtain rough estimates of the evaporation rates we measured the evaporation rates for different cases by using a precision balance (Ohaus Corp. Pine Brook, NJ USA, model Pioneer PA114C, minimal readout 1 µg).

An evaporation of 8 nL/s from the device can be compared to the typical flow rate through the device of 65 nL/s. Roughly 12% of the sample is thus evaporated from the device.

Due to nonuniform wetting and possible variations in the lab environment during the course of the experiments, the evaporation rates should be considered rough estimates to give a perspective of the relationship between the evaporation rate and the volumetric throughput in the devices.

The lab environment had a 60±5% RH and room temperature of 21°±1° C.

Biological samples

The size distributions of the biological samples used were determined by measurement in optical micrographs using ImageJ (Figure S6). The results are summarized in the following table.

Sample type	*Dimensions ± std dev*	*Shape*
MCF7 (cancer cell line)	17.3±2.1 µm	spherical
White blood cell	12.2±0.9 µm	spherical
Red blood cell	2.2±0.5 µm 7.8±0.6 µm	biconcave
Trypanosome cyclops	2.5±0.5 µm 12.8±3.3 µm	ribbon-like

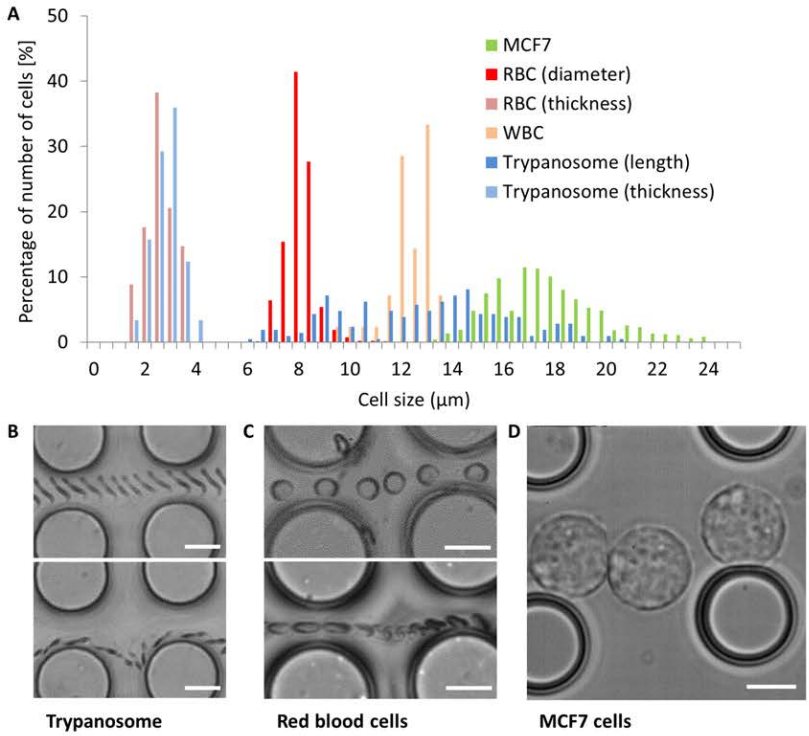

***Figure S6**. Size distribution of biological samples based on measurements in optical micrographs. (A) Histograms of size distributions. For the spherical cells (MCF7 and WBC) one number gives the relevant size (diameter). Red blood cells and the parasites are described by two numbers (thickness and overall diameter or length). (B) & (C) Optical micrographs of the non-spherical cells exhibiting different orientations depending on device depth (9 µm and 24 µm) (top images shallow device and bottom images deep device) (D) Optical micrograph of spherical MCF7 cells. All scale bars 10 µm.*

Paper IV

RBC Rotation in DLD

(The manuscript is not shown due to copyright reason)

Active post DLD

Paper v

(The manuscript is not shown due to copyright reason)

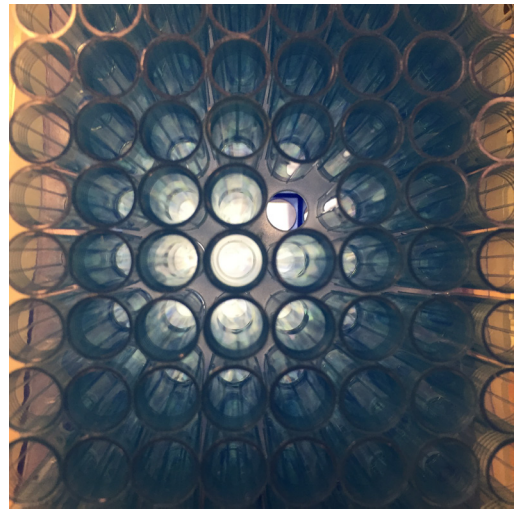

Printed by Media-Tryck, Lund 2018 NORDIC SWAN ECOLABEL 3041 0903

LUND UNIVERSITY

Lund University
Faculty of Engineering
Department of Physics

ISBN 978-91-7753-888-2